

Copyright

by

Jakub Paweł Jodłowski

2012

**The Thesis Committee for Jakub Paweł Jodłowski**  
**Certifies that this is the approved version of the following thesis:**

**Design and Fabrication of a Granular Media Testing Instrument and  
Experimental Determination of Granular Media Flow Behavior under  
Static and Oscillating Normal Loads.**

**APPROVED BY  
SUPERVISING COMMITTEE:**

**Supervisor:**

---

Eric M. Taleff

---

Carolyn C. Seepersad

---

**Design and Fabrication of a Granular Media Testing Instrument and  
Experimental Determination of Granular Media Flow Behavior under  
Static and Oscillating Normal Loads.**

**by**

**Jakub Paweł Jodłowski, B.S.M.E.**

**Thesis**

Presented to the Faculty of the Graduate School of  
The University of Texas at Austin  
in Partial Fulfillment  
of the Requirements  
for the Degree of

**Master of Science in Engineering**

**The University of Texas at Austin**  
**August 2012**

## **Dedication**

To my parents,

Joanna Jodłowska

and

Mieczysław Jodłowski

for their great support throughout my entire academic career

## **Acknowledgements**

I would like to thank my advisor Dr. Eric Taleff for sharing his advice and ideas that allowed me to accomplish this research study. I would like to express my gratitude to Dr. Taleff for mentoring me throughout both undergraduate and graduate career, and teaching me skills required to conduct a research investigation.

I would also like to thank the fellow members of Taleff Research Group, who always provided me with advice and assistance, which allowed me to solve multiple obstacles that occurred during the entire course of this project.

Finally, I want to express my appreciation to the machine shop and electric shop staff at the University of Texas at Austin, who provided me with extremely helpful technical support.

## **Abstract**

# **Design and Fabrication of a Granular Media Testing Instrument and Experimental Determination of Granular Media Flow Behavior under Static and Oscillating Normal Loads.**

Jakub Jodlowski, M.S.E.

The University of Texas at Austin, 2012

Supervisor: Eric M. Taleff

An interest in vehicle efficiency improvement drives a need for research in the field of light metal alloys. Current industrially-available technologies do not include warm-forming of metal alloy sheet materials. The obstacles to the technology may be potentially overcome with granular media, which could be used as an alternative force transfer medium. However, some granular material properties like force chain formation require further investigation before forming technology using granular media may be developed.

Throughout the course of this study, a direct shear cell instrument was designed and fabricated. This instrument was used to measure the basic mechanical properties of granular media. A 3D CAD model of the direct shear cell instrument and operating procedures are presented in this study. Different granular materials, such as steel bearing balls and sand, were tested under conditions simulating granular media flow behavior expected for the working medium in warm-forming of metal alloys sheet materials. The experiments were conducted under both static and oscillating normal loads. The static load experiments were conducted for various normal loads and shear rates, and

oscillating normal load experiments were conducted under various oscillation frequencies, average normal loads and load amplitudes.

During dense-packed spherical granular media flow experiments, shear stress oscillations were observed. These are attributed to the force-chain jamming behavior occurring within the granular media structure. It was also observed that granular media flow properties can be controlled by an oscillating normal load applied to the granular media. From the experimental and simulation studies it may be concluded that normal load oscillations should enhance granular media flow, which could be a great advantage for using granular media as working fluid for sheet metal forming.

## Table of Contents

List of Tables .....	xi
List of Figures .....	xiii
I. PROJECT BACKGROUND AND RESEARCH MOTIVATION .....	1
II. GRANULAR MEDIA LITERATURE REVIEW .....	5
2.1. Introduction .....	5
2.2. Granular Media Models .....	5
2.2.1. Discrete Models .....	6
2.2.2. Continuum Models .....	6
2.3. Granular Flow Regimes .....	7
2.3.1. Dense Granular Flow Overview .....	7
2.3.2. Rapid Flow .....	8
2.3.3. Transitional Flow .....	8
2.4. Granular Flow Experiments Overview .....	11
2.4.1. Shear Tests .....	11
2.4.1.1. Direct Shear Box .....	11
2.4.1.2. Triaxial Test .....	12
2.4.1.3. Rotating Shear Cells .....	13
2.4.1.4. Alternative Shear Test.....	17
2.4.2. Vibration Tests and Jamming in Granular Media Flow.....	17
2.4.3 Vibration Induced Granular Media Fluidization.....	21
2.5. Proposed Experimental Set-up.....	25
III. EXPERIMENTAL INSTRUMENTATION DESIGN .....	26
3.1. Problem Statement .....	26
3.2. Design Requirements .....	26
3.3. Deliverables .....	26
3.4. Design Variants.....	27
3.5. Relevant Calculations .....	27

3.5.1. Normal Stress .....	27
3.5.2. Shear Rate .....	29
3.5.3. DC Motor Selection .....	30
3.5.4. Load Lever Analysis .....	30
3.5.5. Shear Pin Geometry .....	34
3.6. Final Model in CAD .....	35
3.6.1. Frame .....	38
3.6.2. Shear Cell Cavity System .....	38
3.6.3. Drive Mechanism .....	39
3.6.4. Load Application Structure .....	39
3.6.5. Pneumatic Vibration Actuator .....	40
3.7. Final Instrument Design.....	40
<b>IV. EXPERIMENTAL PROCEDURE .....</b>	<b>42</b>
4.1. Instrument Operation Instructions .....	42
4.1.1. Initial Instrument Calibration.....	42
4.1.2. Shear Pin Placement .....	43
4.1.3. Shear Cell Cavity and LVDT Adjustment .....	44
4.1.4. Placing Granular Media in the Cavities .....	45
4.1.4.1 Sand Sieving .....	46
4.1.5. Load Plate Adjustment.....	47
4.1.6. Lever Load Application .....	47
4.1.7. Static Load Test .....	48
4.1.7.1. Loose Packed Experiment.....	50
4.1.7.2. Dense Packed Experiment .....	50
4.1.8. Granular Media Oscillating Load Shear Test Procedure .....	52
4.2. Test Conditions .....	53
4.2.1 Static Load Tests.....	53
4.2.2 Oscillating Load Tests .....	55
4.3. Experimental Data Analysis Procedure .....	56
4.3.1. Force Measurement.....	56

4.3.2. Force Oscillation Analysis .....	57
4.3.3. Shear rate and uncertainty analysis .....	58
4.3.4 Oscillating load experiments analysis.....	59
<b>V. EXPERIMENTAL RESULTS AND DISCUSSION .....</b>	<b>61</b>
5.1. Static Normal Load Experiments.....	61
5.1.1. Shear Stress versus Displacement.....	61
5.1.2. Shear Stress versus Shear Rate .....	63
5.1.3. Internal Friction Angle.....	64
5.1.4. Decay Exponents for Static Normal Load Experiments. ....	68
5.1.5. Shear Stress Oscillation FFT Analysis .....	72
5.2. Oscillating Normal Load Experiments. ....	74
5.2.1. Normal Load Oscillation.....	74
5.2.2. Shear Stress under Oscillating Normal Load.....	75
5.2.3. Oscillating Load Decay Exponents .....	82
5.2.4.Shear Stress versus Displacement.....	84
<b>VI. CONCLUSIONS AND FUTURE WORK RECOMMENDATIONS .....</b>	<b>88</b>
Appendix A: Technical Drawings .....	93
Appendix B: Load Cell Measuring Shear Force .....	99
Appendix C: LVDT .....	105
Appendix D: Load Cell Measuring Normal Load .....	108
Appendix E: Solenoid Valve .....	112
Appendix F: Solid State Relay.....	116
Bibliography .....	119
Vita	122

## List of Tables

Table 4.1.	Load cell LCHD-2K wire connector designation.....	43
Table 4.2.	Static load tests conducted with 2mm chrome steel bearing balls. X represents test on loose packed material, P represents granular material that underwent the dense packing procedure prior to the experiment.....	54
Table 4.3.	Static load tests conducted with 3mm chrome steel bearing balls. X represents test on loose packed material, P represents granular material that underwent the dense packing procedure prior to the experiment.....	54
Table 4.4.	Static load tests conducted with 3mm Delrin® acetal bearing balls. X represents test on loose packed material, P represents granular material that underwent the dense packing procedure prior to the experiment.....	54
Table 4.5.	Static load tests conducted with sand, with grain sizes of 1-2mm....	55
Table 4.6	Oscillating normal load test conditions for 2mm chrome steel bearing balls. X represents test on loose packed material, P represents granular material that underwent the dense packing procedure prior to the experiment.....	55
Table 4.7	Oscillating normal load test conditions for sand with a grain size of 1- 2mm. ....	56
Table 5.1.	Average internal friction angle $\varphi$ , measured in degrees. The “N/C” tests were not conducted. Error represents a mean error that accounts for 95% confidence intervals on angle measurements obtained for each tested shear rate. ....	66

Table 5.2. Peak internal friction angle $\varphi$ , measured in degrees. The “N/C” tests were not conducted. Error represents a mean error that accounts for 95% confidence intervals on angle measurement obtained for each tested shear rate.....	66
Table 5.3. Measurement repeatability study on decay exponents obtained from the fit of shear stress versus time for steel balls with 2mm diameter under normal load of approximately 0.55MPa. Error represents a 95% confidence interval for each of the $\eta$ parameters.....	72

## List of Figures

- Figure 1.1. A forming limit diagram, representing the improvement of ductility in aluminum for hot forming conditions, compared to ductility of aluminum and steel during the stamping process (Taken from Taub [2006, p.341]).....1
- Figure 1.2. Flow stress, normalized by the temperature-dependent elastic modulus, is shown for alloy AA5182 aluminum sheet as a function of the Zener-Hollomon parameter,  $Z = \dot{\varepsilon} \exp(Q/RT)$ , where  $\dot{\varepsilon}$  is the plastic true-strain rate,  $Q=136,000 \text{ J/mol}$ , R is the universal gas constant and T is absolute temperature. Along the top axis, temperature in Celsius is shown for the desirable forming strain rate of  $0.1 \text{ s}^{-1}$  (Taken from Chang [2010, p.3825]).....2
- Figure 1.3. A compression test, where load is applied to the piston at the top causing the granular media within the cylinder to press against the carbon paper at the base. The color intensity of the marks in the paper corresponds directly to the contact force. (Taken from Mueth [1998 , p.3165])....3
- Figure 2.1. Spring dashpot model approach for estimating interparticle contact forces (Taken from Rao [2008, p.25]). .....6
- Figure 2.2 Shear stress versus strain rate for granular flow in the rapid-flowing regime. (Taken from Hanes [1984, p.368]). .....8
- Figure 2.3. Shear stress and normal stress are shown as functions of shear rate, spanning dense flow, rapid flow and transitional flow regimes for sand (Taken from Lu [2007, p.355]). .....10

Figure 2.4. Shear stress as a function of shear rate for polymer powder and silica powder (Taken from Klausner [2000, p.99]).	10
Figure 2.5. (a) Direct shear cell schematic. Load is applied at the lid, top ring experiences shearing force, while the base remains stationary (Figure taken from Rao [2008, p.71]), (b) Change in shear stress and sample height with respect to the sheared distance (Figure taken from Rao [2008, p. 72])	11
Figure 2.6. (a) Triaxial experimental set-up schematic (Figure taken from Rao [2008, p.221]), (b) Stresses applied to the test sample during the experiment, where $\sigma_a$ and $\sigma_r$ indicate axial and radial normal stress respectively (Figure taken from Rao [2008, p.221]), (c) Principal stress ratio $(\sigma_1 - \sigma_3)/\sigma_3$ versus axial strain during compression test on loose (dashed line) and dense (solid line) sand (Figure taken from Rao [2008, p.224])	12
Figure 2.7. Annular shear cell experimental set-up (Taken from Hsiau [1999, p.1971])	14
Figure 2.8. Coutte-shear cell experimental set-up (Taken from Tardos [2003, p.34]).	
	14
Figure 2.9. Force chain formation in sheared granular media (Taken from Howell [1998, p.5241])	15
Figure 2.10. Grain velocities versus the distance from the shear plate, where distance is normalized by the grain diameter and grain velocity is normalized by the cell rotational velocity (Taken form Howell [1998, p.5242])	15

Figure 2.11. (a) Annular shear cell, with a heating system around the sheared material  
(Taken from Wang [1992, p.530]), (b) Close-up of the heating system in  
a (Taken from Wang [1992, p.532]), (c) The apparent thermal  
conductivity,  $k$ , and apparent shear viscosity as functions of shear rate  
(Taken from Wang [1992, p.538]).....16

Figure 2.12 (a) Alternative shear cell experiment (Taken from Bocquet [2008]), (b)  
Velocity versus distance inside the shear band (Taken from Bocquet  
[2008]).....17

Figure 2.13. (a) Experimental set-up measuring the granular media mass delivery  
from a hopper, where the bottom lid is subject to controlled vibrations  
produced by a piezo-electric actuator (Taken from Janda [2009,  
p.24002-p2]), (b) Mass delivered from the hopper as a function of time  
for vibrations with varying amplitude (Taken from Janda [2009,  
p.24002-p4]), (c) Time when the granular media in the hopper is  
jammed for vibrations with varying amplitude (Taken from Janda [2009,  
p.24002-p5]). .....18

Figure 2.14a Experiment measuring the force acting on a rod injected into a moving  
granular layer (Taken from Albert [2000, p.5122]).....19

Figure 2.14b Force acting on the rod as a function of distance travelled by the grains  
for different depths of injection of a rod (Taken from Albert [2000,  
p.5123]).....19

Figure 2.15 (a) Granular media vibration experiment schematic. Experiment was conducted using glass beads used as granular material (Taken from D'Anna [2008, p.011306-1]), (b) Granular media bed vibration intensity response as a function of torque T applied to the rod for different forced granular bed vibration intensities $\Gamma$ . G represents a complex frequency response, obtained from equation $G = T/\theta$ , where $\theta$ represents the optically measured angular displacement (Taken from D'Anna [2008, p.011306-2]). .....	20
Figure 2.16 (a) Experimental set-up with a rotating vane and vibrated granular bed (Taken from Ford [2009, p.34]), (b) Vane torque versus the rotation speed for different granular media bed vibration intensities (Taken from Ford [2009, p.36]).....	21
Figure 2.17 (a) Experimental set-up and nondimensionalized torque versus rotational speed for different granular media bed vibration intensities. (Taken from Dijksman [2011]), (b) Hysteresis loops for different values of vibration intensity $\Gamma$ (Eq. 2.3) in torque-controlled experiments. Horizontal axes represent the nondimensionalized torque (Taken from Dijksman [2011]), (c) Torque-speed behavior for different materials. (Taken from Dijksman [2011]).....	23
Figure 2.18 (a) Experimental set-up for horizontally shaken granular bed. (Taken from Metcalfe [2002]), (b) Schematic of granular media flow in the fluidized layer. (Taken from Metcalfe [2002]), (c) The height of the liquefied layer with respect to the vibration intensity (Taken from Metcalfe [2002]). .....	24
Figure 3.1. Direct shear cell schematic [Figure taken from Puppala].....	27

Figure 3.2. Simply Supported Beam .....	31
Figure 3.3. Lever arm stress analysis [units in psi].....	32
Figure 3.4. Model used in beam vibration analysis. In the implemented design a=2.5 in., d= 16 in., L=18.75 in. ....	33
Figure 3.5. Simply supported beam representing the shear pin .....	34
Figure 3.6. Shear pin shear stress FEA results [units in psi].....	35
Figure 3.7. Isometric view, representing the CAD model of the direct shear cell.	36
Figure 3.8. Direct shear cell major subsystems: A) Load application system, B) DC motor drive system, C) Frame, D) Shear cell cavities, E) Pneumatic vibration actuator. ....	37
Figure 3.9. Direct shear cell fabricated according to the computer-aided design. A) Load application system, B) DC motor drive system, C) Frame, D) Shear cell cavities, E) Pneumatic vibration actuator. ....	41
Figure 3.10. Entire experimental set-up utilized in experiments. A) Signal Conditioners, B) Compressed air supply lines.....	41
Figure 4.1. Vishay2100 Signal Conditioning Module. ....	42
Figure 4.2. Calibration curve for the LCHD-2K load cell attached to the lever arm 43	
Figure 4.3. a) Shear pin, b) Shear pin adjustment. ....	44
Figure 4.4. a) Motor front panel speed knob adjustment and switches, b) Motor controller adjustments.....	44
Figure 4.5. a) Top and bottom shear cell cavities are aligned, b) SC1000 transducer display and signal conditioning unit with LVDT display for aligned shear cells, c) LVDT position adjusted and fixed.....	45
Figure 4.6. Steel bearing balls placed inside the cavities.....	46

Figure 4.7 (a) Sand Sieves, (b) Sieved sand placed in the cavities.....	46
Figure 4.8. Load cell and load plate.....	47
Figure 4.9. Load applied to the lever.....	48
Figure 4.10. NI USB 6210 Data Acquisition module. ....	49
Figure 4.11. Data acquisition front panel: A) RS232 port communication settings, B) Input and output commands from SC1000 Signal Conditioner, C) Shear force and displacement output file path, D) Shear force vs. displacement plot, E) Normal load acquisition settings, F) Normal load vs. time plot, G) Shear speed output, H) Shear speed vs. time plot.....	49
Figure 4.12. Electrical set-up of the pneumatic vibration actuator. (A) Square wave input signal connection from NI USB 6210, (B) Output signal connected to the solenoid valve, (C) 24 VDC power supply, (D) fast recovery diode for transient protection.....	51
Figure 4.13. Pneumatic Vibration Actuator: A) Pressure gauge (B) compressed air supply, (C) air cylinder pressure line, (D) solenoid valve exhaust with attached muffler. ....	52
Figure 4.14. Adjusting the air cylinder position.....	53
Figure 4.15. Shear and normal force sample data measurements for loose random packed 2 mm chrome steel bearing balls. Approximately 275 lbs normal force was applied to the granular media through the loading arm. Granular media was sheared at $0.003 \text{ s}^{-1}$ .....	56
Figure 4.16. FFT Analysis: a) Shear force data acquired from the load cell, b) Steady state shear force offset by the mean force, c) Zero padding applied, d) FFT on shear force data from part (c). ....	58

Figure 4.17. Shear speed measurement: a) Speed measured from slope of the fit to 2 displacement points, b) Speed measurement smoothed by measuring slope of 24 points.....	59
Figure 4.18. Monte Carlo Analysis on speed measurement uncertainty. ....	59
Figure 4.19. (a) Experimental shear force and fit. The experiment was conducted on chrome steel beads with 2mm diameter, an average normal load of approximately 275 lbs, and a shear rate of $0.003\text{ s}^{-1}$ . (b) Fit zoomed during the transient period. .....	60
Figure 5.1. Shear stress versus displacement for static load direct shear experiments conducted under normal stress of approximately 0.6 MPa: (a) Chrome steel 2mm diameter balls, loose packed, (b) Chrome steel 2mm diameter balls, dense packed, (c) Chrome steel 3mm diameter balls, loose packed, (d) Chrome steel 3mm diameter balls, dense packed, (e) Delrin® Acetal 3mm diameter balls, loose packed, (f) Delrin® Acetal 3mm diameter balls, dense packed, (g) Sand 1-2mm diameter. ....	62
Figure 5.2. Literature experimental results from direct shear cell tests: (a) Shear stress versus horizontal strain for 1 mm steel bearing balls with void ratio ranging from 0.5841 to 0.6097 (Figure taken from O'Sullivan [2005]), (b) Shear stress versus displacement for dry Zbraslav sand (grain diameter less than 2mm), normal load of 0.1 MPa and shear speed of 0.1mm/min. Figure presents behavior for loose and dense sand packed sand (Figure taken from Feda [1982]).....	63

- Figure 5.3. Shear stress versus shear rate for chrome steel 2mm diameter bearing balls. The experiments were conducted under a normal stress of approximately 0.6MPa. Vertical error bars represent a 95% confidence interval in shear stress measurement. Horizontal error bars represent a shear rate error introduced after speed smoothing was applied, as prescribed from the Monte Carlo analysis.....64
- Figure 5.4. Shear stress versus normal stress for loose packed 2mm chrome steel bearing balls, sheared at  $0.003\text{ s}^{-1}$ . .....65
- Figure 5.5. Steady-state shear stress versus applied normal stress for sand (1-2mm), loose random packed Delrin® acetal 3mm diameter bearing balls, and loose random packed chrome steel bearing balls with 2mm diameter. All materials were sheared at  $0.003\text{ s}^{-1}$ . .....65
- Figure 5.6. Friction angle, literature results: (a) Peak shear stress versus normal stress for 1mm diameter chrome steel bearing balls [Figure taken from O'Sullivan], (b) Shear stress versus normal stress for Daytona Beach sand. Experimental data was measured at  $37.4^\circ$ , and simulated at  $39.1^\circ$  to  $42.9^\circ$ . Corresponding rounded particle had a measured internal friction angle of  $24.4^\circ$  to  $27^\circ$  (Figure taken from Das [2007])......67
- Figure 5.7. Exponential decay fits to shear stress versus displacement plots for the experiments under static loads. Blue curves represent the experimental data for the tests with the following conditions: (a) Steel 2mm loose packed sheared at  $0.003\text{ s}^{-1}$  with normal load of approximately 0.6MPa, (b) Sand 2mm sheared at  $0.003\text{ s}^{-1}$  with normal load of approximately 0.55MPa. Plots on the right present the experimental data during the transient period.....69

Figure 5.8. Decay exponents for static load tests conducted at a shear rate of  $0.003\text{ s}^{-1}$ . The exponents were obtained from fitting the exponential decay equation (Eq. 4.2) to shear stress versus time plots.....70

Figure 5.9. Decay exponents for static load tests conducted on chrome steel balls of 2mm diameter. The exponents were obtained from fitting the exponential decay equation to shear stress versus displacement plots.71

Figure 5.10. Shear stress FFT analysis on dense packed chrome steel balls under an approximate normal load of 0.6MPa: (a) 2mm diameter, shear rate of  $0.003\text{ s}^{-1}$  (b) 2mm diameter, shear rate of  $0.012\text{ s}^{-1}$  (c) 2mm diameter, shear rate of  $0.021\text{ s}^{-1}$  (d) 3mm diameter, shear rate of  $0.003\text{ s}^{-1}$  (e) 3mm diameter, shear rate of  $0.012\text{ s}^{-1}$  (f) 3mm diameter, shear rate of  $0.021\text{ s}^{-1}$ . The dashed vertical line on each plot represents the grain bead inverse diameter.....73

Figure 5.11. (a) Annular shear cell experimental set-up (Figure taken from Miller [1997]), (b) Transducer stress measurement versus time; horizontal mark “d” represents the time corresponding to the top lid travelling a distance of one bead diameter (Figure taken from Miller [1997]).....74

Figure 5.12. Predicted and measured normal load applied to granular media during the oscillating normal load experiment. Initial load applied to the lever equals approximately 0.55MPa. The data were obtained from a test conducted with air under 30 psi pressure applied to the pneumatic cylinder at the frequency of 2 Hz.....75

Figure 5.13. Chrome steel 2mm bearing balls sheared at a steady-state rate of  $0.003\text{s}^{-1}$  under oscillating load at  $f=0.03\text{Hz}$ , (a) Normal load oscillation, dashed lines indicate average normal stress during low and high load application, and a corresponding 95% confidence interval, (b) Shear stress, normal stress, and expected steady-state shear stress, (c) Shear stress oscillation (d) Exponential decay fit applied to the shear stress for  $\frac{1}{2}$  of the load cycle at  $t_0 = 126.2\text{s}$ .....76

Figure 5.14. Chrome steel 2mm bearing balls sheared under oscillating load at  $f = 0.9\text{Hz}$ , (a) Normal load oscillation, (b) Shear stress and normal load during 5 periods of normal load oscillation, (c) Shear stress oscillation, (d) Shear stress and normal load during 5 periods of normal force oscillation, with shear stress acquired at 100 Hz, (e) Shear stress exponential decay model (labeled ‘Transient  $\eta = 1.1 \text{ s}^{-1}$ ’) compared to experimental data, after the high normal load was applied for  $\frac{1}{2}$  load cycle at  $t_0 = 100.5\text{s}$ .....78

Figure 5.15. Steel 2mm diameter dense packed bearing balls, sheared at  $0.003 \text{ s}^{-1}$  under an oscillating load; normal load is oscillating at  $0.9\text{Hz}$  between  $0.12\text{MPa}$  and  $0.55\text{MPa}$  (a) Shear stress versus time, (b) Shear stress FFT analysis on the data presented in part A, the dashed line represents an inverse of the time required for the shear cell to travel 1 ball diameter.

Figure 5.16. Sand sheared under oscillating load at  $f = 0.01\text{Hz}$ , (a) Normal load oscillation, dashed lines indicate average normal stress during low and high load application periods, and a corresponding 95% confidence interval, (b) Normal load, shear stress and expected steady-state shear stress, (c) Shear stress (d) Exponential decay fit applied to the shear stress after the high normal load was applied for  $\frac{1}{2}$  cycle at  $t_0 = 45.5\text{s}$ .

81

Figure 5.17. Sand sheared under oscillating load at  $f = 0.3\text{Hz}$ , (a) Normal load oscillation, (b) Normal load and shear stress during 5 periods of normal force oscillation, (c) Shear stress, (d) Exponential decay fit applied to shear stress when the high normal load is applied for  $\frac{1}{2}$  cycle at  $t_0 = 103.32\text{s}$  .....82

Figure 5.18. Decay exponents obtained from fits to experimentally measured shear stress when the high normal load is applied. The experiments were conducted on 2mm chrome steel bearing balls with initial normal load of 0.55MPa, air cylinder pressure of 30 psi (low load of 0.12MPa) and 25psi (low load of 0.25MPa), and the following load oscillation frequencies: (a)  $f = 0.03\text{ Hz}$ , (b)  $f = 0.06\text{ Hz}$ , (c)  $f = 0.12\text{ Hz}$ , (d)  $f = 0.3\text{ Hz}$ , (e) Average decay exponents for each of the 4 analyzed load oscillation frequencies are plotted versus frequency. .....83

Figure 5.19. Literature results of load reversed experiments (a) Shear stress versus shear displacement for direct shear tests conducted on Zbrasalv sand (Figure taken Feda [1982]), (b) Specimen consisting of steel beads used in triaxial load-unload experiment (Figure taken from O'Sullivan [2005]), (c) Stress-strain results for the triaxial experiment on the specimen presented in Figure 5.19b (Taken from O'Sullivan [2009]).84

Figure 5.20. Shear stress versus displacement for 2mm diameter chrome steel bearing balls under normal load oscillating between 0.12MPa and 0.55MPa at:  
(a)  $f = 0.12\text{Hz}$ , (b)  $f = 0.3\text{Hz}$ , (c)  $f=0.9\text{Hz}$ . .....85

Figure 5.21. A schematic presenting a change in shear cell displacement due to the normal force applied. .....86

Figure 5.22. 2 mm diameter steel balls, sheared at  $0.003 \text{ s}^{-1}$  (a) Shear stress versus time during a static load test with normal load of 0.55 MPa, (b) Shear stress versus time during experiment with normal load oscillating between 0.12 MPa to 0.55 MPa, (c) Shear cell speed measured during the experiment presented in Figure 5.22a, data were smoothed using a Monte Carlo analysis, (d) Shear cell speed measured during the experiment presented in Figure 5.22b (data are not smoothed).....87

Figure 6.1. Granular media shear stress model comparison between steady state static load and oscillating normal load experiments for 2 mm steel bearing balls. The simulations are conducted at shear rate of  $0.003\text{ s}^{-1}$ , or shearing speed of 0.12 mm/s. The average oscillating normal load equals 1kN, which is equal to the static load applied, for each simulation. Oscillating normal load applied during the simulation is presented in (a). The oscillating load is simulated with the following frequency f, and normal load amplitude A: b)  $f=0.2\text{Hz}, A=200\text{N}$ , c)  $f=1\text{Hz}, A=200\text{N}$ , d)  $f=0.2\text{Hz}, A=500\text{N}$ , e)  $f=1\text{Hz}, A=500\text{N}.....90$

## I. PROJECT BACKGROUND AND RESEARCH MOTIVATION

In the pursuit of increased vehicle efficiency through weight reduction, a significant interest in light metal alloys has been developed. Use of aluminum and magnesium alloys allows for considerable vehicle weight reduction, compared to traditional steel structures, which has a direct correlation to fuel efficiency improvement. This correlation may be described quantitatively by the fact that “for every 10% reduction in vehicle mass fuel economy is improved by 6%” [Taub, 2006]. Although characterized by low formability at room temperature, light metal alloys actually present feasible forming properties at warm- and hot- forming temperatures. The significant ductility improvement for high temperature forming of aluminum may be observed from the forming limit diagram in Figure 1.1.

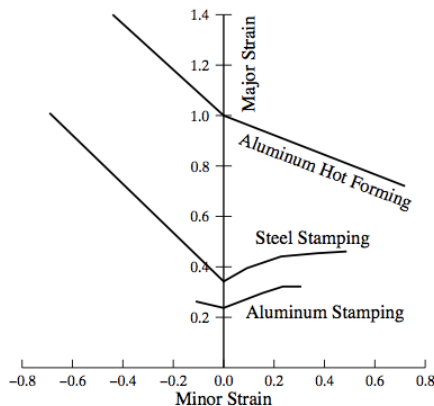


Figure 1.1. A forming limit diagram, representing the improvement of ductility in aluminum for hot forming conditions, compared to ductility of aluminum and steel during the stamping process (Taken from Taub [2006, p.341]).

The two major roadblocks to the emergence of light metal alloys in warm forming applications are the lack of an industrially feasible pressure medium and a lack of suitable lubricants allowing material deformation in the warm- forming temperature range of 200 °C to 400 °C. Gas pressure is commercially used in forming parts at temperatures of

400 °C and higher. However, high material flow stress requires very high gas pressures to meet the industry strain rate requirements (on the order of 0.1 s<sup>-1</sup>) at lower temperatures, higher pressures than practical in general application. Figure 1.2 presents data showing the increase in material flow stress with decreasing temperature (see the top scale) for aluminum AA5182 alloy, which is of great commercial interest to the automotive industry.

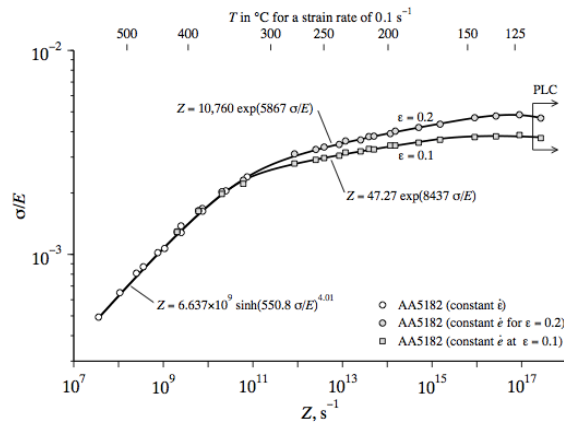


Figure 1.2. Flow stress, normalized by the temperature-dependent elastic modulus, is shown for alloy AA5182 aluminum sheet as a function of the Zener-Hollomon parameter,  $Z = \dot{\varepsilon} \exp(Q/RT)$ , where  $\dot{\varepsilon}$  is the plastic true-strain rate,  $Q=136,000$  J/mol,  $R$  is the universal gas constant and  $T$  is absolute temperature. Along the top axis, temperature in Celsius is shown for the desirable forming strain rate of 0.1 s<sup>-1</sup> (Taken from Chang [2010, p.3825]).

An alternative approach to warm forming is the use of die stamping. This method requires lubricants, which currently restrict the use of die stamping to temperatures lower than approximately 200 °C. At higher temperatures, liquid lubricants, such as oils and greases, remain generally inapplicable due to rapid degradation. Solid lubricants (e.g. graphite or boron nitride), which can be used at higher temperatures, provide an alternative solution. However, industrially accepted solid lubricants do not provide sufficient lubrication to account for high die contact pressures and are very difficult to clean from parts.

Granular media show an interesting potential to overcome both of the above-mentioned barriers. Granular media may transmit considerably higher pressures than gases. Since granular media may behave in a fluid-like manner, a considerably lower friction will occur when pushing material into an open die cavity, possibly eliminating the need for the excellent lubrication required during the die-stamping process. Solid lubricants may still be used to reduce the friction between the deformed material and a die surface, when there is relatively low contact pressure. It is of major interest to determine the feasibility of obtaining a uniform pressure distribution throughout the granular media bed in the process of warm forming of light alloys. A nonuniform pressure distribution could potentially lead to difficulties in sheet metal forming control. A nonuniform force distribution may be visualized from Figure 1.3. In this experiment a granular medium is statically pressed with a normal force against a fixed lower piston. A carbon paper sheet between the granular medium and the piston allows recording of the normal force distribution during the experiment. Since darker spots correspond to higher normal forces, it is shown that the force is transferred to the lower piston in a highly nonuniform pattern.

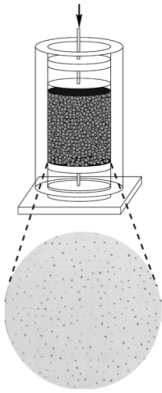


Figure 1.3. A compression test, where load is applied to the piston at the top causing the granular media within the cylinder to press against the carbon paper at the base. The color intensity of the marks in the paper corresponds directly to the contact force. (Taken from Mueth [1998 , p.3165]).

The major goal of this project is to study the effects of pressure on flowing granular media in the presence of varying normal stresses, flow rates and granular media material. The literature review presents the theory and current understanding of granular media flow. This overview is primarily focused on previously utilized experimental instruments in granular media flow study, which form a background in the selection process for the experimental set-up proposed in this project.

## **II. GRANULAR MEDIA LITERATURE REVIEW**

### **2.1. INTRODUCTION**

The purpose of this literature review is to present the state of research in the field of granular media flow. It is of interest to understand the physical laws that govern granular media in different flow regimes. Granular media behave differently from solids, liquids or gases, due to dissipative grain interaction, including inelastic collisions and friction [Aaranson, 2006].

This literature review is focused on collecting information that describes flow of granular media within a slow flowing regime. This particular regime is expected to play the key role in the process of warm forming of materials. Nevertheless, a review of other regimes is also presented, in order to provide a better general understanding of granular media.

In order to better understand the expected behavior of granular media during material forming applications, the literature review is focused on studies of granular media subjected to compression, shear or vibration. Common experiments, which incorporate one or more of these states, are presented in this literature review.

### **2.2. GRANULAR MEDIA MODELS**

In general the proposed physical models for granular media may either be classified as discrete or continuum [Rao, 2008]. Discrete models look at interactions between individual grains, whereas the continuum approach looks at granular media as a continuous medium.

### 2.2.1. Discrete Models

Discrete models focus on simulating interactions between individual particles. In general, there are a variety of different modeling techniques that may apply in the discrete modeling approach. One example of such an approach proposes calculating the normal contact force between two particles using a spring-and-dashpot model and tangential force using spring, dashpot and slider elements as presented in Figure 2.1. Many open source software Discrete Element Modeling (DEM) packages are available, like for example: ESyS-Particle, Yade, or MechSys. All the software packages utilize an analysis based on the approach initially proposed by Cundall and Strack, which is similar to the approach presented in Figure 2.1.

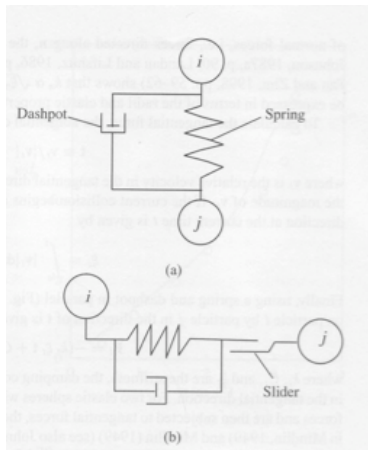


Figure 2.1. Spring dashpot model approach for estimating interparticle contact forces (Taken from Rao [2008, p.25]).

### 2.2.2. Continuum Models

In principle this approach looks at granular media in a continuum manner and uses the laws of continuum mechanics to predict behavior of the medium [Rao, 2008]. However, this approach requires a use of constitutive relations, which still have not been thoroughly established over a wide range of conditions for granular media [Rao, 2008]. The existing theories analyze granular flow depending on the flow rate or flow geometry.

## 2.3. GRANULAR FLOW REGIMES

In a variety of papers studying the flow of granular media it was pointed out that granular media may behave considerably differently depending on the flow rate of the medium. The Savage number for granular media allows distinguishing between rapid and slow flow regimes. Physically, the Savage number represents the ratio of stresses due to interparticle collisions to the normal stress [Lu, 2007]. For a granular medium with a particle density  $\rho$ , a mean grain diameter  $d$ , and subjected to a shear rate  $\dot{\gamma}$  and normal stress  $\sigma$ , the Savage number ( $Sa$ ) may be represented as:

$$Sa = \frac{\rho d^2 \dot{\gamma}^2}{\sigma} \quad [2.1]$$

For Savage numbers much less than one, flow is expected to fall under the dense granular flow regime. High Savage numbers indicate rapid flow; however, there seems to be no single Savage number that is commonly agreed upon to indicate the onset of a rapid flow.

Bagnold proposed a modified nondimensional parameter that distinguishes between the two flow regimes [Hanes, 1984].

$$B = \rho \mu^{-1} \lambda^2 d^2 \dot{\gamma} \quad [2.2]$$

In this parameter the additional variables taken into account are linear concentration  $\lambda$ , and interstitial fluid viscosity  $\mu$ . Bagnold's numbers less than 40 indicate quasi-static flow, and Bagnold's numbers greater than 450 indicate grain inertial flow [Hanes, 1984].

### 2.3.1. Dense Granular Flow Overview

Dense granular flow, which is also referred to as quasi-static flow, is generally described as slow and high solid-fraction flow. The interactions between the grains in this regime are of a Coulomb frictional nature. Momentum exchange in this regime occurs mostly through sliding and rolling [Lu]. Granular flow in this regime shows no dependence between the shear stress and shear rate. A general theoretical understanding for dense granular flow in shear is expressed by the critical state theory [Rao, 2008].

### 2.3.2. Rapid Flow

The main particle interaction in a grain inertial flow occurs by short-duration binary collisions [Lu, 2007]. When tested in a shear cell, rapid granular flow shows a quadratic dependence between the shear stress and shear rate. This behavior is presented in Figure 2.2. This interesting behavior was confirmed for granular flow with different types of granular media and particle diameters. The shear rate and shear stress dependence may vary in cases when different interstitial fluids are used. It was observed that, for the same range of shear rates and the same type of particles, the slope decreases when water is used instead of air as an interstitial fluid [Hanes, 1984]. This indicates that interstitial fluid may cause a change in the flow regime, as predicted from Bagnold's number.

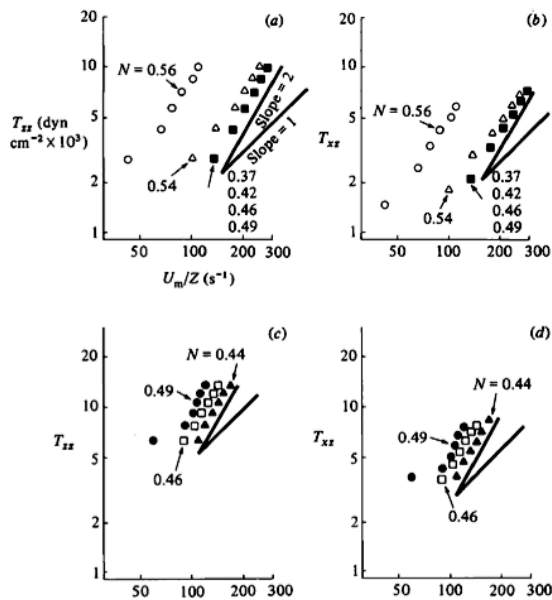


Figure 2.2 Shear stress versus strain rate for granular flow in the rapid-flowing regime.  
(Taken from Hanes [1984, p.368]).

### 2.3.3. Transitional Flow

While most papers analyze different approaches for either rapid or dense granular flow, some scientists span both regimes in their experiments to include

transitional flow. While it is generally established that the dense granular flow regime is rate independent and the rapid flow regime shows a quadratic dependence on rate for shear stress, the transitional flow regime still requires a more in-depth analysis [Lu, 2007]. In a constant volume experiment in a cylindrical shear cell, it was found that both shear and normal stress, applied to the loading plate, experience a stress-weakening effect in the region between slow and rapid flow regimes [Lu, 2007]. In this regime, shear stress drops below the shear stress value recorded for the dense granular flow regime, as pictured in Figure 2.3. The authors have also noted that the granular media under higher normal load exhibit greater shear weakening. In this particular experiment, sand was utilized as a granular medium. The occurrence of the shear weakening effect shows a strong dependence on the type of material used, indicating that size distribution or sphericity could strongly influence granular media flow behavior. An interesting result occurs in the case of powders for a similar experimental test set up. Figure 2.4 shows shear stress versus shear rate for silica and polymer powders. Both powders behave similarly in the dense flow regime. However, while shear stress in silica powder increases at high shear rates, shear stress in the polymer powder stays rather constant [Klausner, 2000]. While silica powder is non-cohesive, polymer powder has cohesive characteristic. Hence, Figure 2.4 indicates the importance of a cohesion factor in determining the behavior of granular media. An effect resembling shear weakening, presented in Figure 2.3, may also be observed for silica powder in Figure 2.4.

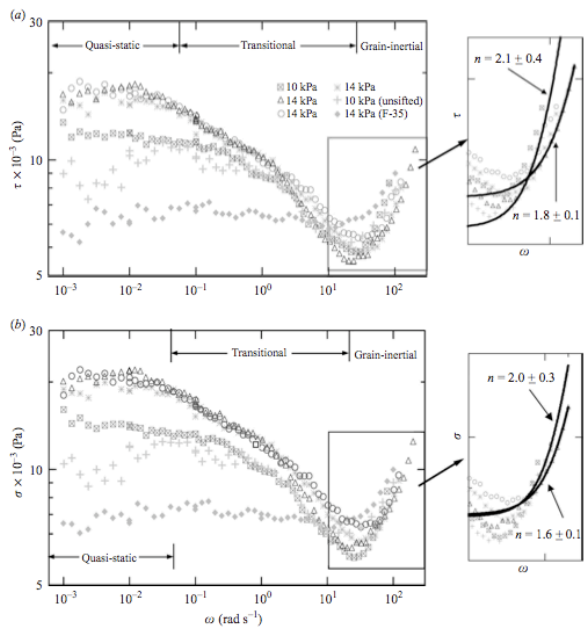


Figure 2.3. Shear stress and normal stress are shown as functions of shear rate, spanning dense flow, rapid flow and transitional flow regimes for sand (Taken from Lu [2007, p.355]).

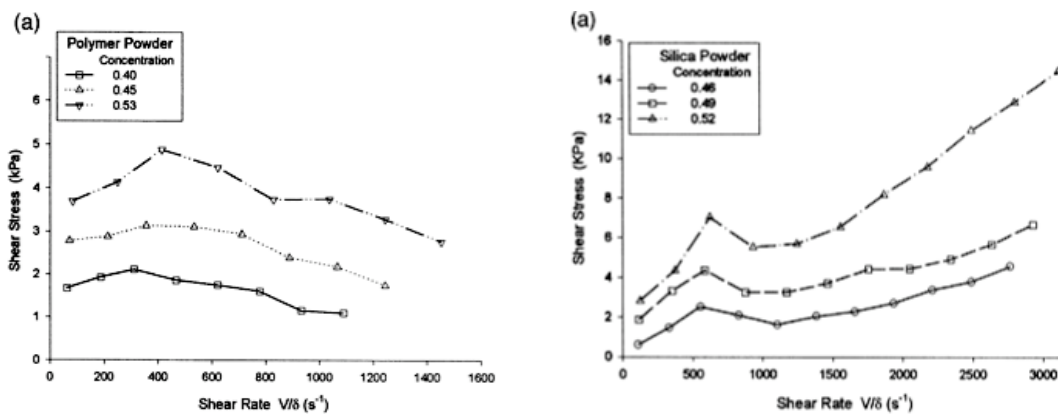


Figure 2.4. Shear stress as a function of shear rate for polymer powder and silica powder (Taken from Klausner [2000, p.99]).

## 2.4. GRANULAR FLOW EXPERIMENTS OVERVIEW

### 2.4.1. Shear Tests

#### 2.4.1.1. Direct Shear Box

The direct shear cell is a test apparatus that allows testing granular media at high normal stresses and low shear rates. An example of a direct shear cell is presented in Figure 2.5a. This particular shear box, also known as Jenike shear cell, consists of two cells. The bottom cell remains stationary, while a shearing force is applied to top cell, which is free to move. Depending on whether the granular media is dense or loose, a shear stress spike may occur at a given normal stress in the graph of shear stress versus displacement, as presented in Figure 2.5b.

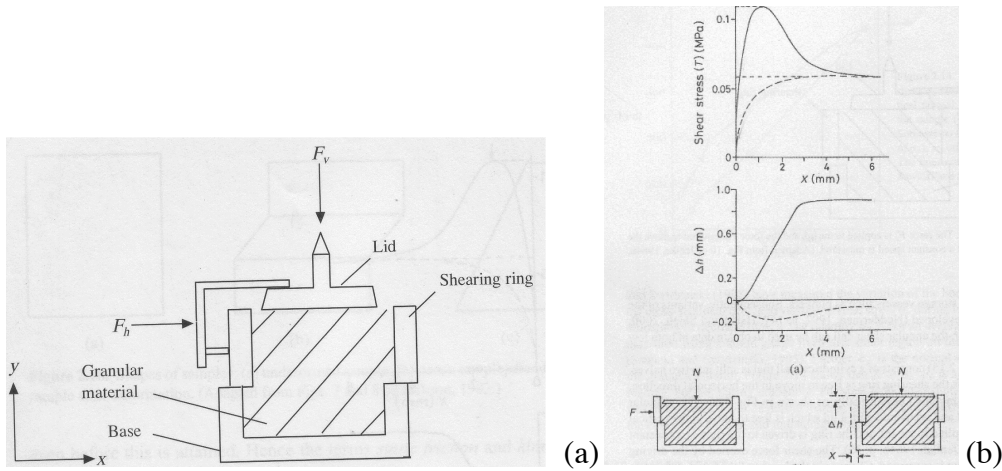


Figure 2.5. (a) Direct shear cell schematic. Load is applied at the lid, top ring experiences shearing force, while the base remains stationary (Figure taken from Rao [2008, p.71]), (b) Change in shear stress and sample height with respect to the sheared distance (Figure taken from Rao [2008, p. 72]).

### 2.4.1.2. Triaxial Test

Triaxial testing apparatus, schematically presented in Figure 2.6a, provides an alternative method of testing granular media in the slow flow regime. During the experiment, the granular media forms a cylindrical specimen, restrained by a rubber membrane. Normal load is applied at the top of the sample cylinder using a loading ram, and radial stress is applied to the granular medium by water inside the cell. Axial and radial loads may be measured by measuring cell and pore pressure respectively. The test exhibits negligible shear stresses in the membrane; hence, the axial and radial stresses may be considered as principal stresses, as presented in Figure 2.6b. Principal stresses analyzed for loose and dense sand samples during the triaxial experiments (Figure 2.6c) reveal a characteristic behavior similar to the experiments conducted in direct shear.

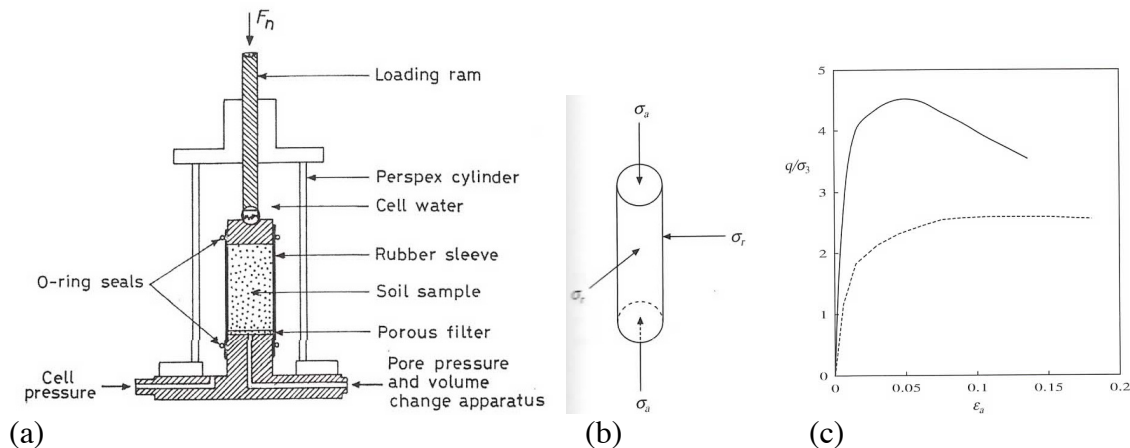


Figure 2.6. (a) Triaxial experimental set-up schematic (Figure taken from Rao [2008, p.221]), (b) Stresses applied to the test sample during the experiment, where  $\sigma_a$  and  $\sigma_r$  indicate axial and radial normal stress respectively (Figure taken from Rao [2008, p.221]), (c) Principal stress ratio  $(\sigma_1 - \sigma_3)/\sigma_3$  versus axial strain during compression test on loose (dashed line) and dense (solid line) sand (Figure taken from Rao [2008, p.224]).

#### ***2.4.1.3. Rotating Shear Cells***

The annular shear cell appears to be the most commonly proposed experimental geometry in the field of granular media flow research. A multitude of different annular shear cell designs exist in the literature. Figure 2.7 shows one type of annular shear cell instrument [Hsiau, 1999]. A speed-controlled motor actuates rotation of the bottom plate, while the top plate, which is stationary, fits inside a groove inside the bottom plate. Bearings on the fixed shaft allow the cover plate to move in the vertical direction to accommodate solid fraction changes in sheared granular media. It is very common to roughen the top and bottom plates in the shearing cell, while keeping the sidewalls as smooth as possible in order to approximate a two-dimensional shear geometry.

In a variety of research papers that study the behavior of granular media within an annular shear cell, some set-up modifications may be noticed. However, the general idea behind the experiment does not change. For example, some experiments propose the use of a counter-weight to balance out the weight of the top plate [Ji, Hanes]. Another experiment proposes the use of an LVDT to measure the displacement of the top plate and a tangential load cell, consisting of a known moment arm attached to the top plate, in order to determine the torque acting on the granular media [Klausner, 2000]. Another experiment proposes use of cylindrical shear cell where, instead of a grooved ring, the entire cylindrical space is subjected to shear [Lu, 2007].

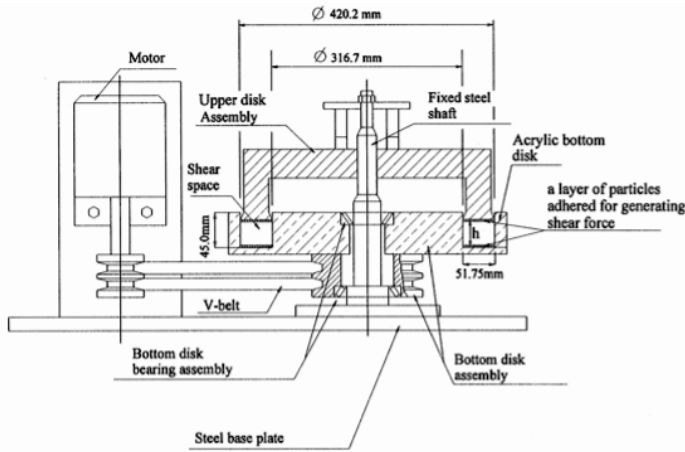


Figure 2.7. Annular shear cell experimental set-up (Taken from Hsiau [1999, p.1971]).

A shear cell may also have a Couette geometry, as presented in Figure 2.8 [Tardos, 2003]. This experiment is in principal very similar to the annular shear cell experiment. It consists of inner and outer cylinders. The inner cylinder imposes shear stress in the granular medium, while the outer cylinder remains stationary. Particles in this experiment may be sheared without having a plate imposing a normal stress on the medium. This experiment also uses of a piston sensor to measure normal stress exerted by the granular medium. Normal load may be applied parallel to the shearing plane, as opposed to perpendicular to shearing plane in the annular shear cell geometry.

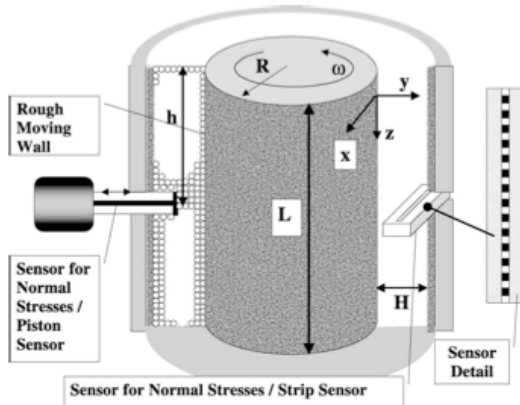


Figure 2.8. Couette-shear cell experimental set-up (Taken from Tardos [2003, p.34]).

Figure 2.9 shows formation of force chains within a shear cell. This effect was observed using photoelastic particles as the granular medium. It was commonly observed and pointed out in multiple papers that the thickness of the shear band in a shear cell is approximately ten grain diameters. The result that confirms this observation is presented in Figure 2.10, which presents grain velocity versus the distance from the shearing plane. It was also pointed out that the shear thickness may vary with the granular material [Bocquet, 2008].

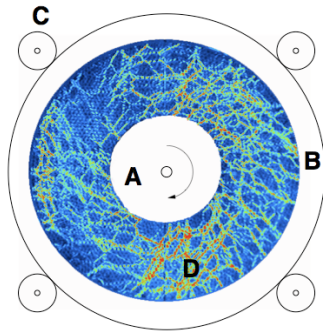


Figure 2.9. Force chain formation in sheared granular media (Taken from Howell [1998, p.5241]).

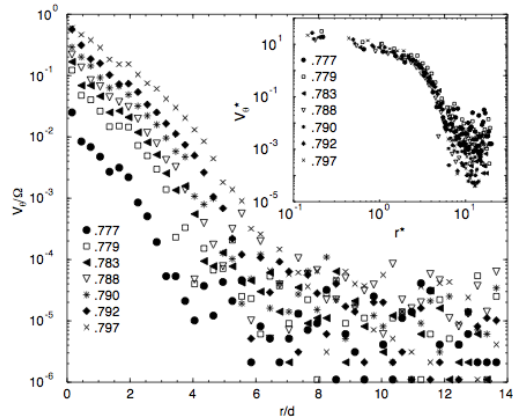


Figure 2.10. Grain velocities versus the distance from the shear plate, where distance is normalized by the grain diameter and grain velocity is normalized by the cell rotational velocity (Taken form Howell [1998, p.5242]).

It was also proposed to include a heating system around the test region to measure thermal conductivity of granular media under different packing during shearing [Wang]. Figures 2.11a and 2.11b present schematics of this shear cell and a detailed overview of the heating system. The results for apparent viscosity and thermal conductivity measured as functions of shear rate are presented in Figure 2.11c. It is worth noting the strong dependence of solid fraction on both apparent conductivity and viscosity.

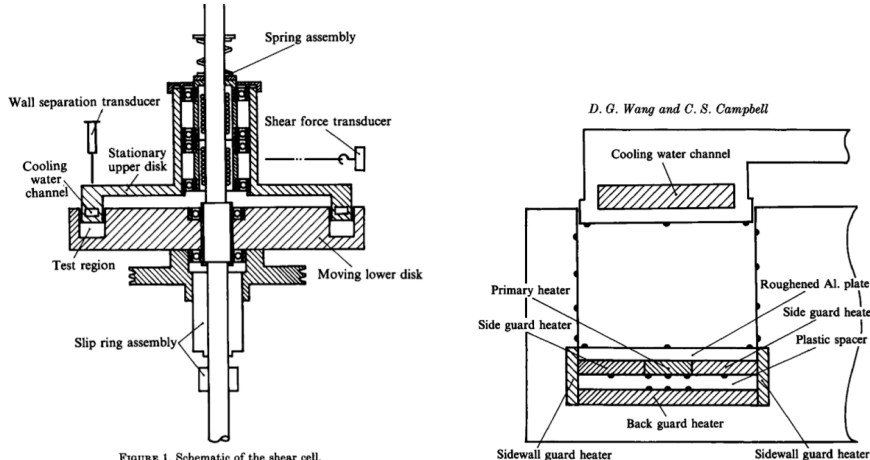


FIGURE 1. Schematic of the shear cell.

(a) (b)

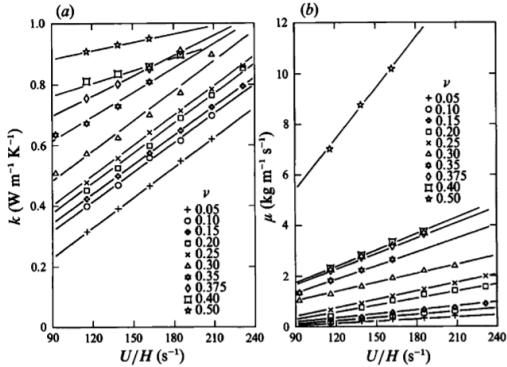


FIGURE 4. (a) The apparent thermal conductivity  $k$  and (b) the apparent shear viscosity  $\mu$  as functions of shear rate for 3.0 mm glass beads.

(c)

Figure 2.11. (a) Annular shear cell, with a heating system around the sheared material (Taken from Wang [1992, p.530]), (b) Close-up of the heating system in a (Taken from Wang [1992, p.532]), (c) The apparent thermal conductivity,  $k$ , and apparent shear viscosity as functions of shear rate (Taken from Wang [1992, p.538]).

#### 2.4.1.4. Alternative Shear Test

Another interesting experimental set-up for testing granular media behavior in shear forces the flow of granular media using an outside substance, like air, to push the granular media around a rotating cylinder, as presented in Figure 2.12a [Bocquet, 2008]. In principal, this experiment is very similar to the rotating shear cell experiment presented in Figure 2.7. It also shows the same velocity gradient in the shear band region (Figure 2.12b) commonly observed for annular shear cell experiments. The authors of this experiment observed no dependence between shear rate and shear stress for dense granular flow, confirming that their results are in agreement with standard annular shear cell results.

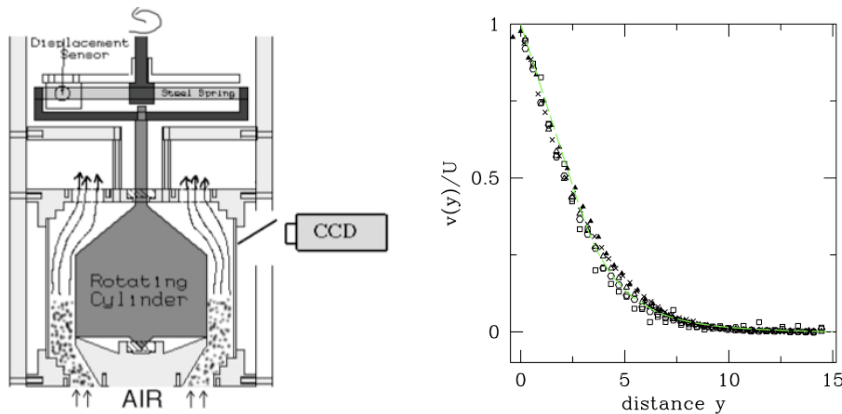


Figure 2.12 (a) Alternative shear cell experiment (Taken from Bocquet [2008]), (b) Velocity versus distance inside the shear band (Taken from Bocquet [2008]).

#### 2.4.2. Vibration Tests and Jamming in Granular Media Flow

In granular media stress is generally transmitted through force chains, which occur due to such effects as variations in the particle sizes, imperfections in packing arrangements and nonlinear interparticle friction forces [Mueth]. In consequence, only a fraction of all the particles, which form the force chains, becomes active in the force transfer process. These chains can potentially cause jamming and impede the motion of granular media. Various experiments show that force chains may be broken when vibration is introduced during the granular media flow. One possible experiment that

studies vibration response of granular media is presented in Figure 2.13a. In this experiment granular media, flowing in a granular hopper through a small opening, is continuously vibrated using a piezo-electric actuator. The authors of this experiment only varied amplitude of vibration. Figure 2.13b shows the mass delivered from the hopper versus time for vibrations with different amplitudes. The horizontal lines correspond to the jamming times. It can be noticed from this figure that greater vibration amplitude reduces jamming time. However, it should also be pointed out that for every test, the same number of grains is delivered, even if the tests are run for different time periods. This suggests that the vibration effect may be scaled with time, meaning that a large vibration amplitude may be simulated by a small amplitude over a longer time period. Figure 2.13c shows that the fraction of time during which the flow is jammed, and it can again be noticed that the flow induced at the largest vibration amplitude experiences considerably less jamming than flows at smaller amplitudes.

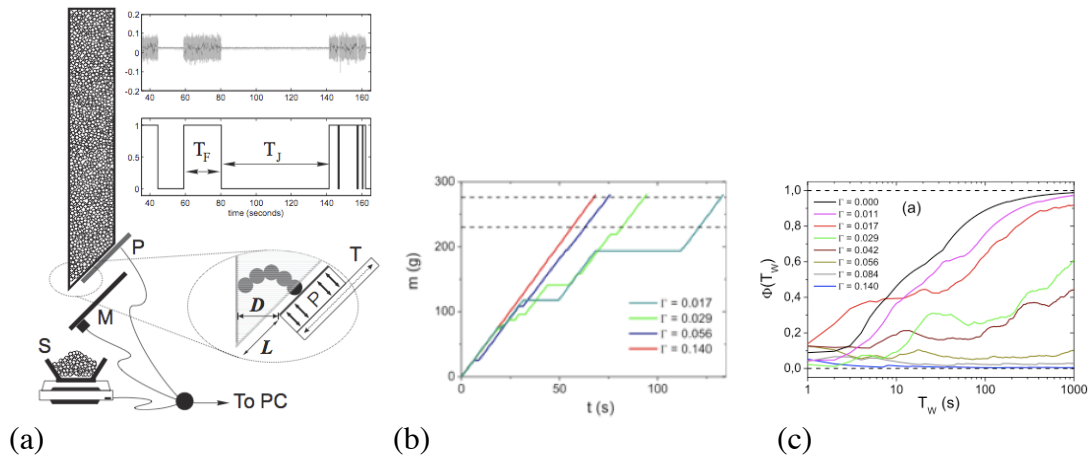


Figure 2.13. (a) Experimental set-up measuring the granular media mass delivery from a hopper, where the bottom lid is subject to controlled vibrations produced by a piezo-electric actuator (Taken from Janda [2009, p.24002-p2]), (b) Mass delivered from the hopper as a function of time for vibrations with varying amplitude (Taken from Janda [2009, p.24002-p4]), (c) Time when the granular media in the hopper is jammed for vibrations with varying amplitude (Taken from Janda [2009, p.24002-p5]).

Another experiment testing the behavior of jammed granular matter uses a rod inserted into a moving granular bed, as presented in Figure 2.14a [Albert]. The force acting on the rod is measured in the direction parallel to the granular flow. This force is subjected to fluctuations when the force chains around the rod constantly form and break. There is an interesting transition from purely periodic to stepped fluctuation, depending on the depth to which the rod is submerged into the granular medium, as shown in Figure 2.14b. This figure implies that normal stress variation within the granular medium affects the jamming characteristic in the material.

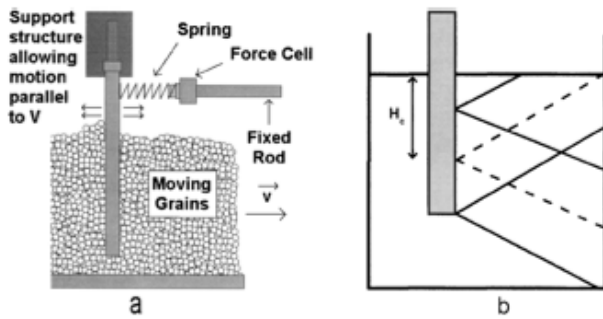


Figure 2.14a Experiment measuring the force acting on a rod injected into a moving granular layer (Taken from Albert [2000, p.5122]).

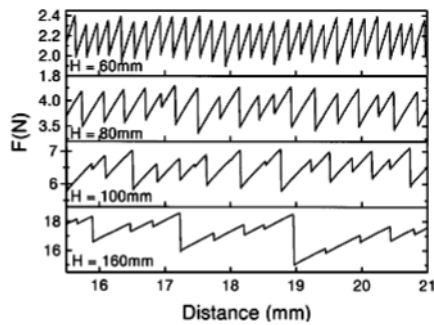


Figure 2.14b Force acting on the rod as a function of distance travelled by the grains for different depths of injection of a rod (Taken from Albert [2000, p.5123]).

Vibration effects have also been tested using the experimental set-up presented in Figure 2.15a. In this experiment a rod is injected into a granular bed at a defined depth. This rod is then subjected to torsional oscillation at a given frequency. At the same time

the granular bed is independently vibrated in a vertical direction at a different frequency.

The granular media vibration is expressed in terms of nondimensional intensity

$$\Gamma = A\varpi^2/g, \quad [2.3]$$

where  $A$ , and  $\varpi$  represent the vibration amplitude and frequency respectively, and  $g$  represents the acceleration of gravity. Figure 2.15b shows the relation between the granular medium frequency response and the applied oscillation torque for different vibration intensities. The experimental results show that, for low torque inputs, an increase in granular medium bed vibration intensity causes a decrease in granular media jamming intensity (resulting with the rod unjamming more easily). It may also be noticed that above a certain rod torque input frequency response becomes independent of bed vibration intensity. The authors of this experiment concluded the “unjamming process to be a statistical, activated like hopping process and that some of the usual statistical concepts of thermal systems can be extended to vibrated granular material” [D’Anna 2008].

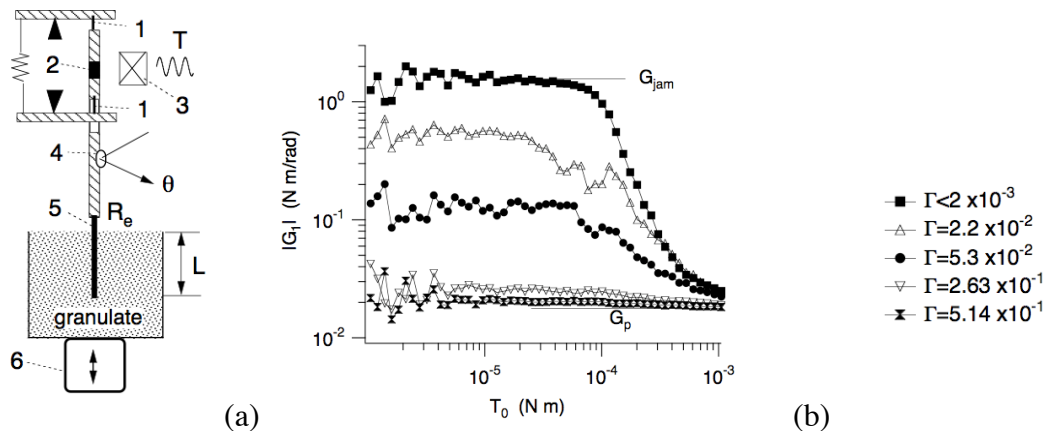


Figure 2.15 (a) Granular media vibration experiment schematic. Experiment was conducted using glass beads used as granular material (Taken from D’Anna [2008, p.011306-1]), (b) Granular media bed vibration intensity response as a function of torque  $T$  applied to the rod for different forced granular bed vibration intensities  $\Gamma$ .  $G$  represents a complex frequency response, obtained from equation  $G = T/\theta$ , where  $\theta$  represents the optically measured angular displacement (Taken from D’Anna [2008, p.011306-2]).

### 2.4.3 Vibration Induced Granular Media Fluidization

Introduction of vibration in granular media flow is also associated with the concept of fluidization. This state of granular media is highly desirable in this project since fluidized granular media would allow for more uniform pressure distribution in the forming process. In the experimental set-up presented in Figure 2.16a a rotating vane is subjected into a vibrated granular bed. For the input vane speed and applied vibration, the torque and power drawn by the motor are measured. The actual vibration intensity is evaluated with an accelerometer. In this experiment, glass beads were tested. The authors of the experiment discovered that there exists a critical vibration intensity  $\Gamma$  (Eq. 2.3) of approximately 1.5-1.6, that allows the sheared granular media to reach the liquefied state at vane rotation speed of approximately 800-1000 RPM, as observed from a discontinuous drop in torque curve in Figure 2.16b. For a vibration intensity that is greater than 1.6, granular media is in the fluidized state throughout the entire range of vane rotation speeds tested. Below the critical vibration intensity of 1.5, no granular media fluidization was observed.

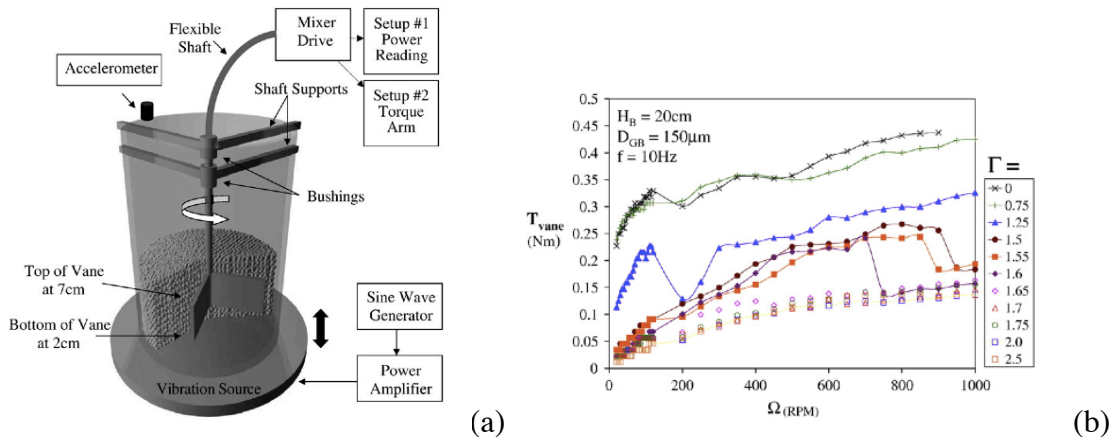


Figure 2.16 (a) Experimental set-up with a rotating vane and vibrated granular bed (Taken from Ford [2009, p.34]), (b) Vane torque versus the rotation speed for different granular media bed vibration intensities (Taken from Ford [2009, p.36]).

In the slow flow regime, vibration may have important effects. In an experimental study similar to the one presented in detail in Figure 2.16a, a layer of glass beads was

subjected to slow rotational speed controlled flow, and the torque was measured [Dijksman, 2011]. The authors observed an interesting behavior of the flow curve (Figure 2.17a), where the vane actually exhibits a torque drop for sufficiently high vane rotational speed. The vane torque is expected to follow the pattern presented in Figure 2.16b for higher rotational speeds. Granular media bed vibrations significantly decrease the required torque at low vane rotational speeds. When the flow approaches the rotational speed for which the torque drop is observed, a much smaller dependence between torque and bed vibration intensity is observed. In torque-controlled experiments, the authors observed hysteresis in the rotational speed when torque was varied between critical values, as presented in Figure 2.17b. The critical torques in Figure 2.17b matched the torques predicted from speed-controlled flow experiment presented in Figure 2.17a. The dropping torque behavior observed in this experiment appears to be material-dependent, since some of the tested materials, like aluminum flakes or PMMA beads, did not exhibit this type of behavior.

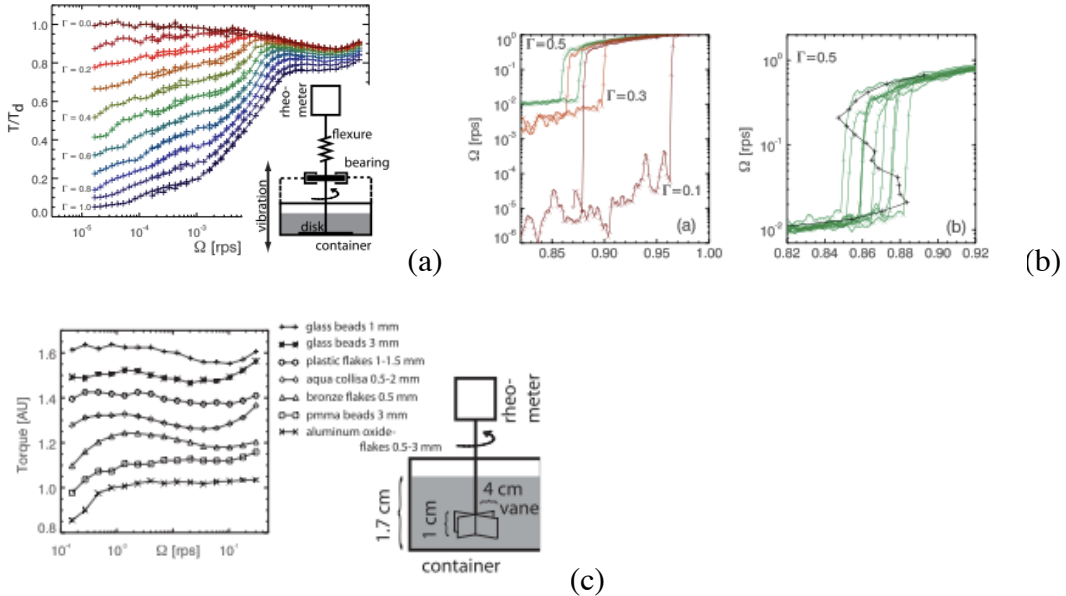


Figure 2.17 (a) Experimental set-up and nondimensionalized torque versus rotational speed for different granular media bed vibration intensities. (Taken from Dijksman [2011]), (b) Hysteresis loops for different values of vibration intensity  $\Gamma$  (Eq. 2.3) in torque-controlled experiments. Horizontal axes represent the nondimensionalized torque (Taken from Dijksman [2011]), (c) Torque-speed behavior for different materials. (Taken from Dijksman [2011]).

Another experimental approach to understand granular media liquefaction uses a vertically shaken granular media bed, as presented in Figure 2.18a [Metcalfe]. When granular media are shaken above a critical intensity, a fluidized layer of granular media occurs in the top layer of the bed, which is schematically presented in Figure 2.18b. For a large vibration intensity, the fluidized layer height is measured, then the vibration intensity is decreased until no fluidized state is observed in the granular bed. In this experiment rough and smooth sand and glass beads were tested. The authors of the study observed that once granular media reached a critical vibration intensity, the vibration intensity may decrease considerably, while still retaining the liquefied layer in the granular media bed, as shown in Figure 2.18c. In this experiment, a critical vibration intensity  $\Gamma$  (Eq. 2.3) for the onset of glass beads fluidization is measured at around 0.4,

which is smaller than the critical vibration intensity in the case of horizontally shaken granular media observed in the rotating vane experiment (approximately 1.65 from Figure 2.16b), and larger than the critical granular media bed vibration intensity in the oscillated rod experiment (smaller than 0.263 from Figure 2.15b). Various experiments generally show a significant discrepancy in granular media bed vibration intensity causing granular media liquefaction. This discrepancy shows that the critical vibration intensity for granular media liquefaction does not appear to be an intrinsic property of granular media.

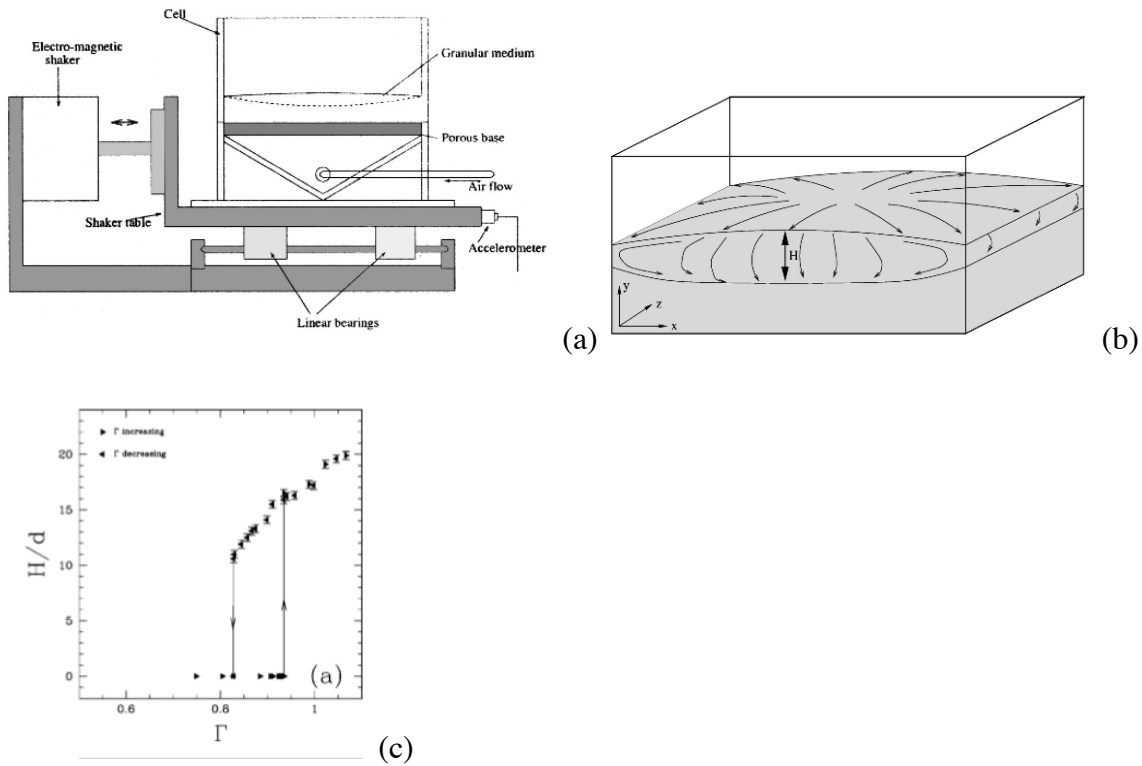


Figure 2.18 (a) Experimental set-up for horizontally shaken granular bed. (Taken from Metcalfe [2002]), (b) Schematic of granular media flow in the fluidized layer. (Taken from Metcalfe [2002]), (c) The height of the liquefied layer with respect to the vibration intensity (Taken from Metcalfe [2002]).

## **2.5. PROPOSED EXPERIMENTAL SET-UP**

In the process of warm forming of materials, granular media will experience both shear and normal stresses. These stresses are known to initiate force chains in granular media, which may lead to jamming behavior. In order to reduce the amount of jamming and allow for a more controlled flow of the granular material, it is suggested to induce vibration in the granular medium during the process of forming. During the literature review, it was determined that it is not common for experimental studies to look into the simultaneous effects of normal stress, shear stress and vibrations in granular media. Therefore, it is required to design an experiment that will incorporate all three of the above effects to provide a better understanding of flow behaviors of granular media, as well as control of this flow in the process of engineering material deformation.

Due to the fact that material forming rates are relatively slow, the direct shear cell presented in Figure 2.5a will serve as a core concept for the experimental set-up design. The low complexity of this design makes it very cost effective when compared to other design concepts. In this study, there is a strong interest in understanding granular media flow under high normal stresses, and the direct shear cell proves to be very useful in high-load testing applications. The direct shear cell design may also be modified to incorporate vibration tests, using an oscillator directly connected to the test rig.

### **III. EXPERIMENTAL INSTRUMENTATION DESIGN**

#### **3.1. PROBLEM STATEMENT**

The research study in this project is motivated by the need to develop new light metal alloy forming technologies for practical application at warm forming temperatures. Hence, the interest is in obtaining new understanding of dense granular media flow theory for application as a force transfer medium, particularly for forming sheet materials.

#### **3.2. DESIGN REQUIREMENTS**

An experimental study of granular media flow is needed for conditions corresponding to light alloy warm forming. The particulate materials will be tested at rates that match the forming rates expected for industrial warm forming of light metal alloys. Granular media will be subjected to pressures required to produce stresses to form light metal alloy sheet. Different granular materials of different size need to be tested in order to determine the most suitable properties in the final granular media selection for a force transfer medium.

#### **3.3. DELIVERABLES**

The main goal of this study is to fabricate a granular media testing apparatus that provides new understanding in the field of granular flow. The experimental study is expected to provide information that is essential to predicting granular media behavior, when utilized as a force transfer medium in warm forming of light metal alloys. Both qualitative and quantitative data analysis and granular media flow theoretical discussions validated by experimental results in the literature are the deliverables for this project.

### 3.4. DESIGN VARIANTS

The direct shear cell experiment, as schematically presented in Figure 3.1, was selected as the granular-media testing method. This design variant was introduced in part 2.4.1.1. This testing geometry was chosen due to the experimental condition requirements determined by slow flow and high pressure. Direct shear cell fabrication requires relatively simple mechanical solutions compared to other experimental instrument approaches presented in the literature review, for example the Couette shear cell.

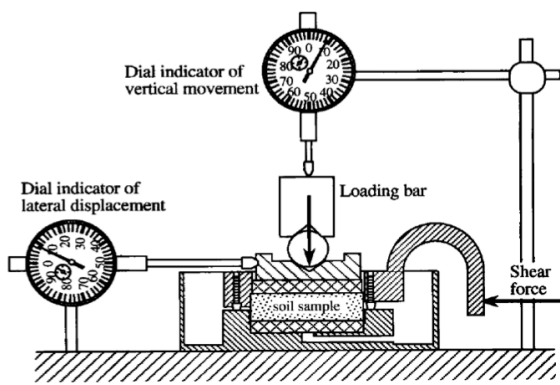


Figure 3.1. Direct shear cell schematic [Figure taken from Puppala].

### 3.5. RELEVANT CALCULATIONS

#### 3.5.1. Normal Stress

To approximate the stresses developed in light metal alloys during biaxial warm forming, forming of aluminum alloy AA5182 was considered. Although the granular media flow experiments are conducted at room temperature, the stresses applied to granular media should emulate actual stresses during the warm forming process. Figure 1.2 introduced in section 1 presents a tensile deformation data fit developed by Chang *et al.*

al. [Chang, 2010]. Based on the selected forming strain rates and temperatures, the Zener-Hollomon parameters were calculated from the equation:

$$Z = \dot{\varepsilon} \exp\left(\frac{Q_c}{RT}\right) \quad [3.1]$$

where  $Q_c = 136$  kJ/mol is the activation for creep,  $\dot{\varepsilon}$  is the strain rate, R is the universal gas constant, and T is absolute temperature. For the given Zener-Hollomon parameter, the approximate material stress was calculated using a fit proposed by Chang. The data fit for the applied stress is normalized by the temperature-dependent Young's modulus for pure aluminum, with the following equation used to incorporate the temperature effect,

$$E = 77,630 - 12.98T - 0.03084T^2, \quad [3.2]$$

where E is in MPa and T is in K. For the simulated strain rates of  $3 \times 10^{-2}$ ,  $10^{-2}$ ,  $3 \times 10^{-3}$ , and  $10^{-3}$  s<sup>-1</sup> and forming temperatures of 150 and 350°C, calculated Zener-Hollomon parameters were in the range between  $10^{12}$  and  $2 \times 10^{15}$  s<sup>-1</sup>. Within this range of Z parameters, the following equation may be used to approximate stress in the deformed material,

$$Z = 10,760 \exp(5867\sigma/E), \quad [3.3]$$

where Z is in the units of s<sup>-1</sup>. Based on these material stresses, the required bulge forming pressure p was approximated using the spherical pressure vessel model [Craig, 2011, p.607],

$$\sigma = \frac{pr}{2t} \quad [3.4]$$

where r represents the sphere radius (estimated at 20 mm) and t represents the sphere/bulge thickness (estimated at 1 mm). The material stress  $\sigma$  is expected to range between approximately 46 to 290 MPa, which requires the forming pressure on the order of 4.6 to 29 MPa. The calculated forming pressure p defines the normal stress  $\sigma_n$  applied to the granular media. Based on the load plate area A, the normal load P applied to the top shear cell plate was calculated from the equation:

$$\sigma_n = \frac{P}{A} \quad [3.5]$$

The test instrument uses a load plate with a total surface area of 20 cm<sup>2</sup>. Hence, the expected forming pressure requires that the normal load applied to granular media varies between 2000 lbs (8.9 kN) to simulate forming at 350°C, to 13000 lbs (57.8 kN) for forming at 150°C.

### 3.5.2. Shear Rate

It is important to relate the shear rates during granular media experiments to strain rates during material deformation. The shear rate applied to granular media should correspond with tensile test strain rates selected when determining the material stress developed during warm forming. The effective uniaxial strain increment may be represented as [Dieter, 1961]:

$$d\bar{\varepsilon} = \left[ \frac{2}{3} (d\varepsilon_1^2 + d\varepsilon_2^2 + d\varepsilon_3^2) \right]^{1/2} \quad [3.6]$$

For the plain strain case, the strain increments may be represented in terms of shear strain as:

$$d\varepsilon_1 = \frac{d\gamma}{2}, \quad d\varepsilon_2 = -\frac{d\gamma}{2}, \quad d\varepsilon_3 = 0 \quad [3.7]$$

When representing the uniaxial effective strain increment in terms of shear strain, equation 3.6 could be written as:

$$d\bar{\varepsilon} = \left[ \frac{1}{3} (d\gamma^2) \right]^{1/2} \quad [3.8]$$

By taking a time derivative of equation 3.8, a relation between uniaxial strain rate and shear rate may be obtained as follows:

$$\dot{\bar{\varepsilon}} = \frac{1}{\sqrt{3}} \dot{\gamma} \quad [3.9]$$

For the selected shear cell cavity height, H, and shear rate,  $\dot{\gamma}$ , a required shear cell velocity can be obtained from relation:

$$v = H\dot{\gamma} \quad [3.10]$$

### **3.5.3. DC Motor Selection**

The shear cell is driven by an electric motor and screw jack system. The motor is expected to supply relatively high torque at low rotational speeds. The motor speed is also expected to stay constant during the experiments. Hence, a geared DC motor was selected. When specifying a DC gearmotor, both maximum power rating and rotational speed need to be provided.

The maximum shear cell velocity may be represented as:

$$v = \frac{n}{60} d \quad [3.11]$$

where n represents motor rpm and d represents the travel distance per turn of the screw jack. The system uses a screw jack with a travel distance per turn of 1/25 in. For the maximum expected shear cell velocity of 1 mm/s the maximum motor rotational speed will be no less than 60 rpm.

The minimum required motor power is calculated from the following equation:

$$P = Fv \quad [3.12]$$

For a maximum estimated shear force of 50kN and maximum shear cell travel speed of 1mm/s the motor should be rated at 50W at minimum.

### **3.5.4. Load Lever Analysis**

A high normal force needs to be applied to the granular media to simulate the pressure of forming, and it would be impractical to directly apply loads this great by weight alone, as calculated in section 3.5.1. Thus, a lever system was designed to apply normal loads. When selecting an appropriate material and geometry for the lever, a simply supported beam model was initially chosen and studied using Finite Element Analysis (FEA). The simply supported beam schematic utilized in the analysis is presented in Figure 3.2. Point A represents a pivot point, point B represents a position

where force is being applied to granular media, and point C represents a point where the normal force is applied to the lever using known weights.

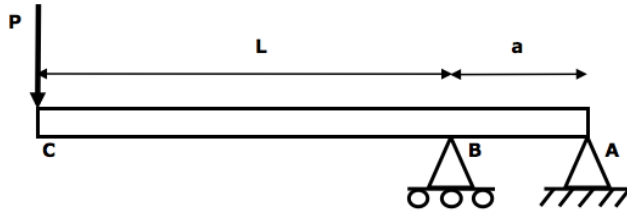


Figure 3.2. Simply Supported Beam

For this particular lever geometry, the ratio of reaction force at B to the normal force P is:

$$\frac{B_y}{P} = \frac{L+a}{a} \quad [3.13]$$

The maximum bending moment,  $M_B$ , in the lever occurs at point B. Hence, the maximum normal stress in the beam due to bending is [Craig, 2011, p.363]:

$$\sigma = \frac{M_B y}{I} = \frac{PLy}{I} \quad [3.14]$$

where  $y$  represents the distance from the neutral axis to the beam surface, and  $I$  represents the second moment of inertia about the neutral axis.

Maximum deflection can be calculated using the superposition method. The deflection angle at point B,  $\theta_B$ , and corresponding beam deflection at A due to the bending moment,  $\delta_1$ , may be obtained from the equations below [Craig, 2011,p.E-3]:

$$\theta_B = \frac{M_B a}{3EI}, \quad [3.15]$$

$$\delta_1 = \theta_B L \quad [3.16]$$

Beam deflection due to the normal force P applied at point A,  $\delta_2$ , may be calculated from [Craig, 2011, p.E-1]:

$$\delta_2 = \frac{PL^3}{3EI} \quad [3.17]$$

Finally, the total beam deflection at point A may be represented as the sum of the corresponding deflections.

$$\delta_{tot} = \sum_{i=1}^n \delta_i = \delta_1 + \delta_2 \quad [3.18]$$

In the current design the maximum load applied to the granular media (reaction at B in Figure 3.2) equals 2000 lbs. This constraint is determined by the maximum load allowed by the load cell attached to the lever and the load capacity of the linear slider attached to the bottom shear cell cavity. The design selected assumes a lever made of a 6105 – T5 aluminum T slotted extrusion, with a yield strength of 35 ksi.

For a lever arm with  $a = 3.5$  in. and a lever with the required mechanical advantage of 8.5, the maximum tensile stress due to bending in the lever equals 26 ksi, which produces a safety factor of 1.35. The maximum deflection is calculated at 0.23 in.

FEA was conducted to ensure design safety using the Ansys Workbench software platform. In this analysis the actual lever geometry, as proposed in the final instrument fabrication stage, was applied. According to the FEA analysis the lever should not yield when the maximum allowed load ( $P = 235$  lbs.) is applied. The lever deflection at the point of load application is predicted to be 0.21 in., and is close to the value calculated using equation 3.18. The FEA stress analysis is presented in Figure 3.3.

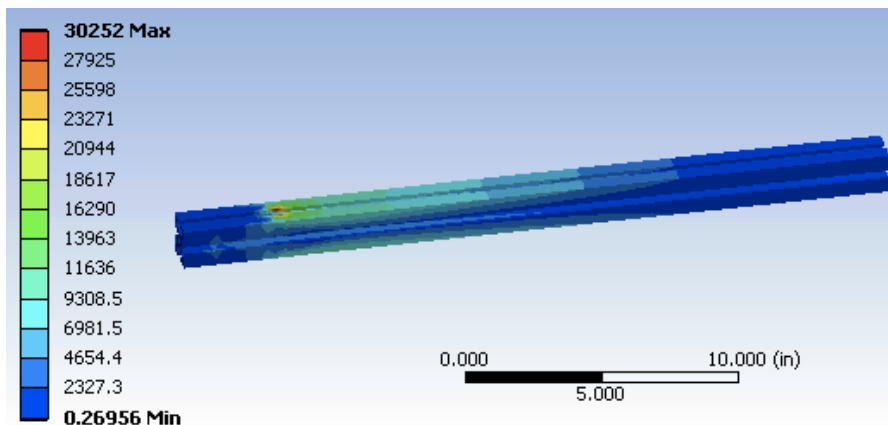


Figure 3.3. Lever arm stress analysis [units in psi].

During oscillating normal load experiments an upward force is applied to the lever using a pneumatic cylinder. The force step input causes beam vibrations, which result in an oscillating normal force applied to the granular material at point B in Figure 3.2. A harmonic oscillator analysis was utilized to predict the vibration of the system. A beam model is presented in Figure 3.4, with  $M$  representing the effective mass associated with the weight applied to the beam,  $k$  representing an effective spring constant of the lever and  $b$  representing the damping coefficient of the beam. The lever is modeled as a rigid body.

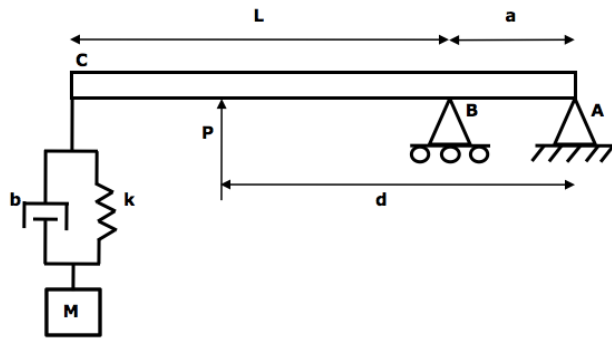


Figure 3.4. Model used in beam vibration analysis. In the implemented design  $a=2.5$  in.,  $d= 16$  in.,  $L=18.75$  in.

A bond graph analysis results in a second order differential equation

$$M\ddot{x} + b\dot{x} + kx = U \quad [3.19]$$

$U$  represents an effective load applied to the beam. The damping coefficient may be obtained from analysis of experimental data [Graham]. The effective spring constant of the lever may be determined when the system is analyzed at its steady state with no pressure applied, when terms  $\dot{x}$  and  $\ddot{x}$  have values of zero, and the equation may be represented as

$$U = k\delta_{tot}, \quad [3.20]$$

where  $\delta_{tot}$  is the deflection at the end of the beam. The total deflection may be obtained using equations 3.15, 3.16, and 3.17, which provide the lever's effective spring constant:

$$k = \frac{3EI}{L^3 + L^2a} \quad [3.21]$$

### 3.5.5. Shear Pin Geometry

As a safety measure, a shear pin was designed to serve as a link between the mechanical drive and the bottom shear cell cavity. The shear pin is supported at both ends by the cavity, while the shear force is applied at its center by the screw jack clevis-end mounting attachment. Brass was selected as the pin material. Two notches are machined in the shear pin between the clevis mount and the shear cell cavity support. The shear pin is designed to fail in shear at the notches in order to not overload the drive mechanisms.

Initially, the pin was modeled as the simply supported beam presented in Figure 3.5, with reaction forces at A and B representing the contacts with the shear cell cavity, and uniformly distributed load P representing the shear force applied. Shear stress in a circular beam of cross sectional area A and diameter D equals [Gere, 2003, p.344]:

$$\sigma_t = \frac{4V}{3A} = \frac{16V}{3\pi D^2} \quad [3.22]$$

where V represents the shear force, which equals  $0.5P$  in the gap region, A is the cross-sectional area and D is the diameter. The maximum allowed shear force equals 1 ton, which is determined by the load capacity of the screw jack. The shear strength and typical tensile strength for standard 360-alloy brass in the soft condition are 30 and 50 ksi, respectively [Free-Cutting of Brass]. If the shear pin was required to fail at 85% of the maximum load, then the required shear pin diameter at the center of the notch D equals 0.23 in.

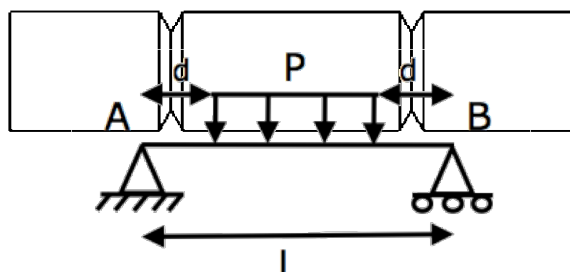


Figure 3.5. Simply supported beam representing the shear pin

FEA conducted in Ansys Workbench was also applied to the shear pin as presented in Figure 3.6 below. A shear pin with a notch diameter of 0.23 in. was analyzed in the FEA. The analysis represents the shear stress in the shear pin when the maximum allowed shear force is applied. The maximum shear stress at the lowest point of the notch represents approximately 160% of the shear strength of brass, which ensures that the shear pin will fracture before the maximum allowed load is reached.

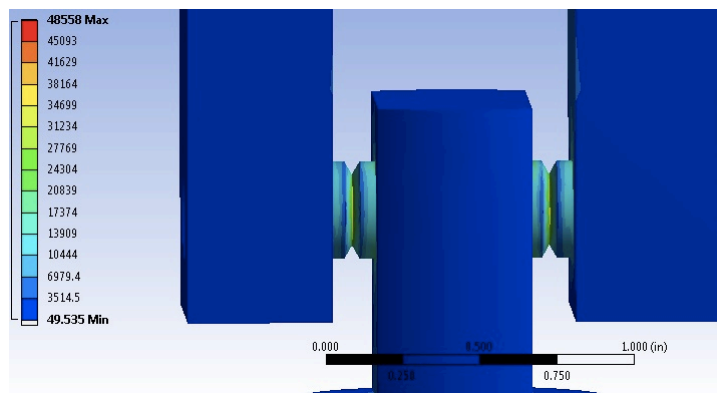


Figure 3.6. Shear pin shear stress FEA results [units in psi].

### 3.6. FINAL MODEL IN CAD

The entire instrument was designed using SolidWorks Computer Aided Design (CAD) software. Modeling the instrument in CAD allowed for a thorough stress and deformation analysis on multiple components, which allowed validating the design choices. The computer model is of assistance when redesign is required. Figure 3.7 presents an isometric view of the final design of the instrument fabricated and utilized during the granular media shear test study. The experimental apparatus consists of 5 major subsystems, as presented in the form of exploded views in Figure 3.8. The major subsystems include: frame, shear cell cavities, load application structure, electro-mechanical drive system, and pneumatic vibration actuator.

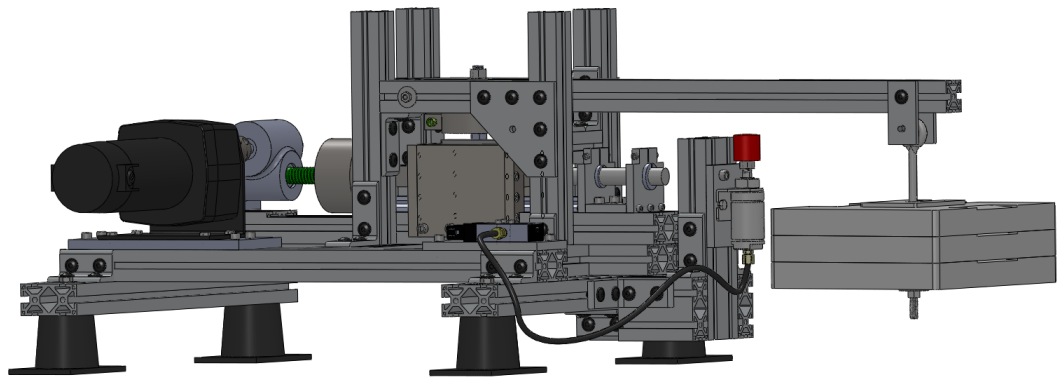


Figure 3.7. Isometric view, representing the CAD model of the direct shear cell.

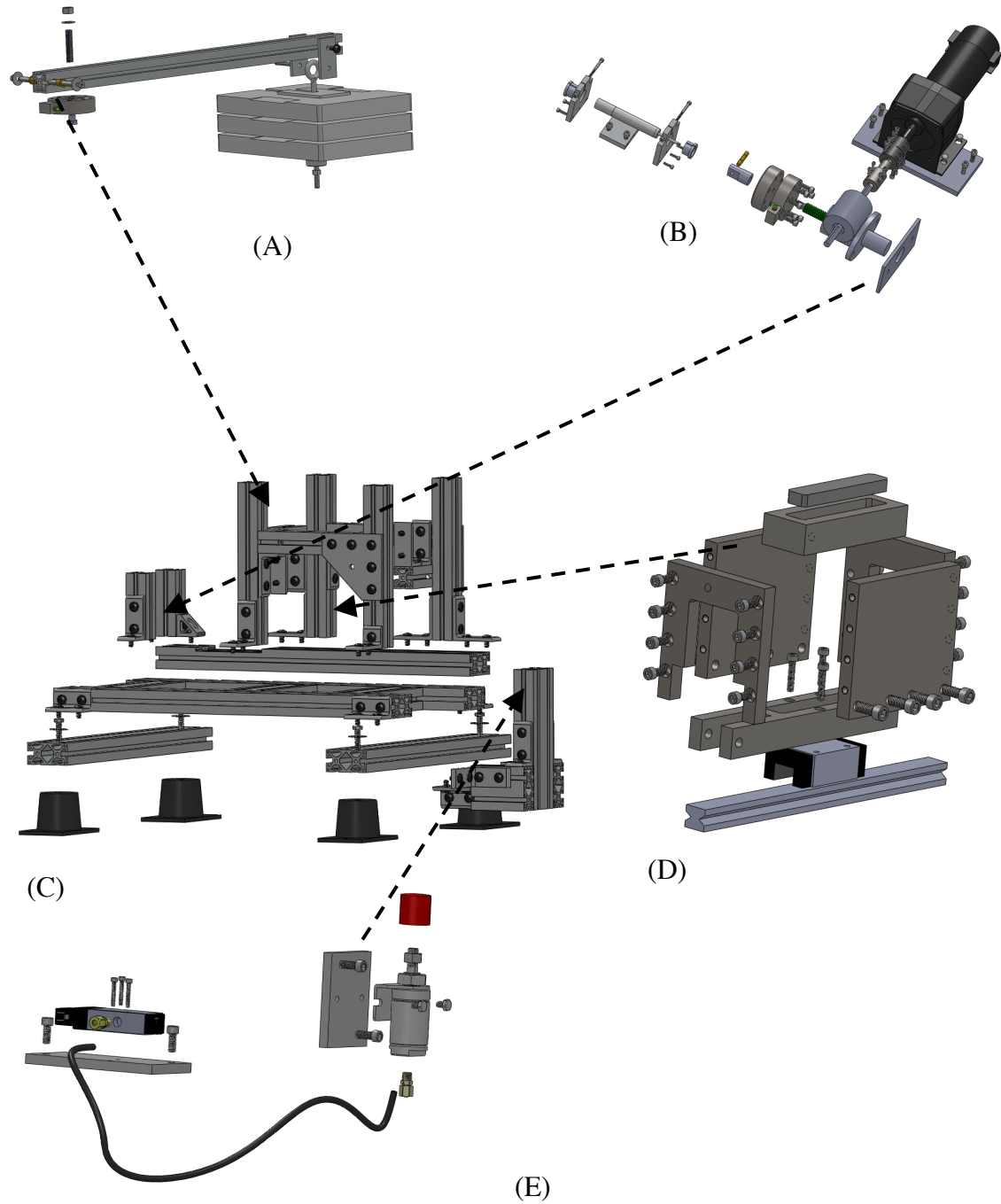


Figure 3.8. Direct shear cell major subsystems: A) Load application system, B) DC motor drive system, C) Frame, D) Shear cell cavities, E) Pneumatic vibration actuator.

### **3.6.1. Frame**

The frame (Figure 3.8c) is constructed of aluminum T slotted extrusions made out of 6105 – T5 aluminum, also used in the lever design. Aluminum extrusions allow for relatively good machinability and sufficient yield strength. By introducing screw fastened joints the instrument may be relatively easily adjusted to incorporate new design variants. The entire frame remains attached to the floor through vibration isolators made out of neoprene rubber.

### **3.6.2. Shear Cell Cavity System**

The granular media is contained in a 2-cavity system (Figure 3.8d). Both cavities are made of A2 tool steel. It is desired to maximize the hardness of the cavity material to ensure that the granular media does not cause cavity wear during testing. Following the machining process, the cavities were subjected to the recommend heat-treating practices in the ASM Handbook [Heat Treating of Specific Steels]. The final hardness of the top and bottom cavities was measured to be 58.2 and 51.7 respectively on the Rockwell Hardness C scale. The top cavity remains fixed to the frame using a support structure made of 4 steel plates. A shim plate is placed between the top and bottom cavity, while the top cavity is fixed to the frame. Subsequently, the shim plate is removed. The bottom cavity is allowed to translate in one direction by attaching it to a linear slider, which translates on a rail attached to the frame. The maximum load capacity of the linear slider is 3102 lbs. There is a small air gap between the two cavities, which isolates the shear force due to flow of granular media from the friction between the cavities. The surfaces of both cavities were ground to increase the tolerance of the space between the cavities, and allow for relatively small particulate material testing. The bottom shear cell is attached to the drive mechanism using a shear pin, which is designed to fail when the maximum allowed load is exceeded. Shear cell cavities and top cavity support structure technical drawings are attached in the Appendix A.

### **3.6.3. Drive Mechanism**

The drive system (Figure 3.8b) consists of a 1/4 hp parallel shaft DC gearmotor and an upright style screw jack mechanism. The maximum speed of the motor is 62 rpm. The motor controller allows for manual speed control. The maximum load capacity of the screw jack equals 1 ton, which determines the maximum load capacity of the drive system.

Both screw jack and the DC motor are attached to the frame, using custom made brackets. The motor is connected to the screw jack using shaft couplers. A compression/tension pancake style load cell is attached in-line between the screw jack and the bottom shear cell cavity. The maximum load capacity of the load cell equals 5000 lbs [See Load Cell Model 41 in Appendix B for more detailed specifications]. The load cell is connected to a Honeywell signal-conditioning unit (SC1000), which feeds the load data directly to the computer via an RS232 serial port. A clevis-end mounting attachment allows connecting the load cell with the bottom shear cell cavity, with the shear pin. The shear pin is designed to fail in shear when the drive load reaches approximately 70% of the maximum allowed load. A spring return AC-AC Linear Variable Differential Transformer [LVDT] is mounted to the frame on the opposite side of the bottom shear cell cavity [See LVDT VL7A in Appendix C for detailed specifications]. The LVDT measures the relative position of the bottom cavity with respect to the top cavity, which remains stationary during the experiments. Acquiring both time and displacement data allows for speed measurement of the shear cell. The LVDT is connected to the Honeywell signal-conditioning unit, which feeds the data directly to the computer.

### **3.6.4. Load Application Structure**

A normal force is applied to the granular media using known weights and a lever arm, as presented in Figure 3.8a. Two alloy 954 bronze flanged-sleeve bearings are pressed into the lever arm, to allow the lever to pivot about the precision shaft attached to the frame. The load in the bushings should not exceed 4500psi. A compression load cell

with a maximum capacity of 2000 lbs is attached to the lever [See Load Cell model LCHD-2k in Appendix D for more detailed specifications]. The load button attached to the load cell is in direct contact with the top load plate contacting the granular media in the test cavity. The load cell is connected to a Vishay 2100 signal-conditioning unit, which feeds an amplified signal to the National Instruments data acquisition module NI USB 6210.

### **3.6.5. Pneumatic Vibration Actuator**

During the experiments it is of interest to determine the properties characteristic to granular media continuously loaded and unloaded while undergoing shear. The pneumatic actuator shown in Figure 3.8e applies an upward force to the lever, which allows for continuous variation of the normal force applied to the granular media. An air cylinder is attached to the frame through a custom-made bracket. A threaded polyurethane rubber bumper is attached at the end of the air cylinder shaft in order to reduce vibrations during application of force by this actuator. The frequency of the oscillations is controlled with a 2-way single-solenoid valve [See Solenoid Valve Appendix E for specifications and valve connection schematic]. The operation of the solenoid valve is controlled with the NI USB 6210 module. The module sends a digital square input signal into the solid-state relay, which controls the power supply to the solenoid valve [See Solid State Relay Appendix F for specifications and electrical connection diagram]. The pressures of operation of the solenoid valve are rated at 29-145 psi. The operating air pressure is supplied from laboratory compressed air lines and the input pressure is controlled with a manually adjusted pressure regulator.

## **3.7. FINAL INSTRUMENT DESIGN**

Following the design stage, a direct shear cell instrument was fabricated. Figure 3.9 presents a photograph of the direct shear cell apparatus utilized for the experimental study. Figure 3.10 presents the entire experimental set-up including the data acquisition

system, signal conditioners, and compressed air supply lines. Instrument operation procedures are thoroughly presented in the following chapter.

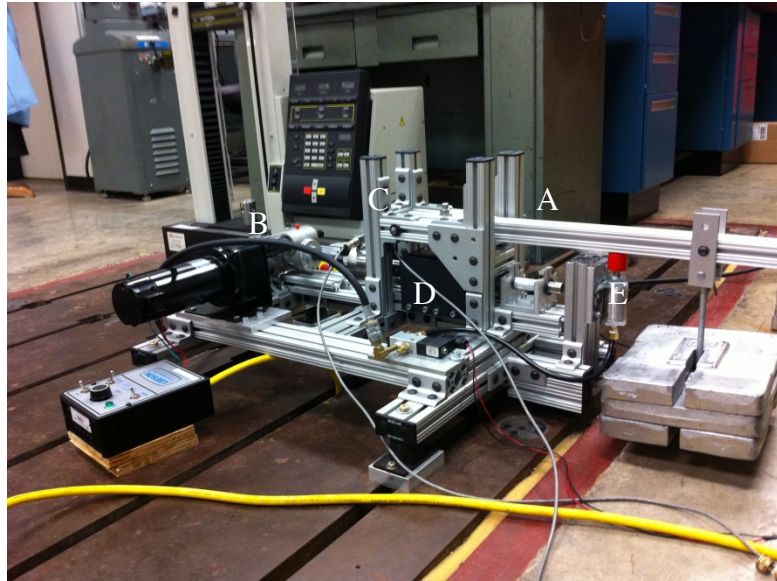


Figure 3.9. Direct shear cell fabricated according to the computer-aided design. A) Load application system, B) DC motor drive system, C) Frame, D) Shear cell cavities, E) Pneumatic vibration actuator.

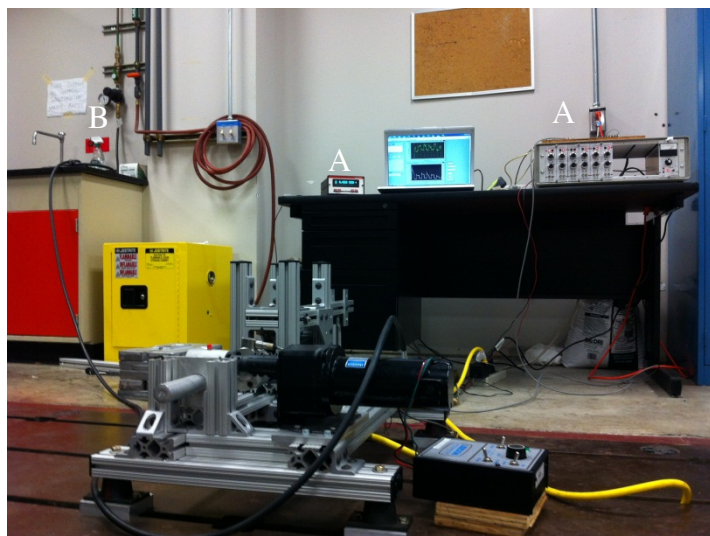


Figure 3.10. Entire experimental set-up utilized in experiments. A) Signal Conditioners, B) Compressed air supply lines.

## IV. EXPERIMENTAL PROCEDURE

### 4.1. INSTRUMENT OPERATION INSTRUCTIONS

#### 4.1.1. Initial Instrument Calibration

The Vishay 2100 signal conditioner presented in Figure 4.1 was used with a load cell to calibrate the normal force applied to the shear cell. Currently, the instrument uses a LCHD-2K load cell from Omega [Appendix D] to measure the normal force applied to the shear cell by the loading arm. This load cell can measure a maximum load of 2000 lbs, which is calibrated to the maximum signal output of 10 V.



Figure 4.1. Vishay 2100 Signal Conditioning Module.

Initially, the load cell signal output is properly balanced. In order to balance the signal, set the conditioner excitation at 10V, and with no load applied to the load cell adjust the ‘Balance’ knob until the conditioner diodes turn dim. The conditioner signal output should read 0 V. The Vishay signal-conditioning unit manual is provided in room MER 1.406. The maximum allowed signal input into the data acquisition NI USB 6210 module is 10V, and the maximum load cell output is 30 mV, hence the signal amplifier gain knob should be adjusted approximately 333. A calibration curve should be obtained by plotting the load vs. the signal output. The load cell calibration curve is presented in Figure 4.2. The cable attached to the LCHD-2K load cell was custom made. Load cell wire connectors are presented in Table 4.1.

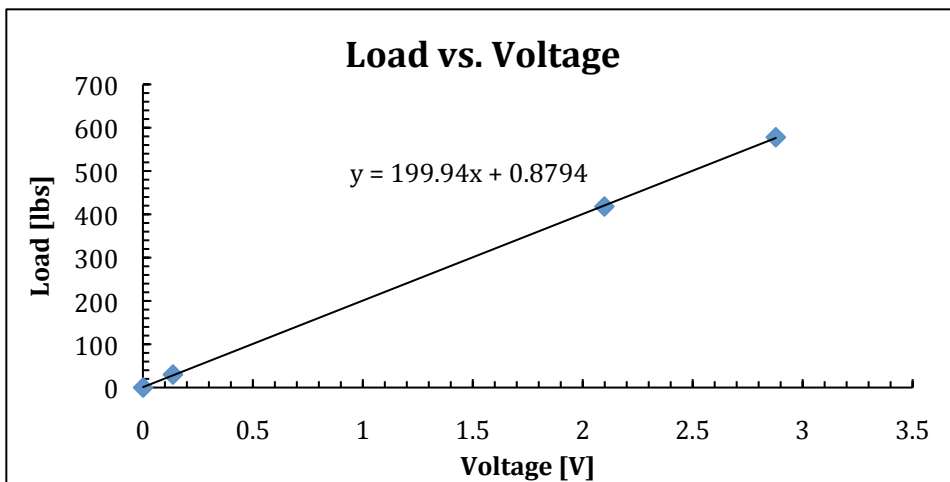


Figure 4.2. Calibration curve for the LCHD-2K load cell attached to the lever arm

Table 4.1. Load cell LCHD-2K wire connector designation.

WIRE COLOR	DESIGNATION
WHITE	EXCITATION (+)
BLACK	EXCITATION (-)
RED	SIGNAL OUTPUT (+)
GREEN	SIGNAL OUTPUT (-)

#### 4.1.2. Shear Pin Placement

Ensure the shear pin presented in Figure 4.3a is in the right position. The machined grooves should be spaced inside the gaps between the clevis end mount and the bottom shear cell cavity as presented in Figure 4.3b.



(a)



(b)

Figure 4.3. a) Shear pin, b) Shear pin adjustment.

#### 4.1.3. Shear Cell Cavity and LVDT Adjustment

In order to adjust the bottom cavity position first turn on the DC motor. Next, release the brake and slowly move the bottom shear cell to the desired position. Figure 4.4 presents the DC motor SCR thyristor controller front panel, as well as the controller adjustments. The potentiometer labeled IR COMP is responsible for maintaining constant speed when the motor load changes. The Leeson DC motor controller operation manual is provided in room MER 1.406.



(a)



(b)

Figure 4.4. a) Motor front panel speed knob adjustment and switches, b) Motor controller adjustments.

Using the motor controller, center the shear cell cavities as presented in Figure 4.5a. The SC1000 transducer display and signal-conditioning unit, which conditions the signal from the LVDT and the load cell attached to the screw jack, is shown in Figure 4.5b. While the LVDT measurement is being displayed on the signal conditioner, adjust the LVDT position on the rail until the zero measurement is displayed. Fix the LVDT in this position, as shown in Figure 4.5c.



(a) Shear cell aligned



(b) LVDT display



(c) LVDT

Figure 4.5. a) Top and bottom shear cell cavities are aligned, b) SC1000 transducer display and signal conditioning unit with LVDT display for aligned shear cells, c) LVDT position adjusted and fixed.

#### 4.1.4. Placing Granular Media in the Cavities

Before pouring granular media into the shear cell the size of the gap between the top and bottom cavities should be inspected and adjusted, if necessary. The gap size between the cavities should be smaller than the minimum granule size to ensure that all

the particles remain within the test space during the experiment. Insert an appropriate amount of granular media, as presented in Figure 4.6. For the tests conducted in this study, the initial granular media bed height was set to approximately 40 mm.



Figure 4.6. Steel bearing balls placed inside the cavities.

#### 4.1.4.1 Sand Sieving

In order to obtain sand of a known grain size, a sieve mesh system was used. The sieve assembly is presented in Figure 4.7a. The sieve mesh sizes were obtained according to the ASTM E-11 standard sieve specification. Three sets of sieve mesh sizes were available during the experiments, with opening sizes of 2mm, 1mm, and 0.5mm. The as-received sand was sieved through the sieve assembly, with mesh size ordered from coarse to fine. Figure 4.7b presents the shear cell cavity containing sand of grain size between 1mm and 2mm.



(a)



(b)

Figure 4.7 (a) Sand Sieves, (b) Sieved sand placed in the cavities.

#### **4.1.5. Load Plate Adjustment**

Set the motor adjustment to ‘forward’ rotation, and slowly move the bottom shear cavity to the ‘-10 mm’ (per LVDT) position. Place a load plate on top of the granular media bed. Lower the loading lever and ensure that the load button attached to the load cell is contacting the load plate. Position the load plate parallel to the top shear cell cavity surface, as pictured in Figure 4.8. During the course of the experiment, the granular media causes the load plate to tilt. In order to prevent jamming of the load plate into the top shear cell cavity it is recommended to use additional insert plates underneath the load plate. The insert plates should shim the load plate above the level at which the load plate jamming occurs.



Figure 4.8. Load cell and load plate.

#### **4.1.6. Lever Load Application**

Apply an appropriate load to the lever by hanging weights on the support base attached to the eyebolt, as presented in Figure 4.9. The eyebolt contacts a load pin, which fits through the joint plates attached to the lever. The eyebolt should be centered on the load pin to minimize stress in the lever. The current lever advantage setting allows a maximum load applied on the eyebolt of approximately 230 lbs. When applying weights to the lever, ensure that the normal load applied to the shear cell cavities does not exceed 2000 lbs, which is the limitation of the load cell. The output of the load cell should not exceed 10V, which is the data acquisition system limitation.



Figure 4.9. Load applied to the lever.

#### 4.1.7. Static Load Test

The amplified output from the Vishay 2100 conditioner should be connected to the NI USB 6210 data acquisition module presented in Figure 4.10 at pins AIGND (black) and AI 1 (red). Initiate the data acquisition software, which acquires the LVDT displacement and load cell outputs. The LabVIEW program ‘Shear and Normal Load DAQ.vi’ automatically saves the shear force and LVDT displacement to a text file, with a file path defined by the user in the program. A computer internal clock timestamp precedes every shear force and displacement measurement. The user interface is presented in Figure 4.11. The program displays the shear force vs. displacement; shear cell displacement speed; and normal load vs. time. The plots are automatically updated while the experiment is conducted. The normal load data can be retrieved after the test by exporting the data from the graph. Any preload applied to the load cell prior to the experiment should be subtracted from the normal load measurement.

Prior to the experiment, set the motor to ‘reverse’ rotation. Apply the required bottom shear cavity speed using the motor control speed knob adjustment. Shear cell cavity speed corresponds to shear rate according to Eq. 3.10. Upon reaching the bottom cavity displacement limit of ‘10 mm’, set the motor speed to zero and stop the data acquisition program. Finally, unload the lever and return the bottom cavity to the initial test position at ‘-10 mm’.

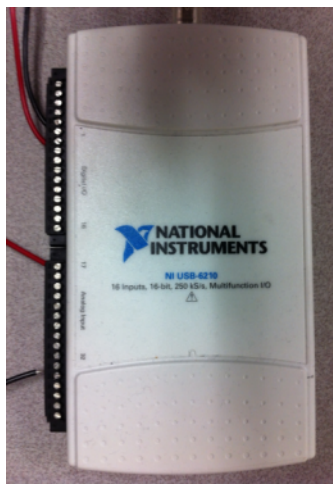


Figure 4.10. NI USB 6210 Data Acquisition module.

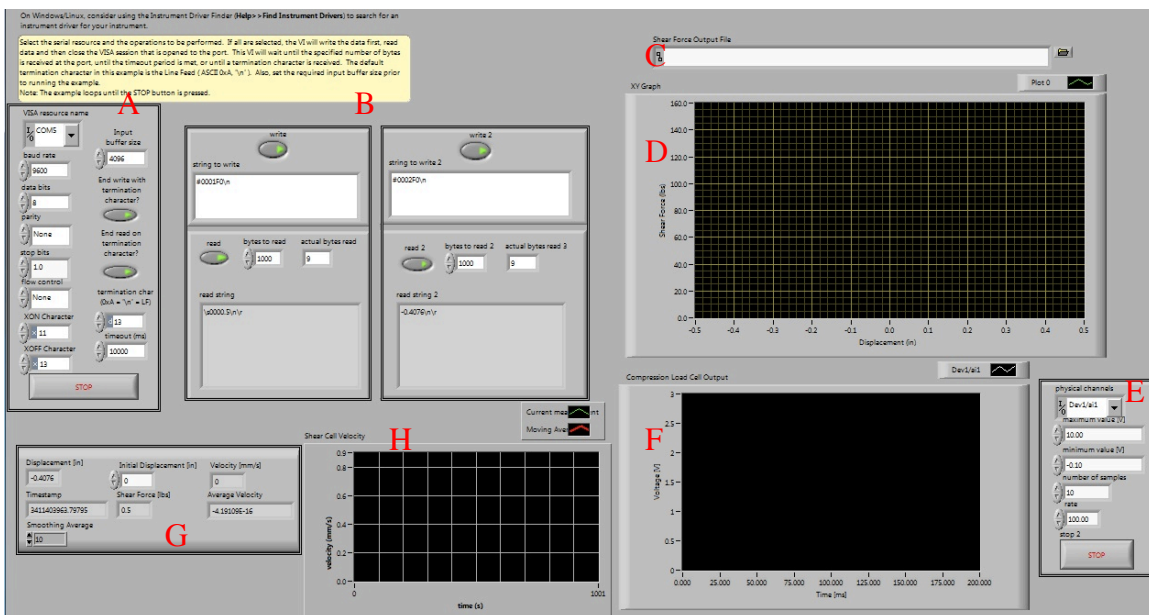


Figure 4.11. Data acquisition front panel: A) RS232 port communication settings, B) Input and output commands from SC1000 Signal Conditioner, C) Shear force and displacement output file path, D) Shear force vs. displacement plot, E) Normal load acquisition settings, F) Normal load vs. time plot, G) Shear speed output, H) Shear speed vs. time plot.

#### **4.1.7.1. Loose Packed Experiment**

When conducting loose packed tests, carefully stir the granular media bed after having completed 1 to 2 tests in order to ensure that the packing density does not increase substantially during the tests. Having finished the low-packing-density tests, use calipers to measure the final top load plate displacement, in order to determine the packing density of the granular media in the shear bed. The known load plate displacement allows obtaining the volume of the shear cell cavity  $V$ , and the random packing density  $\eta_{rand}$  may be calculated from equation below:

$$\eta_{rand} = \frac{m/\rho}{V} \quad [4.1]$$

where  $m$  is the total mass of granular media inside the shear cell, and  $\rho$  is the density of the granular media material. Loose random packing density for spheres is estimated at 0.59 to 0.6 [Dullien, 1992].

#### **4.1.7.2. Dense Packed Experiment**

Prior to a dense packing test, when the shear cell cavities are centered, apply force oscillations to the granular media bed via the pneumatic vibration actuator (PVA). The pneumatic vibration actuator electronic controller box should be connected to a 24V DC power supply. The control input signal to the solid-state relay should be connected to the NI USB 6210 data acquisition instrument at pins labeled PFI5 (red wire) and DGND (black wire). Electrical set-up is presented in Figure 4.12, and a relay connection diagram is provided in the Appendix F.

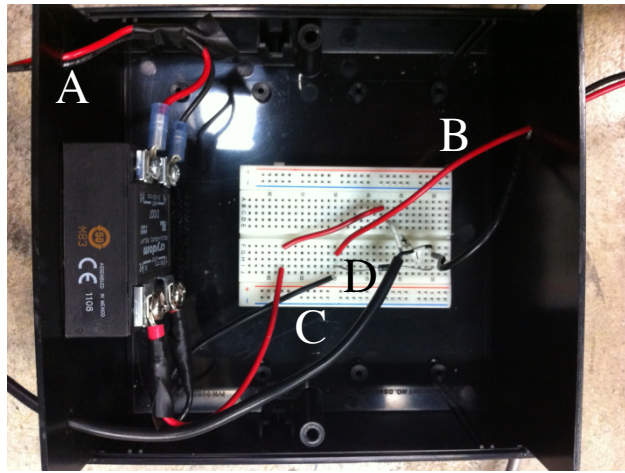


Figure 4.12. Electrical set-up of the pneumatic vibration actuator. (A) Square wave input signal connection from NI USB 6210, (B) Output signal connected to the solenoid valve, (C) 24 VDC power supply, (D) fast recovery diode for transient protection.

When setting up the compressed air supply, follow the description provided in Figure 4.13. Link the compressed air supply to the solenoid valve using the quick disconnect fitting. The LabVIEW program ‘PVA control and Normal Load DAQ.vi’, provides control of the frequency of the solenoid valve operation, as well as acquisition of the data from the load cell measuring the normal force. Apply the required testing load to the lever, set the vibration frequency input to 2 Hz, and adjust the air pressure regulator to approximately 30 psi. Check the system for air leaks before starting the program. Allow the lever force to oscillate for approximately 150 s. Repeat the process when the bottom cavity is at the ‘-10 mm’ position prior to the static load test. Before the first low load test, slowly move the bottom shear cell cavity from the centered position to ‘10 mm’ position, while oscillating the normal load. Once, the granular media packing density has increased, a standard static load test procedure is applied. After the experiments, measure the final top load plate displacement, and calculate the packing density of the granular media within the shear bed from Eq. 4.1, which is expected to fall within the close random packing density bracket from 0.625 to 0.641 [Dullien, 1992].

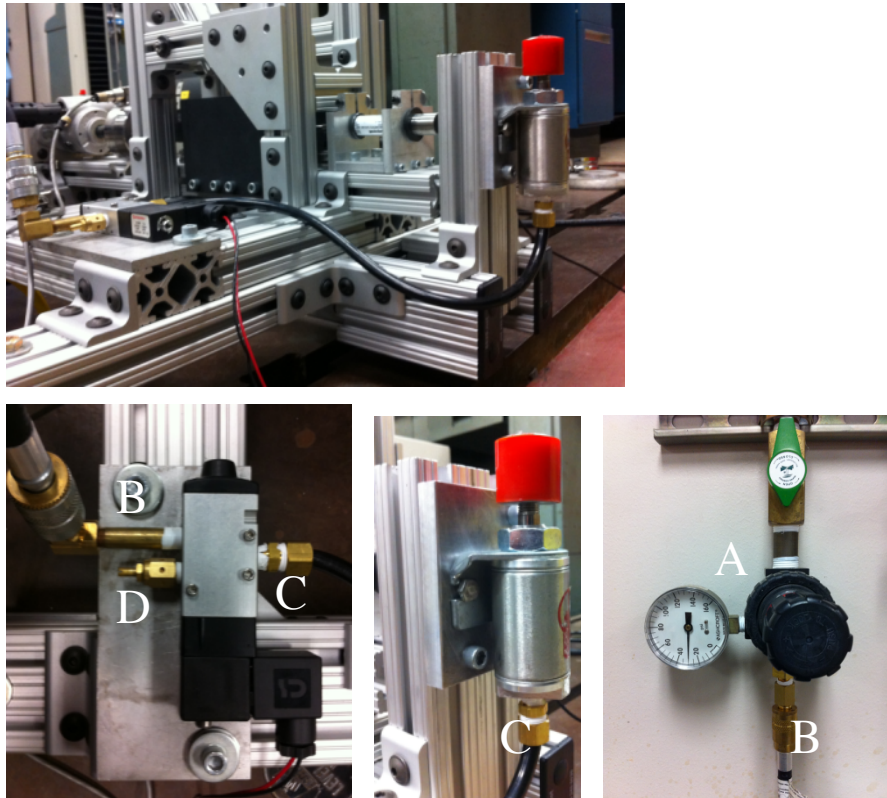


Figure 4.13. Pneumatic Vibration Actuator: A) Pressure gauge (B) compressed air supply, (C) air cylinder pressure line, (D) solenoid valve exhaust with attached muffler.

#### 4.1.8. Granular Media Oscillating Load Shear Test Procedure.

In this set of experiments the normal load applied to granular media in the shear cavity is oscillated about a mean value with a constant frequency while the bottom shear cell cavity is moved at a constant rate, according to the procedure defined in part 4.1.7. The oscillating force is applied to the lever arm using the pneumatic vibration actuator (PVA). The instructions for PVA operation are provided in part 4.1.7.2. Prior to the experiment, the desired oscillation frequency is defined in the ‘Shear and Normal Load PVA DAQ.vi’ program. The force amplitude is controlled using the air pressure regulation valve. During the experiment, the position of the lever arm may change; hence, it is important to leave a small gap at approximately 5-10mm between the top of the

rubber bumper attached to the air cylinder and the lever arm. The space should be smaller than the cylinder stroke length of 0.5 in. This adjustment ensures that the piston is in contact with the lever arm only when the air pressure is being applied. Figure 4.14 shows a recommended initial position of the air cylinder. The lever moment arm is approximately 16in. at the piston location.



Figure 4.14. Adjusting the air cylinder position.

## 4.2. TEST CONDITIONS

### 4.2.1 Static Load Tests

The static load experiments were conducted on chrome steel bearing balls with 2mm and 3mm diameters, and Delrin® acetal bearing balls with a 3mm diameter. Tests were conducted at various normal loads and shear rates. Selected tests were repeated with the dense packed procedure (described in part 4.1.7.2) conducted prior to the experiment. Tables 4.2, 4.3, 4.4 and 4.5 present testing conditions for experiments conducted on 2mm steel, 3mm steel, 3mm Delrin® acetal bearing balls, and sand with a grain size of 1-2mm, respectively. The “Normal Load” column presents the approximate normal force applied to the granular media before the shear force was applied.

Table 4.2. Static load tests conducted with 2mm chrome steel bearing balls. X represents test on loose packed material, P represents granular material that underwent the dense packing procedure prior to the experiment.

NORMAL LOAD [Lbs.]	SHEAR RATE [ $s^{-1}$ ]							
		0.003	0.006	0.009	0.012	0.015	0.018	0.021
30	X	X	X	X	X	X	X	X
270	X/P	X	X	X/P	X	X	X	X/P
420	X	X	X	X	X	X	X	X
500	X/P	X	X	X/P	X	X	X	X/P
720	X/P	X	X	X/P	X	X	X	X/P
960	X	X	X	X	X	X	X	X
1180	X	X	X	X	X	X	X	X
1410	X	X	X	X	X	X	X	X

Table 4.3. Static load tests conducted with 3mm chrome steel bearing balls. X represents test on loose packed material, P represents granular material that underwent the dense packing procedure prior to the experiment.

NORMAL LOAD [Lbs.]	SHEAR RATE [ $s^{-1}$ ]							
		0.003	0.006	0.009	0.012	0.015	0.018	0.021
30	X	X	X	X	X	X	X	X
120	X/P	X	X	X/P	X	X	X	X/P
270	X/P	X	X	X/P	X	X	X	X/P
420	X	X	X	X	X	X	X	X
500	X/P	X	X	X/P	X	X	X	X/P
720	X/P	X	X	X/P	X	X	X	X/P
960	X	X	X	X	X	X	X	X

Table 4.4. Static load tests conducted with 3mm Delrin® acetal bearing balls. X represents test on loose packed material, P represents granular material that underwent the dense packing procedure prior to the experiment.

NORMAL LOAD [Lbs.]	SHEAR RATE [ $s^{-1}$ ]							
		0.003	0.006	0.009	0.012	0.015	0.018	0.021
30	X	X	X	X	X	X	X	X
120	X/P	X	X	X/P	X	X	X	X/P
190	X	X	X	X	X	X	X	X
270	X/P	X	X	X/P	X	X	X	X/P

Table 4.5. Static load tests conducted with sand, with grain sizes of 1-2mm.

NORMAL LOAD [Lbs.]	SHEAR RATE [ $s^{-1}$ ]		
		0.003	0.021
40	X	X	
120	X	X	
190	X	X	
270	X	X	
420	X	X	
500	X	X	

#### 4.2.2 Oscillating Load Tests

The oscillating-load experiments were conducted at one maximum normal load of approximately 250 lbs, and one shear rate of  $0.003\ s^{-1}$ . Applying different air pressures and solenoid valve operating frequencies allowed varying normal load oscillation amplitude, and frequency. A change in normal load amplitude produces a change in the average normal load applied, since the maximum load is kept at a constant value. Tables 4.6 and 4.7 present testing conditions for experiments conducted on 2mm chrome steel bearing balls and sand, respectively. The experiments for steel bearing balls were conducted for both loose and dense random packed conditions for the tests performed with air pressure at 30 psi applied to the pneumatic vibration actuator. The air pressures of 25 and 30 psi result with the normal load applied to the granular media reduced by approximately 140 and 190 lbs, respectively.

Table 4.6 Oscillating normal load test conditions for 2mm chrome steel bearing balls. X represents test on loose packed material, P represents granular material that underwent the dense packing procedure prior to the experiment.

PRESSURE [psi]	FREQUENCY [Hz]									
		0.03	0.06	0.12	0.3	0.6	0.9	1.2	1.5	1.8
25	X	X	X	X	X	X	X	X	X	X
30	X/P	X/P	X/P	X/P	X/P	X/P	X/P	X/P	X/P	X/P

Table 4.7 Oscillating normal load test conditions for sand with a grain size of 1-2mm.

PRESSURE [psi]	FREQUENCY [Hz]					
	0.01	0.03	0.06	0.12	0.3	0.9
	25	X	X	X	X	X
30	X	X	X	X	X	X

### 4.3. EXPERIMENTAL DATA ANALYSIS PROCEDURE

#### 4.3.1. Force Measurement

Figure 4.15 presents an example of force measurement during a loose random packed static load test conducted on 2mm chrome steel bearing balls. The data presented in Figure 4.15 allows determining the average shear and normal forces. These average forces represent the mean measured value obtained during the time after the shear force has reached the steady-state value (indicated in the figure with the vertical dotted line). The error bars (marked with the dashed lines) represent a 95% confidence interval of the mean force measurements. Based on the average shear and normal forces the mean stresses may be calculated using Eq. 3.5. Mean shear stress is expected to be linearly dependent on mean normal stress, where the inverse tangent of the slope represents the internal friction angle of the granular medium [Rao, 2008].

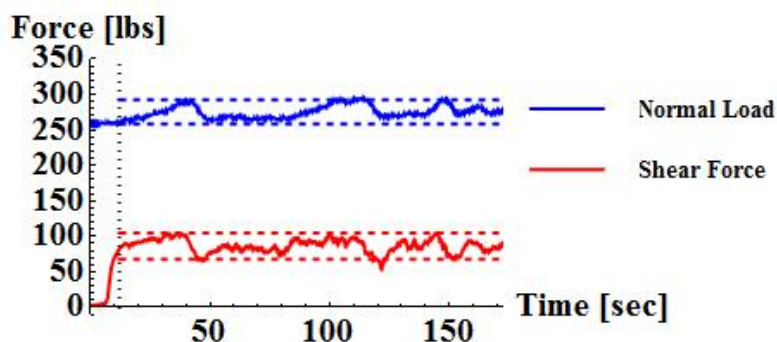


Figure 4.15. Shear and normal force sample data measurements for loose random packed 2 mm chrome steel bearing balls. Approximately 275 lbs normal force was applied to the granular media through the loading arm. Granular media was sheared at  $0.003 \text{ s}^{-1}$ .

### **4.3.2. Force Oscillation Analysis**

During the dense random packing experiments, shear force showed considerable oscillation around a mean value. Oscillating shear force data are presented in Figure 4.16a. In order to analyze the force oscillation characteristics, a Fast Fourier Transform (FFT) analysis was applied [Press, 2007, p.608]. An FFT numerical algorithm available in the Mathematica® software package was utilized for data analysis. This method determines the characteristic frequency of the oscillating shear force measurement. FFT applied to force as a function of time or distance returns force spectral density as a function of frequency or  $1/\lambda$  respectively, where  $\lambda$  represents the force oscillation wavelength. This analysis is conducted on the shear force after nearly steady-state flow was achieved. Hence, the initial transient effects are not considered in this analysis. Prior to applying the FFT, shear force is offset by the mean value in order to remove the characteristic frequency peak at 0 Hz corresponding to a nonzero mean value (Figure 4.16b). An array of zero's is added to the end of the force data, as presented in Figure 4.16c, to obtain a smoother FFT response. This approach is known as zero padding [Smith]. A sample FFT analysis on shear force is presented in Figure 4.16d. Characteristic frequencies were compared to the motor oscillation frequencies to ensure that the granular media is in fact physically causing force oscillations.

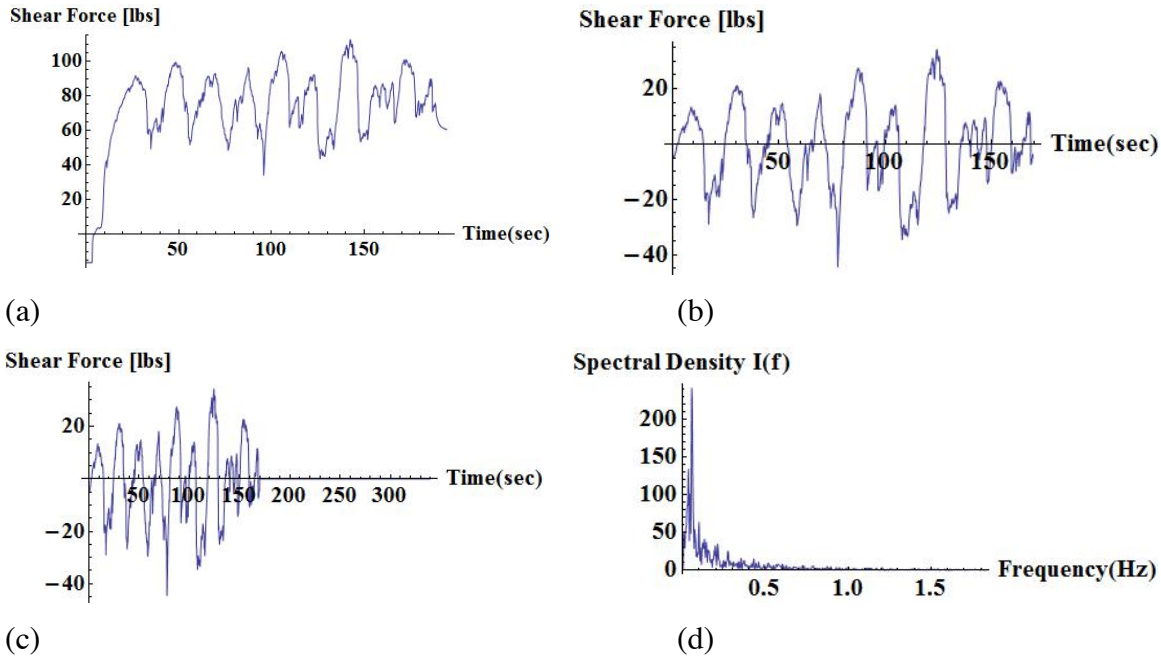


Figure 4.16. FFT Analysis: a) Shear force data acquired from the load cell, b) Steady state shear force offset by the mean force, c) Zero padding applied, d) FFT on shear force data from part (c).

#### 4.3.3. Shear rate and uncertainty analysis

An average shear cell speed is obtained from the slope of the displacement (measured by LVDT) vs. time plot. In order to apply smoothing to the speed measurement, larger data sets are analyzed for each slope calculation. Figure 4.17 shows an example of speed calculated from 2 and 24 displacement points. The speed uncertainty is subsequently estimated using Monte Carlo analysis. This method uses a random number generator function built into the Mathematica® software package. Random data sets are generated within time and displacement uncertainty boundaries. Displacement measurement uncertainty is defined by the instrument uncertainty. Timestamp uncertainty is defined by the period of time during which the displacement measurement is acquired. By analyzing multiple generated data sets, the measurement mean and standard deviation may be determined. Figure 4.18 shows a Monte Carlo simulation example for three randomly generated data sets, with 24 points generated for each data set.

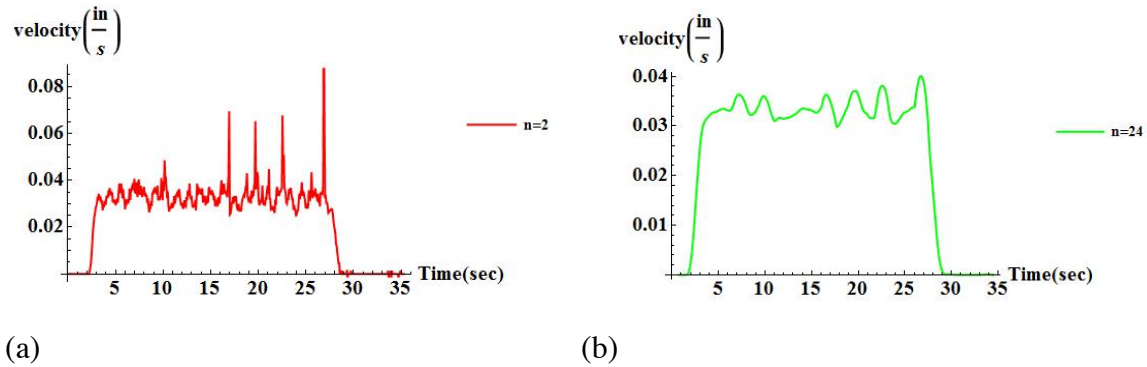


Figure 4.17. Shear speed measurement: a) Speed measured from slope of the fit to 2 displacement points, b) Speed measurement smoothed by measuring slope of 24 points.

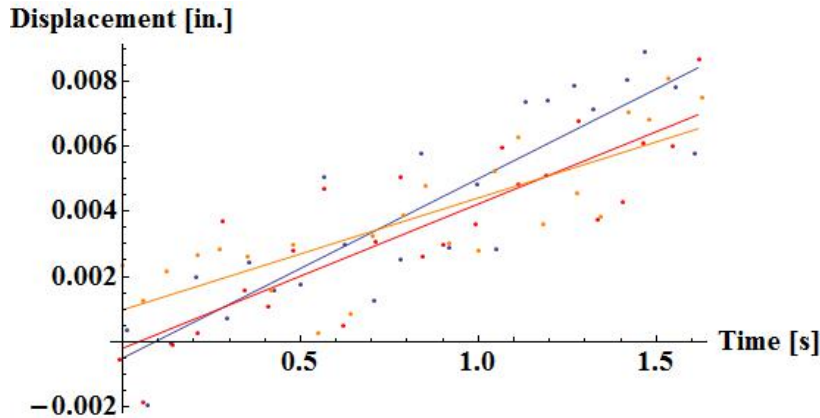


Figure 4.18. Monte Carlo Analysis on speed measurement uncertainty.

#### 4.3.4 Oscillating load experiments analysis

Normal load applied to granular media during the oscillating-load experiments may be modeled using the system presented in Figure 3.3. The static load experimental data were utilized when modeling the shear force behavior during the oscillating-normal load experiments. Steady-state shear force values may be evaluated from the previously calculated granular media internal friction angle. The shear force behavior during the transient time may also be predicted from the static load experiments. A model utilized in

plastic deformation of materials analysis was applied here, with the equation below describing the strain during transient creep [Roesler, 2007, p.384].

$$F_\tau = A(1 - e^{-\eta t}) \quad [4.2]$$

The exponent  $\eta$  may be evaluated by fitting the equation above to the shear force versus time plots under static load conditions. Figure 4.19 shows an example of the shear force fit applied during the data analysis. Utilizing the previously obtained steady state shear force and transient exponent, a complete shear force model was developed. Shear force predicted using this model is compared to the experimental data.

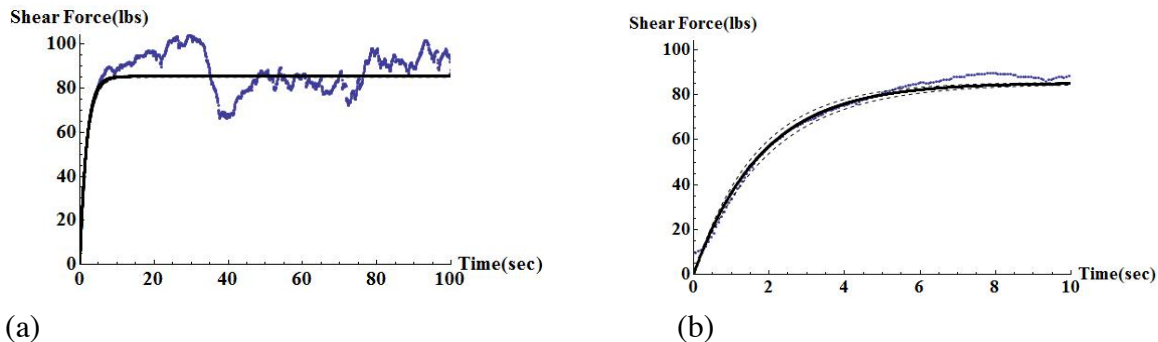


Figure 4.19. (a) Experimental shear force and fit. The experiment was conducted on chrome steel beads with 2mm diameter, an average normal load of approximately 275 lbs, and a shear rate of  $0.003 \text{ s}^{-1}$ . (b) Fit zoomed during the transient period.

## V. EXPERIMENTAL RESULTS AND DISCUSSION

### 5.1. STATIC NORMAL LOAD EXPERIMENTS

#### 5.1.1. Shear Stress versus Displacement

Shear stress versus displacement results obtained for various materials during this study are presented in Figure 5.1. All the tests illustrated in this figure were conducted under one load (30 lbs) applied to the lever. Figures 5.1 a and b present the tests conducted on chrome steel bearing balls with a 2 mm diameter under loose and dense-packed conditions, respectively. Dense-packed specimens generally demonstrate considerable oscillations in shear stress, and higher peak shear stress values than for loose packing. Similar differences are observed for 3 mm diameter bearing balls under loose (Figure 5.1c) and dense-packed (Figure 5.1d) conditions. Substantial oscillations in shear stress were observed for loose-packed Delrin® acetal bearing balls (Figure 5.1e). However, dense-packed acetal bearing ball experiments (Figure 5.1f) produced oscillations of greater amplitude and a trend similar to that discussed for chrome steel bearing balls. No substantial fluctuations in shear stress were observed for the experiments conducted on sand (Figure 5.1g). The steady-state shear stress for sand is approximately twice the steady-state shear stress for steel bearing balls.

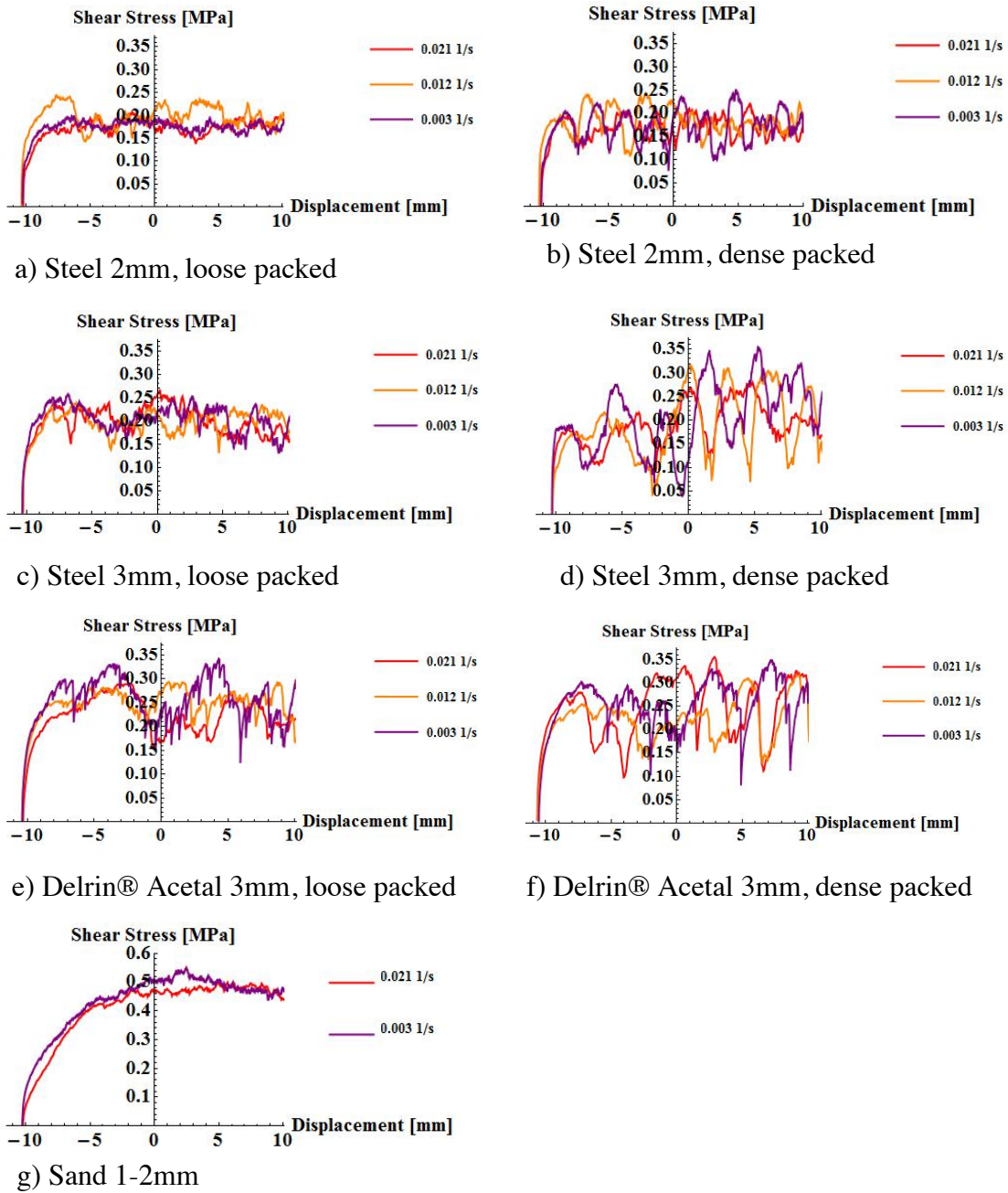


Figure 5.1. Shear stress versus displacement for static load direct shear experiments conducted under normal stress of approximately 0.6 MPa: (a) Chrome steel 2mm diameter balls, loose packed, (b) Chrome steel 2mm diameter balls, dense packed, (c) Chrome steel 3mm diameter balls, loose packed, (d) Chrome steel 3mm diameter balls, dense packed, (e) Delrin® Acetal 3mm diameter balls, loose packed, (f) Delrin® Acetal 3mm diameter balls, dense packed, (g) Sand 1-2mm diameter.

In order to validate the shear stress measurements, the results presented in literature are compared to the experimental data obtained in this study. Figure 5.2 shows experimental results from the literature for shear stress versus displacement for 1 mm diameter chrome steel bearing balls (Figure 5.2a) and sand of particles with diameters smaller than 2 mm (Figure 5.2b). These literature data were obtained from direct shear experiments. Chrome steel bearing ball shear stress behavior presented by O'Sullivan (Figure 5.2a [O'Sullivan 2005]) agrees with the shear stress trend for loose-packed steel presented in this study (Figures 5.1a, and c). Direct shear tests conducted on sand in this study (Figure 5.1g) agree with the trend for the loose-packed sand behavior presented by Feda [1982], as shown in Figure 5.2b. These results provide a general qualitative validation for the experimental instrument and data acquisition system.

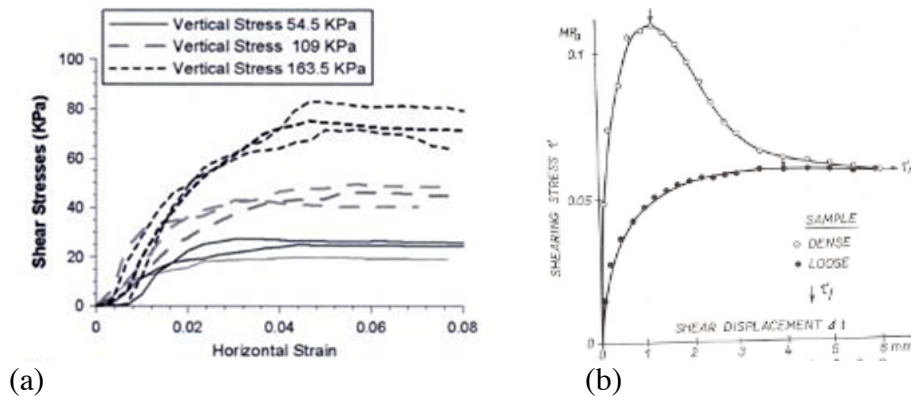


Figure 5.2. Literature experimental results from direct shear cell tests: (a) Shear stress versus horizontal strain for 1 mm steel bearing balls with void ratio ranging from 0.5841 to 0.6097 (Figure taken from O'Sullivan [2005]), (b) Shear stress versus displacement for dry Zbraslav sand (grain diameter less than 2mm), normal load of 0.1 MPa and shear speed of 0.1mm/min. Figure presents behavior for loose and dense sand packed sand (Figure taken from Feda [1982]).

### 5.1.2. Shear Stress versus Shear Rate

A graph of steady-state shear stress versus shear rate for 2mm diameter chrome steel bearing balls is presented in Figure 5.3. The tests analyzed in this figure were conducted under a constant normal load applied to the lever. Shear stress generally shows

no dependence on shear rate. This behavior confirms that the tests were conducted on granular media in the quasi-static flow regime, as discussed in section 2.3.1.

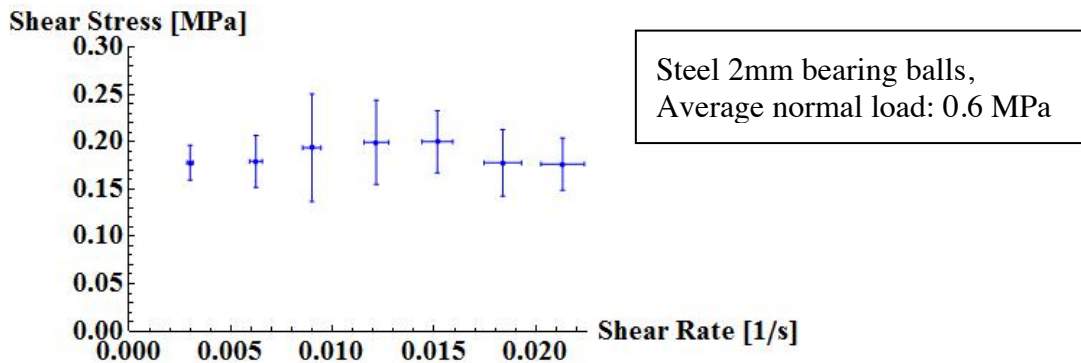


Figure 5.3. Shear stress versus shear rate for chrome steel 2mm diameter bearing balls. The experiments were conducted under a normal stress of approximately 0.6MPa. Vertical error bars represent a 95% confidence interval in shear stress measurement. Horizontal error bars represent a shear rate error introduced after speed smoothing was applied, as prescribed from the Monte Carlo analysis.

### 5.1.3. Internal Friction Angle

Shear stress is expected to depend linearly on normal stress applied during quasi-static flow of granular media. Figure 5.4 presents shear stress versus normal stress for chrome steel bearing balls with a 2 mm diameter under loose random packed conditions and sheared at the slowest shear rate applied in tests ( $0.003\text{ s}^{-1}$ ). The plot includes both average shear stress and maximum shear stress measurements, which were utilized in obtaining average and peak friction angles, respectively. Figure 5.5 presents shear stress versus normal stress for steel balls, acetal balls and sand under the same shear rate. A relation is observed between the material and the friction angle. Sand presents a higher friction angle than the spherical granular media, and acetal balls show a higher friction angle than steel balls. The internal friction angle is expected to exhibit granular material shape dependence, as presented by Das [2007]. Internal friction measurements are compiled in Tables 5.1 and 5.2.

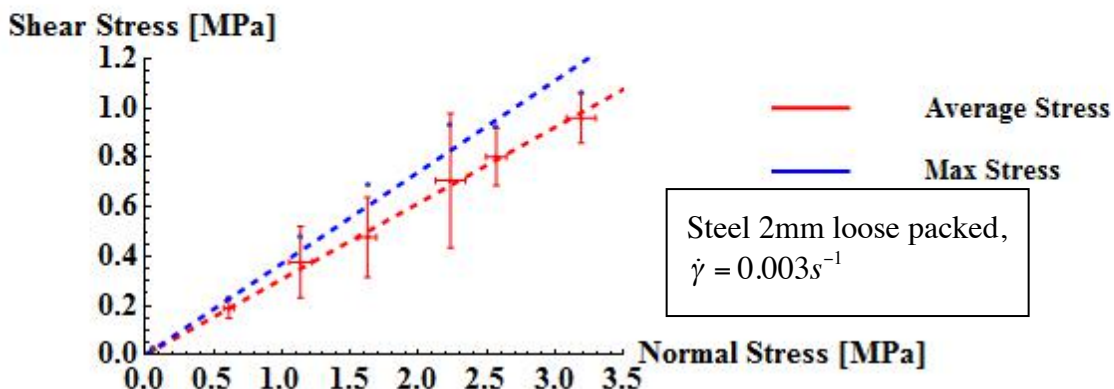


Figure 5.4. Shear stress versus normal stress for loose packed 2mm chrome steel bearing balls, sheared at  $0.003 \text{ s}^{-1}$ .

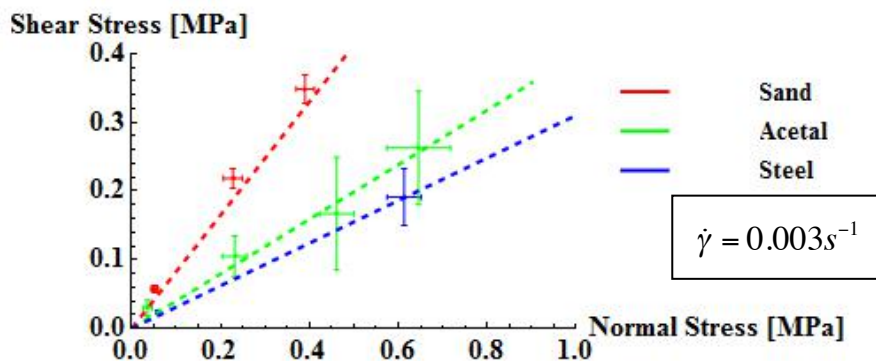


Figure 5.5. Steady-state shear stress versus applied normal stress for sand (1-2mm), loose random packed Delrin® acetal 3mm diameter bearing balls, and loose random packed chrome steel bearing balls with 2mm diameter. All materials were sheared at  $0.003 \text{ s}^{-1}$ .

Table 5.1. Average internal friction angle  $\varphi$ , measured in degrees. The “N/C” tests were not conducted. Error represents a mean error that accounts for 95% confidence intervals on angle measurements obtained for each tested shear rate.

GRANULAR MEDIA MATERIAL	SHEAR RATE [ $s^{-1}$ ]								
		0.003	0.006	0.009	0.012	0.015	0.018	0.021	Average
Steel 2mm loose	17.1	17.1	17.9	18.0	16.9	17.6	17.4	17.4	0.6
Steel 2mm dense	16.7	N/C	N/C	17.1	N/C	N/C	16.3	16.7	1.4
Steel 3mm loose	18.2	18.4	18.4	18.0	17.8	17.9	19.1	18.3	0.5
Steel 3mm dense	20.2	N/C	N/C	19.3	N/C	N/C	18.2	19.2	2.4
Acetal Loose	21.7	24.3	20.5	23.2	22.8	22.4	20.6	22.2	2.5
Acetal Dense	24.6	N/C	N/C	19.8	N/C	N/C	21.1	21.9	4.4
Sand 1-2mm	40.8	N/C	N/C	N/C	N/C	N/C	39.7	40.3	2.9

Table 5.2. Peak internal friction angle  $\varphi$ , measured in degrees. The “N/C” tests were not conducted. Error represents a mean error that accounts for 95% confidence intervals on angle measurement obtained for each tested shear rate.

GRANULAR MEDIA MATERIAL	SHEAR RATE [ $s^{-1}$ ]								
		0.003	0.006	0.009	0.012	0.015	0.018	0.021	Average
Steel 2mm loose	20.3	19.8	21.0	21.0	19.8	20.8	19.9	20.4	1.2
Steel 2mm dense	22.8	N/C	N/C	23.3	N/C	N/C	22.1	22.7	4.2
Steel 3mm loose	23.0	24.1	21.8	21.5	22.0	22.4	23.8	22.7	0.9
Steel 3mm dense	31.0	N/C	N/C	27.3	N/C	N/C	25.7	28.0	4.7
Acetal Loose	27.4	29.4	26.1	27.9	28.0	28.0	26.4	27.6	4.2
Acetal Dense	31.6	N/C	N/C	27.2	N/C	N/C	28.6	29.1	8.6
Sand 1-2mm	42.9	N/C	N/C	N/C	N/C	N/C	41.0	42.0	3.6

Literature results for experimentally measured internal friction angle are presented in Figure 5.6. Peak shear stress versus normal stress for 1 mm diameter steel bearing balls is presented in Figure 5.6a [O’Sullivan, 2005]. Data presented in Figure 5.6a were obtained from the experiments presented in Figure 5.2a. The internal friction angle for 2 mm loose random packed chrome steel bearing balls obtained in this study was measured for 7 different rates and 7 different applied normal loads, with a total of 49

experiments, compared to the 9 experiments analyzed by O’Sullivan in Figure 5.6a. An average peak internal friction angle of  $24.4^\circ$  was reported by O’Sullivan, which is in good agreement with the maximum internal friction angle measured in this study of  $22.7^\circ \pm 4.2^\circ$  for 2 mm dense-packed steel bearing balls. The experiments on loose 2 mm steel bearing balls returned a friction angle of  $20.4^\circ \pm 1.2^\circ$ , which is smaller than the friction angle observed by O’Sullivan. One possible explanation for the lower internal friction angle measured in this project is that an error analysis was not presented in O’Sullivan’s study [O’Sullivan, 2005]. Hence, the two data sets are generally difficult to compare directly. The internal friction angle for sand presented in literature and experimental results obtained in this study agree well. The average experimental internal friction angle in this study is  $40.3^\circ \pm 2.9^\circ$ , compared to  $37.4^\circ$  obtained experimentally by Das [2007]. The study presented by Das also does not provide an error for the experimentally measured friction angle, and from Figure 5.6b a considerable experimental variation is observed. Another possible explanation for the discrepancy in the results could be associated with the fact that the studies were conducted on different sand materials.

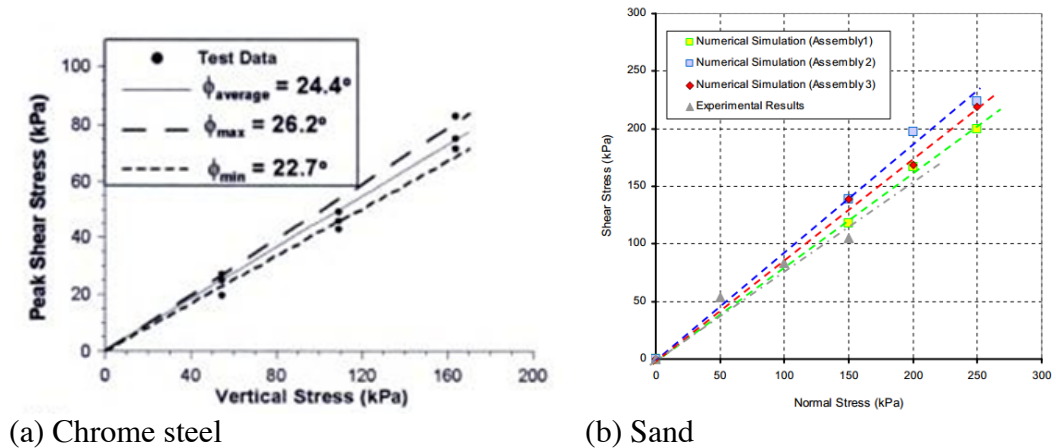


Figure 5.6. Friction angle, literature results: (a) Peak shear stress versus normal stress for 1mm diameter chrome steel bearing balls [Figure taken from O’Sullivan], (b) Shear stress versus normal stress for Daytona Beach sand. Experimental data was measured at  $37.4^\circ$ , and simulated at  $39.1^\circ$  to  $42.9^\circ$ . Corresponding rounded particle had a measured internal friction angle of  $24.4^\circ$  to  $27^\circ$  (Figure taken from Das [2007]).

A discrepancy in the internal friction angle measurement, compared to the literature results, could also be potentially caused by scaling effects. According to the ASTM D3080/D3080M direct shear test standard, the shear cell cavity width should be 2 in. or 10 times the maximum particle size diameter (whichever is larger), the thickness should be 0.5 in. but not less than 6 times the maximum particle diameter, and the width to thickness ratio should be 2:1. For the experiments conducted in this project, the shear cell cavity had a width of 20mm and thickness of approximately 40mm. Hence, for 2 mm balls the width of the box is 10 diameters and the thickness is 20 diameters. For 3mm diameter balls, the width and thickness are approximately 7 and 13 diameters, respectively. The standard width to thickness and minimum width criterions are not satisfied for the shear cell geometry utilized in this study for the 3-mm balls. The width of the shear cell was driven by the design requirement of high normal load application. Increasing the width decreases the maximum normal stress. Another reason for selecting a smaller width was motivated by the volume of the granular media used in each experiment, which is approximately the volume required to perform biaxial light alloy warm forming experiments. According to Cerato [2006], as long as the width of the specimen is less than 50 particle diameters a scale effect may be observed and the friction angle can be over-predicted for boxes of smaller widths. This most likely explains why the 3 mm diameter steel balls show a higher internal friction angle than the 2 mm balls. Cerato [2006] observed that friction angles for loose specimens were more affected by cell size scaling than for dense specimens. This result is reproduced in this study, by the data in Tables 5.1 and 5.2.

#### **5.1.4. Decay Exponents for Static Normal Load Experiments.**

Figure 5.7 presents the fit of an exponential decay equation (Eq. 4.2) to shear stress versus time data. The resulting description is used to characterize the behavior of granular media before the steady-state shear stress was reached. Figure 5.7a shows a fit equation applied to 2-mm steel balls under loose packed conditions, and Figure 5.7b shows a fit equation applied to sand. Although this approach provides a good estimate of

shear stress during the transient period, it oversimplifies the experimental results, as is shown by comparing the fits and experimental data in Figure 5.7.

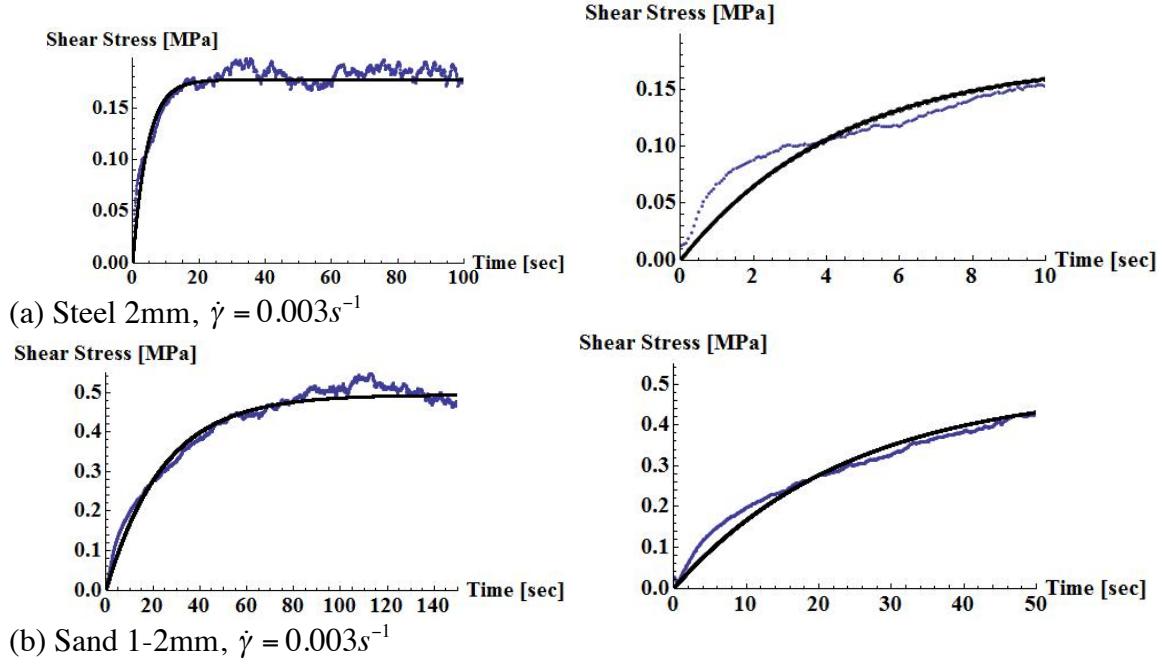


Figure 5.7. Exponential decay fits to shear stress versus displacement plots for the experiments under static loads. Blue curves represent the experimental data for the tests with the following conditions: (a) Steel 2mm loose packed sheared at  $0.003\text{ s}^{-1}$  with normal load of approximately 0.6MPa, (b) Sand 2mm sheared at  $0.003\text{ s}^{-1}$  with normal load of approximately 0.55MPa. Plots on the right present the experimental data during the transient period.

Decay exponent ( $\eta$ ) measurements were obtained for all the tested materials. The results were compiled in Figure 5.8 by plotting decay exponents versus the corresponding average normal loads. The data presented in this figure was obtained from the tests conducted at a constant shear rate of  $0.003\text{ s}^{-1}$ . On average, dense 2 mm diameter steel balls present the largest decay exponent. Generally,  $\eta$  parameters measured for higher normal loads show a slightly decreasing trend. However, a relatively large data scatter does not allow a more detailed determination of trends. It is clear from this figure that decay exponents are considerably smaller for sand than for other materials examined in

this study. The smallest average  $\eta$  parameter signifies that sand has the longest transition period before a steady-state shear stress develops within the granular media sample.

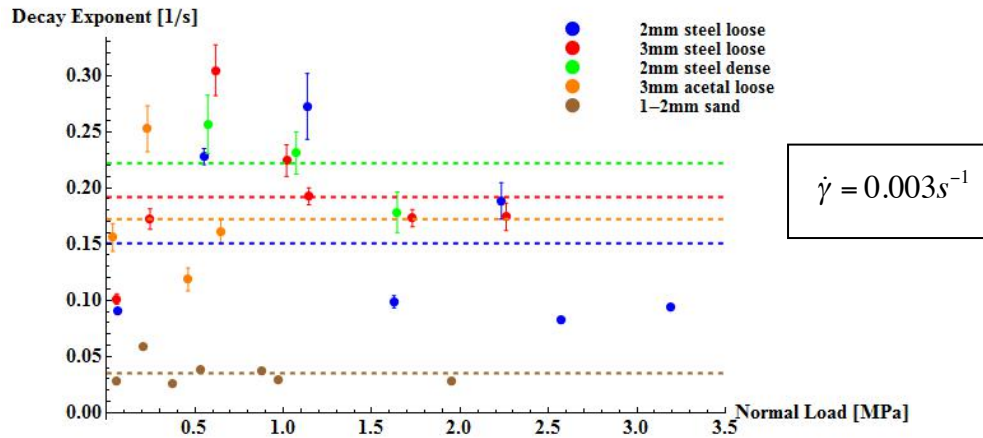


Figure 5.8. Decay exponents for static load tests conducted at a shear rate of  $0.003 \text{ s}^{-1}$ . The exponents were obtained from fitting the exponential decay equation (Eq. 4.2) to shear stress versus time plots.

Decay exponent analysis was also performed on shear stress versus displacement plots, which allow comparing  $\eta$  parameters for experiments undergoing different shear rates. Figure 5.9 presents the exponential decay measurements for static load experiments conducted on 2mm diameter chrome steel bearing balls. The data presents a considerable amount of scatter about relatively close average values for each shear rate. Generally, this indicates that the rate of shearing does not have a significant influence on the shear stress transition distance. Decay exponents appear to decrease for sufficiently high normal loads. However, no strong exponential decay dependencies may be deduced from this figure due to the strong data scatter.

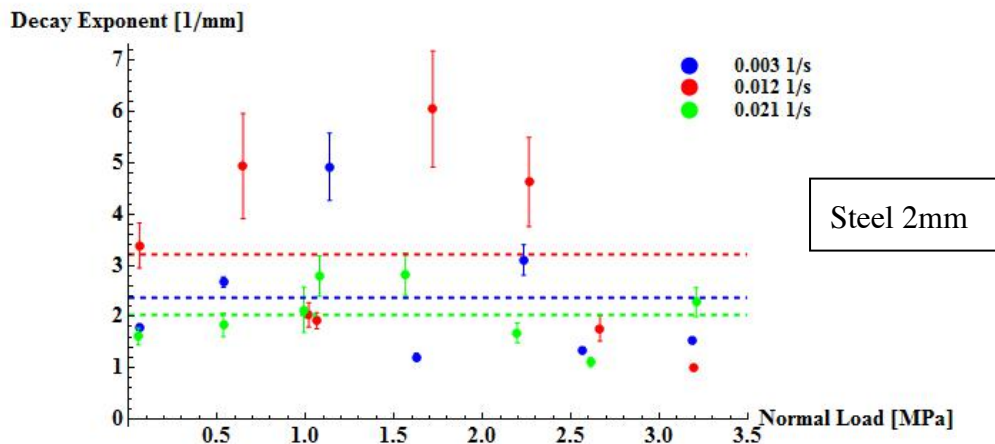


Figure 5.9. Decay exponents for static load tests conducted on chrome steel balls of 2mm diameter. The exponents were obtained from fitting the exponential decay equation to shear stress versus displacement plots.

A decay exponent measurement repeatability study was conducted for experiments at two different test conditions, as presented in Table 5.3. An early onset of shear stress fluctuations appears to affect the exponential fit for the first set of experiments. Because of this, these data points are considered as outliers. Experimental sets 2, 3, and 4 show only small discrepancies, with the fast shear rate experiment revealing considerably more consistent measurements. The experimental variability presented in Table 5.3 provides a reason behind the data scatter in decay exponents observed in Figures 5.8 and 5.9. Perhaps, more experiments would allow generating a better statistical data sample, which could reveal a stronger data trend for decay exponent variation during static load experiments.

Table 5.3. Measurement repeatability study on decay exponents obtained from the fit of shear stress versus time for steel balls with 2mm diameter under normal load of approximately 0.55MPa. Error represents a 95% confidence interval for each of the  $\eta$  parameters.

Test no.	Shear Rate [s <sup>-1</sup> ]			
	0.003		0.021	
	$\eta$ [s <sup>-1</sup> ]	Error	$\eta$ [s <sup>-1</sup> ]	Error
1	0.554	0.050	3.559	0.963
2	0.130	0.005	0.825	0.122
3	0.116	0.003	0.802	0.103
4	0.228	0.007	0.945	0.094

### 5.1.5. Shear Stress Oscillation FFT Analysis

As observed in section 5.1.1, direct shear experiments on bearing balls revealed a considerable shear stress fluctuation. The oscillation was mostly apparent during the tests conducted on dense random packed samples. Figure 5.10 shows shear stress FFT analysis results, with a dashed vertical line representing the inverse diameter of the granular medium tested. Figures 5.10a, b, and c present FFT results for 2mm steel bearing balls under dense packing conditions sheared at 0.003, 0.012, and 0.021 s<sup>-1</sup>, respectively. These tests correspond to the shear stress measurements presented in Figure 5.1b. Figures 5.10d,e, and f present experiments under the corresponding conditions conducted on 3mm dense-packed chrome steel bearing balls. A strong relation between the FFT peaks and the ball diameter shows that the granular medium material physically causes the shear stress fluctuations. The FFT peaks for tests conducted at the fastest rate of 0.021 s<sup>-1</sup> do not correspond exactly to the inverse granular media size, which could be caused by the fact that the fastest rate experiments have the smallest data sample size, which decreases the accuracy of the FFT analysis. The FFT analysis is also affected by the small number of force fluctuation cycles during each experiment, with approximately 9 and 6 total cycles for 2mm and 3mm diameter spheres, respectively. The number of total shear

stress oscillation cycles is constrained by the geometry (length) of the shear cell. The shear stress oscillation is most likely caused by the jamming from the force chain geometries formed within the granular media structure.

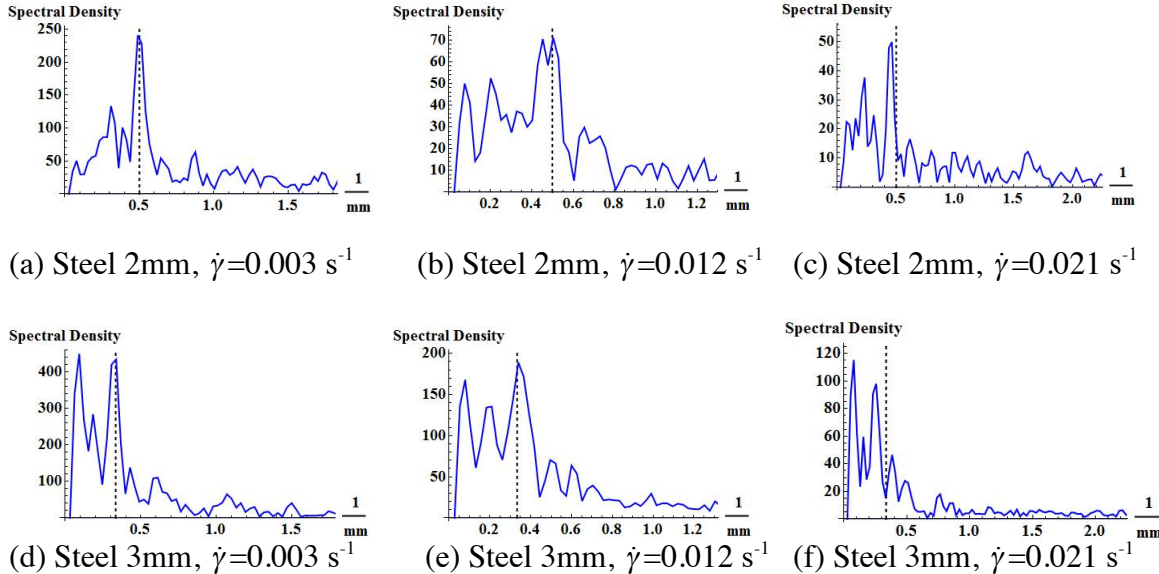


Figure 5.10. Shear stress FFT analysis on dense packed chrome steel balls under an approximate normal load of 0.6MPa: (a) 2mm diameter, shear rate of  $0.003\text{ s}^{-1}$  (b) 2mm diameter, shear rate of  $0.012\text{ s}^{-1}$  (c) 2mm diameter, shear rate of  $0.021\text{ s}^{-1}$  (d) 3mm diameter, shear rate of  $0.003\text{ s}^{-1}$  (e) 3mm diameter, shear rate of  $0.012\text{ s}^{-1}$  (f) 3mm diameter, shear rate of  $0.021\text{ s}^{-1}$ . The dashed vertical line on each plot represents the grain bead inverse diameter.

Miller [1997] observed a similar effect of force fluctuations during granular media flow experiments. The experimental geometry utilized in Miller's study [presented in Figure 5.11a] consisted of an annular shear cell, with a transducer measuring a change in local normal stress in granular media, which was undergoing continuous shear. Figure 5.11b presents the resultant force fluctuations. The author observed that the wavelength of the stress oscillation is on the order of magnitude of the tested grain diameter.

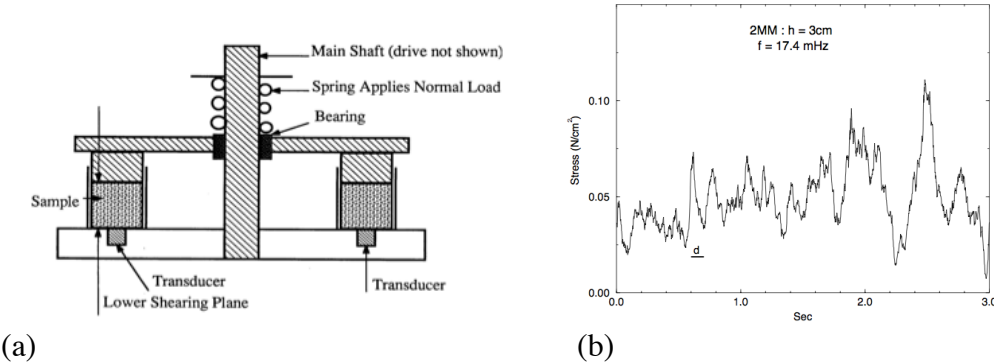


Figure 5.11. (a) Annular shear cell experimental set-up (Figure taken from Miller [1997]), (b) Transducer stress measurement versus time; horizontal mark “d” represents the time corresponding to the top lid travelling a distance of one bead diameter (Figure taken from Miller [1997]).

## 5.2. OSCILLATING NORMAL LOAD EXPERIMENTS.

### 5.2.1. Normal Load Oscillation

During the oscillating load experiments a square wave electrical input into the air valve actuation mechanism produced additional normal load sinusoidal oscillations that decay after load changes. These decaying oscillations were caused by the instrument vibration. Figure 5.12 presents a comparison between the experimental data and the normal force response simulated using the physical system model presented in Figure 3.4. The mass-spring-damper model overpredicts the normal force oscillation frequency by approximately a factor of 2. However, this model represents a highly simplified system and does not account for such effects as compliance due to the instrument frame elements and granular medium. A more detailed system model could be developed, but is beyond the scope of this project. The purpose of this particular model was to determine the main source of the observed load oscillation. These were sufficiently well captured with the simplified harmonic oscillator model. This result supports the explanation of instrument vibration causing the decaying load oscillations observed immediately after load changes.

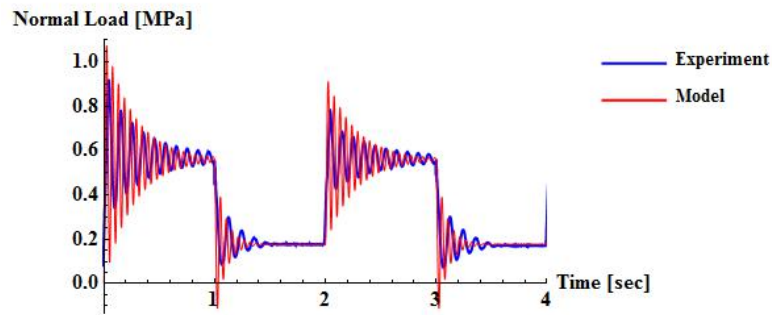


Figure 5.12. Predicted and measured normal load applied to granular media during the oscillating normal load experiment. Initial load applied to the lever equals approximately 0.55 MPa. The data were obtained from a test conducted with air under 30 psi pressure applied to the pneumatic cylinder at the frequency of 2 Hz.

### **5.2.2. Shear Stress under Oscillating Normal Load.**

Figure 5.13 below presents shear and normal stress measurements during a low frequency oscillating normal load experiment. Figure 5.13b presents shear and normal stress experimental measurements, as well as the expected steady-state shear stress computed from the granular media friction angle analysis. When the high normal load is applied, shear stress reaches the steady-state value after a relatively short transient period. Figure 5.13d presents an example of an exponential decay fit to the shear stress experimental data during one half-cycle after the high normal load was applied. This fit procedure is used to determine the exponential decay parameter for granular media during the oscillating load experiments.

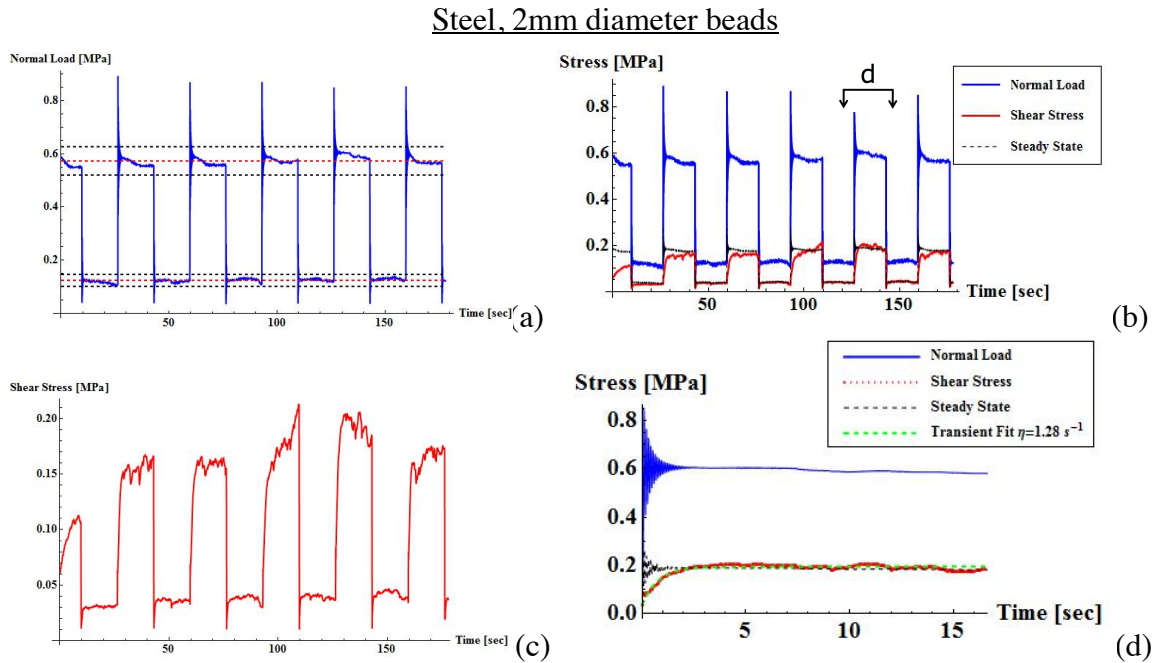


Figure 5.13. Chrome steel 2mm bearing balls sheared at a steady-state rate of  $0.003\text{s}^{-1}$  under oscillating load at  $f=0.03\text{Hz}$ , (a) Normal load oscillation, dashed lines indicate average normal stress during low and high load application, and a corresponding 95% confidence interval, (b) Shear stress, normal stress, and expected steady-state shear stress, (c) Shear stress oscillation (d) Exponential decay fit applied to the shear stress for  $\frac{1}{2}$  of the load cycle at  $t_0 = 126.2\text{s}$ .

Shear and normal stress measurements during a high frequency normal load oscillation experiment are illustrated in Figure 5.14. The maximum shear stress during high frequency oscillation experiment (Figure 5.14c) is smaller than the maximum shear stress under low frequency normal load oscillation (Figure 5.13c). This occurs because the normal load fluctuation is forced fast enough that the shear stress does not reach the steady state. During high frequency normal load oscillation, the shear stress exhibits a saw-tooth pattern (presented in Figure 5.14b), similar to the experimental results presented by Albert [2000] in an experiment measuring the force on a rod injected into a moving granular layer (Figure 2.14b). An additional experiment was conducted, during which the shear force was acquired at a rate of 100 Hz (Figure 5.14d). This experiment was performed in order to examine the transient shear stress behavior more closely, while

the normal load exhibits harmonic oscillations discussed in section 5.2.1. A small shear stress oscillation was observed initially, when the high normal load was applied, yet the shear stress vibration amplitudes were considerably smaller than the vibration amplitudes predicted from the simple exponential decay model (Eq. 4.2). Figure 5.14e presents a comparison between the shear stress exponential decay model (labeled ‘Transient  $\eta=1.1$  s $^{-1}$ ’) and experimental data. The model presented uses an average exponential decay constant obtained from shear stress fits of experiments conducted under a lower normal load oscillation frequency, as presented in Figure 5.13d. Although the predicted shear stress in Figure 5.14e exhibits excessive oscillations, it generally shows a good match with the trends of the experimental data. This observation shows that the decay exponent remains relatively constant at high normal load oscillation frequencies.

### Steel, 2mm diameter beads

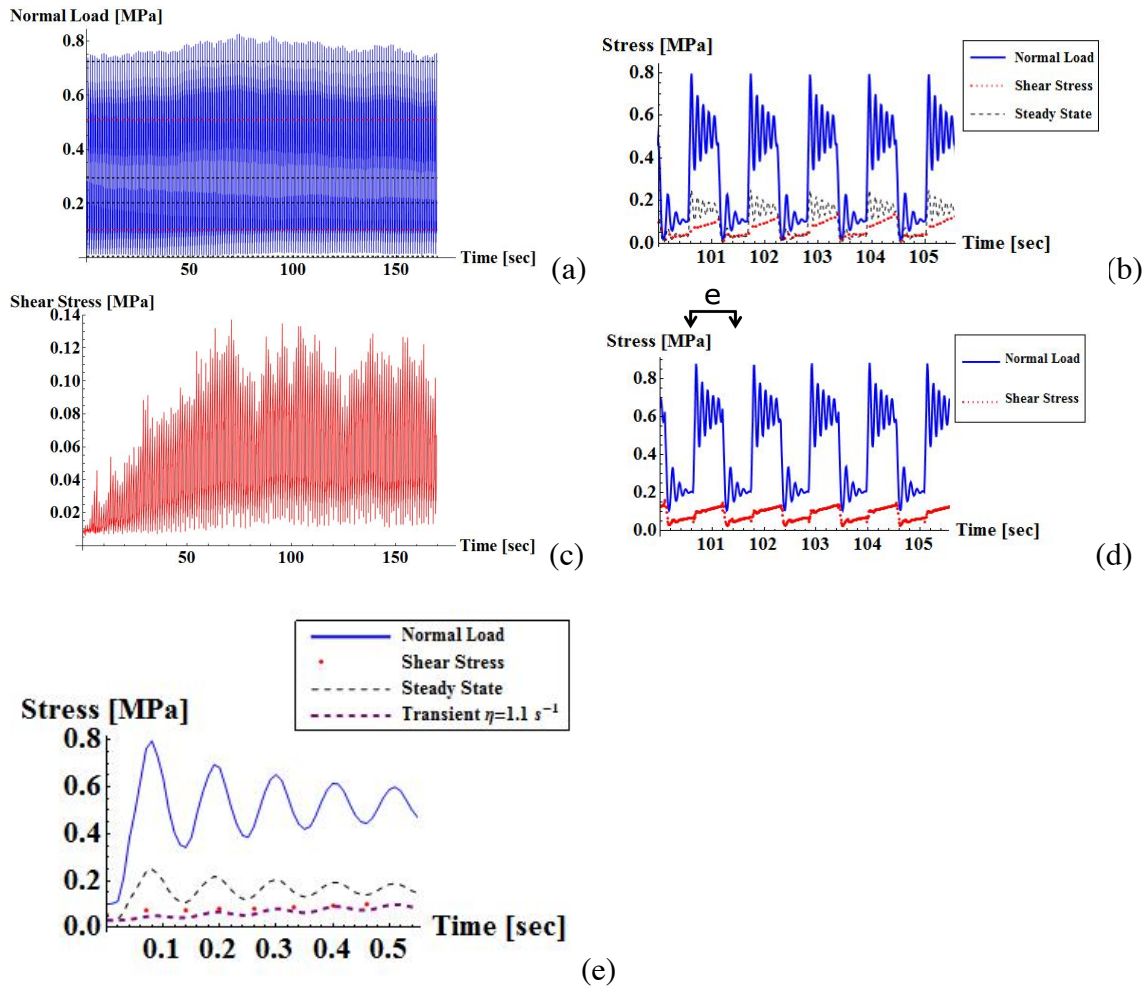


Figure 5.14. Chrome steel 2mm bearing balls sheared under oscillating load at  $f = 0.9\text{Hz}$ , (a) Normal load oscillation, (b) Shear stress and normal load during 5 periods of normal load oscillation, (c) Shear stress oscillation, (d) Shear stress and normal load during 5 periods of normal force oscillation, with shear stress acquired at  $100\text{ Hz}$ , (e) Shear stress exponential decay model (labeled ‘Transient  $\eta = 1.1 \text{ s}^{-1}$ ’) compared to experimental data, after the high normal load was applied for  $\frac{1}{2}$  load cycle at  $t_0 = 100.5\text{s}$ .

Oscillating load experiments on dense packed chrome steel bearing balls may also produce considerable shear stress fluctuations, as previously described in the static load experiments discussion. Figure 5.15a presents a shear stress versus time plot for granular media sheared at similar conditions to the experiment presented in Figure 5.14c. A major difference between the two experiments is the dense packing procedure conducted prior

to the test presented in Figure 5.15a. Low frequency shear stress FFT analysis presented in Figure 5.15b reveals a peak frequency that actually corresponds closely to the inverse of the time required for the shear cell to travel a distance of 1 bead diameter. Hence, normal load oscillation apparently does not remove the effect of granular media jamming force chains, discussed for the static load FFT results in section 5.1.5.

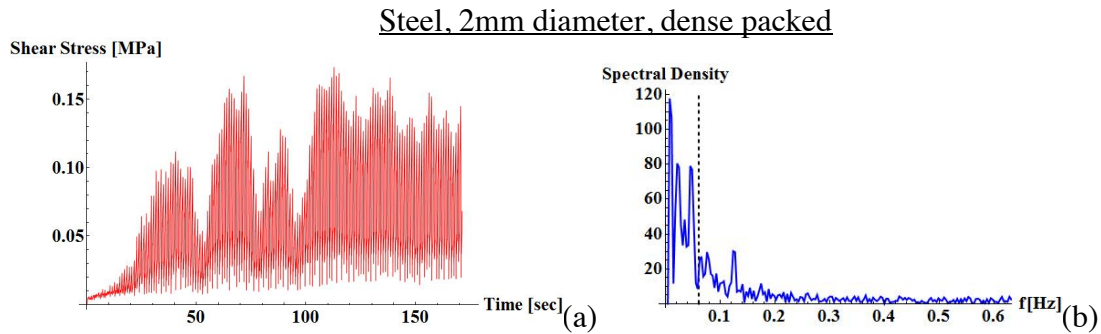


Figure 5.15. Steel 2mm diameter dense packed bearing balls, sheared at  $0.003\text{ s}^{-1}$  under an oscillating load; normal load is oscillating at 0.9Hz between 0.12MPa and 0.55MPa (a) Shear stress versus time, (b) Shear stress FFT analysis on the data presented in part A, the dashed line represents an inverse of the time required for the shear cell to travel 1 ball diameter.

Oscillating normal load experimental results for sand under low and high frequency normal load oscillations are presented in Figures 5.16 and 5.17, respectively. It can be observed from Figure 5.16b, that once the low normal load is applied (load applied between 100-150s), sand exhibits dense granular medium characteristics. The shear stress decreases towards the steady-state value after an initial ‘overshoot’, as previously presented from the literature in Figure 5.2b. This dense packed behavior explains why the shear stress is actually higher than the steady-state value expected for the corresponding low normal load applied during the high frequency oscillation experiment presented in Figure 5.17b. As previously observed for steel bearing ball experiments, high frequency normal load oscillation causes a decrease in maximum shear stress reached during the experiment. This effect can be visualized by comparing Figures 5.16c (maximum shear is approximately 0.52 MPa) and 5.17c (maximum shear is approximately 0.37 MPa). Figure 5.8 showed that the decay exponent for sand is lower than the decay exponent for steel

balls measured during static load experiments. Hence, the shear stress transient period is longer for sand. As a result a lower normal load oscillation frequency is required for sand to prevent the shear stress from reaching the steady-state value. An exponential decay fit to the shear stress experimental data, during one half-cycle (when high normal load is applied) low frequency oscillation experiment, returns a decay exponent of  $0.074 \text{ s}^{-1}$ , as presented in Figure 5.16d. The oscillating load decay exponent is greater than the average decay parameter obtained for static load experiments, measured at approximately  $0.035 \text{ s}^{-1}$ . It should be noted that the exponential decay fit applied to the shear stress experimental data during the high frequency normal load oscillation (Figure 5.17d) returns a much greater  $\eta$  parameter, reported at approximately  $1 \text{ s}^{-1}$ , which is relatively close to the corresponding average for chrome steel balls, measured at  $1.1 \text{ s}^{-1}$ .

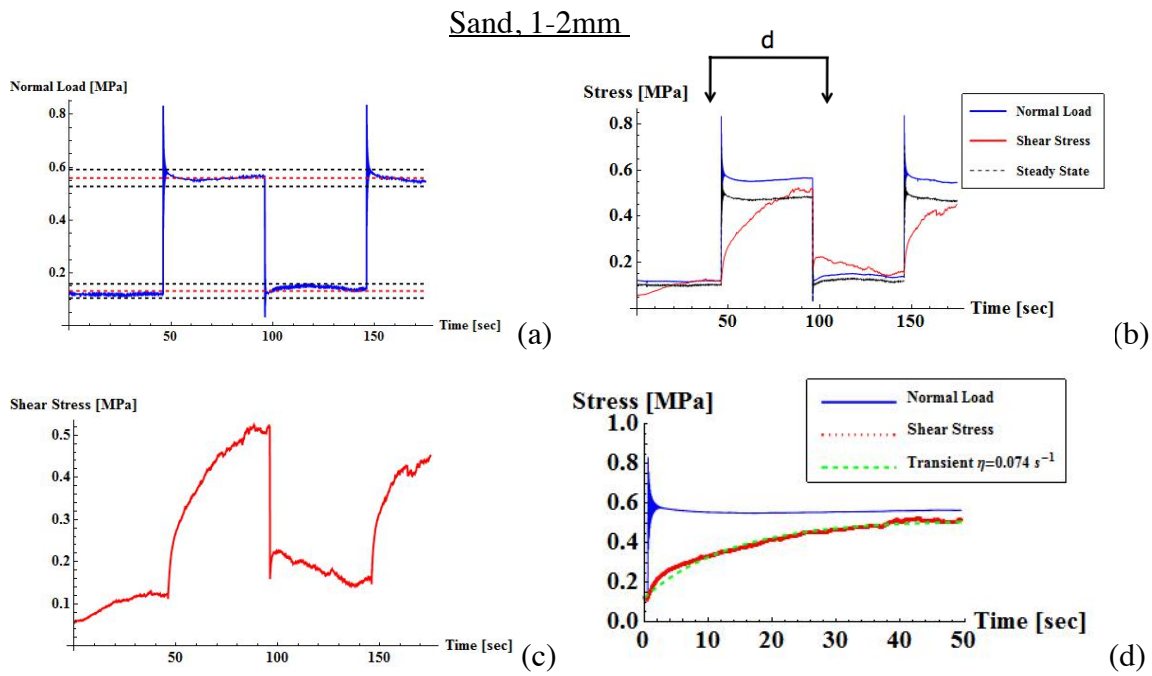


Figure 5.16. Sand sheared under oscillating load at  $f = 0.01\text{Hz}$ , (a) Normal load oscillation, dashed lines indicate average normal stress during low and high load application periods, and a corresponding 95% confidence interval, (b) Normal load, shear stress and expected steady-state shear stress, (c) Shear stress (d) Exponential decay fit applied to the shear stress after the high normal load was applied for  $\frac{1}{2}$  cycle at  $t_0 = 45.5\text{s}$ .

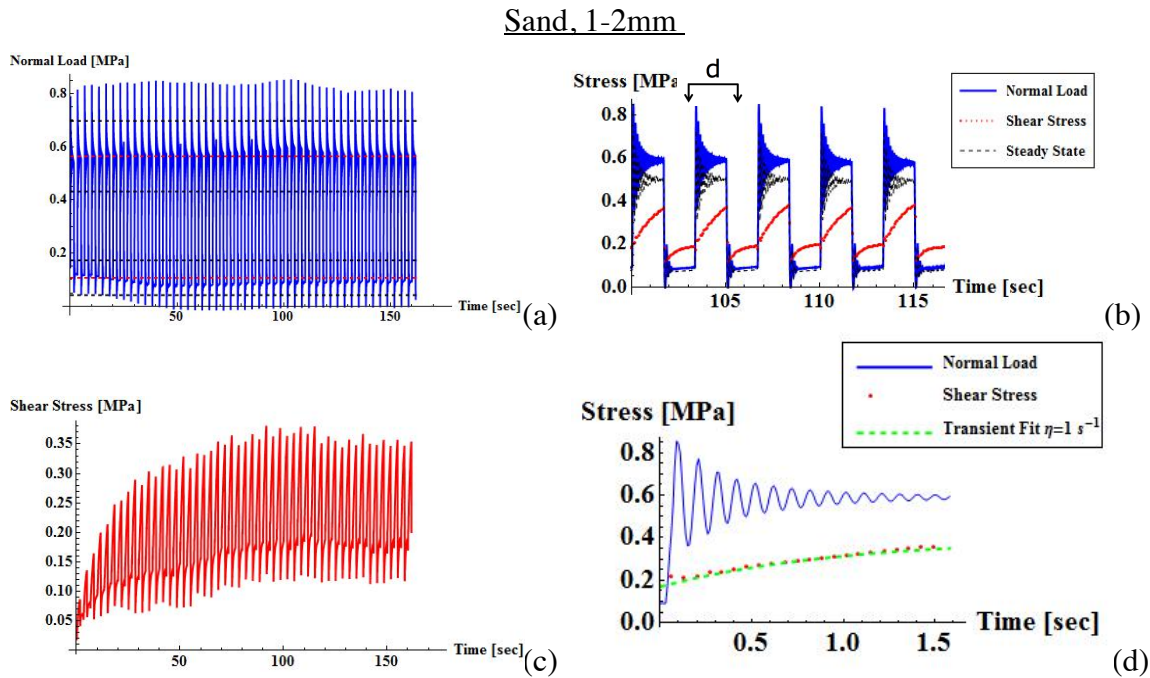


Figure 5.17. Sand sheared under oscillating load at  $f = 0.3\text{Hz}$ , (a) Normal load oscillation, (b) Normal load and shear stress during 5 periods of normal force oscillation, (c) Shear stress, (d) Exponential decay fit applied to shear stress when the high normal load is applied for  $\frac{1}{2}$  cycle at  $t_0 = 103.32\text{s}$

### 5.2.3. Oscillating Load Decay Exponents

The dynamic decay exponent measurements for chrome steel balls are compiled in Figure 5.18. Figures 5.18a, b, c, and d present decay exponents from fits to the shear stress data, during the half-cycle when the maximum normal load is applied, for experiments conducted at 0.03, 0.06, 0.12, and 0.3Hz, respectively. The decay exponents in each figure are plotted versus the normal load cycle number. The oscillating load experiments were conducted for two different pressures applied to the air cylinder, which resulted in two different low load levels. The experiments with higher normal load oscillation frequencies are not included in this analysis because the shear stress did not reach a steady-state value during those experiments. Decay exponents measured during the oscillating load experiments are on average  $1$  to  $2 \text{ s}^{-1}$ . These  $\eta$  values are considerably higher than the decay exponents measured for static load tests with 2mm

steel balls, sheared at the same rate, which were measured to be 0.1 to 0.25 s<sup>-1</sup> (as presented in Figure 5.8). During these experiments, the average decay exponent is greater for the tests conducted at lower load amplitude (caused by the lower air pressure in the piston). The lower load amplitude experiments resulted in a higher average normal load.

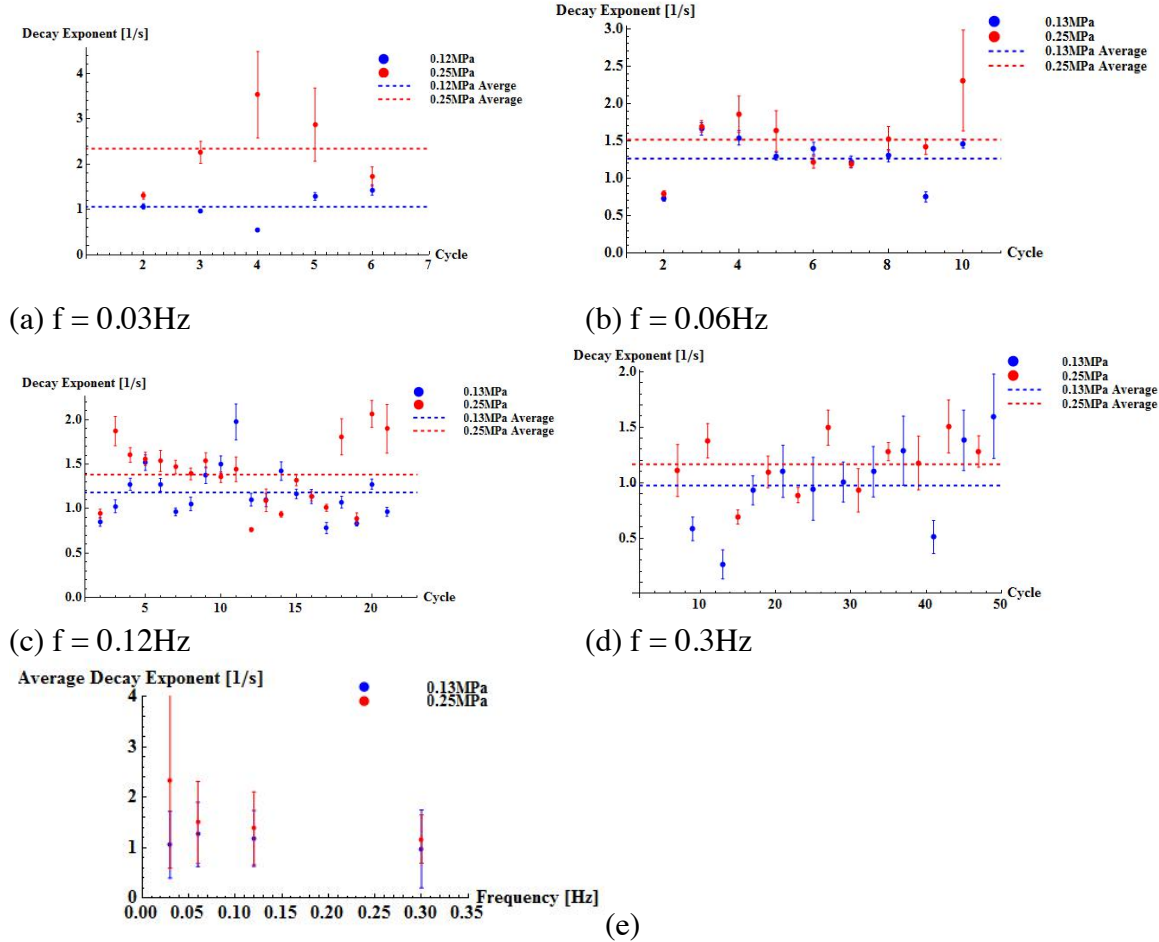


Figure 5.18. Decay exponents obtained from fits to experimentally measured shear stress when the high normal load is applied. The experiments were conducted on 2mm chrome steel bearing balls with initial normal load of 0.55MPa, air cylinder pressure of 30 psi (low load of 0.13MPa) and 25psi (low load of 0.25MPa), and the following load oscillation frequencies: (a)  $f = 0.03\text{ Hz}$ , (b)  $f = 0.06\text{ Hz}$ , (c)  $f = 0.12\text{ Hz}$ , (d)  $f = 0.3\text{ Hz}$ , (e) Average decay exponents for each of the 4 analyzed load oscillation frequencies are plotted versus frequency.

### 5.2.4. Shear Stress versus Displacement

Figure 5.19 presents an example of results from load-unload experiments conducted on granular media, as demonstrated in literature. Figure 5.19a illustrates a shear stress versus displacement result for a direct shear cell test conducted on sand under a constant normal load with a shear stress continuously varied between 0 and  $\tau$  [Feda, 1982]. Figure 5.19c presents triaxial experiment (introduced in section 2.4.1.2) load-unload results conducted on steel beads, with the test specimen presented in Figure 5.19b [O'Sullivan, 2009]. A hysteresis in shear stress occurs when the load-unload cycle takes place.

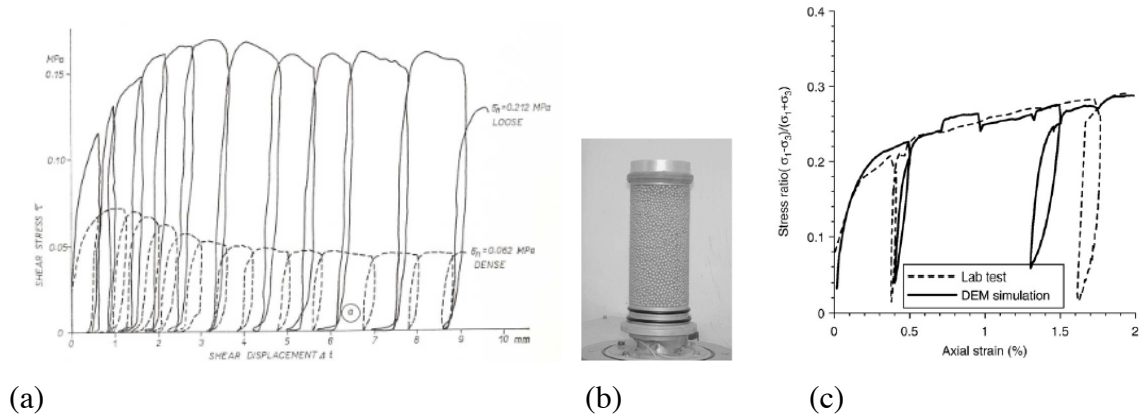


Figure 5.19. Literature results of load reversed experiments (a) Shear stress versus shear displacement for direct shear tests conducted on Zbraslav sand (Figure taken Feda [1982]), (b) Specimen consisting of steel beads used in triaxial load-unload experiment (Figure taken from O'Sullivan [2005]), (c) Stress-strain results for the triaxial experiment on the specimen presented in Figure 5.19b (Taken from O'Sullivan [2009]).

Experimental data obtained in this study, and presented in Figure 5.20 show a behavior similar to that presented in literature. This figure presents five normal load oscillations during experiments conducted on 2 mm diameter steel balls for normal load oscillated at 0.12, 0.3 and 0.9 Hz. Shear stress under the normal load oscillating with the slowest frequency (Figure 5.20a) exhibits a hysteresis behavior, similar to that from

O'Sullivan, shown in Figure 5.19c. Shear stress under higher normal load oscillation frequency (Figure 5.20c) presents a trend similar to the load-unload experiment from Feda, shown in Figure 5.19a. These results provide a general qualitative validation of the measurements analyzed during the oscillating load experiments of this study.

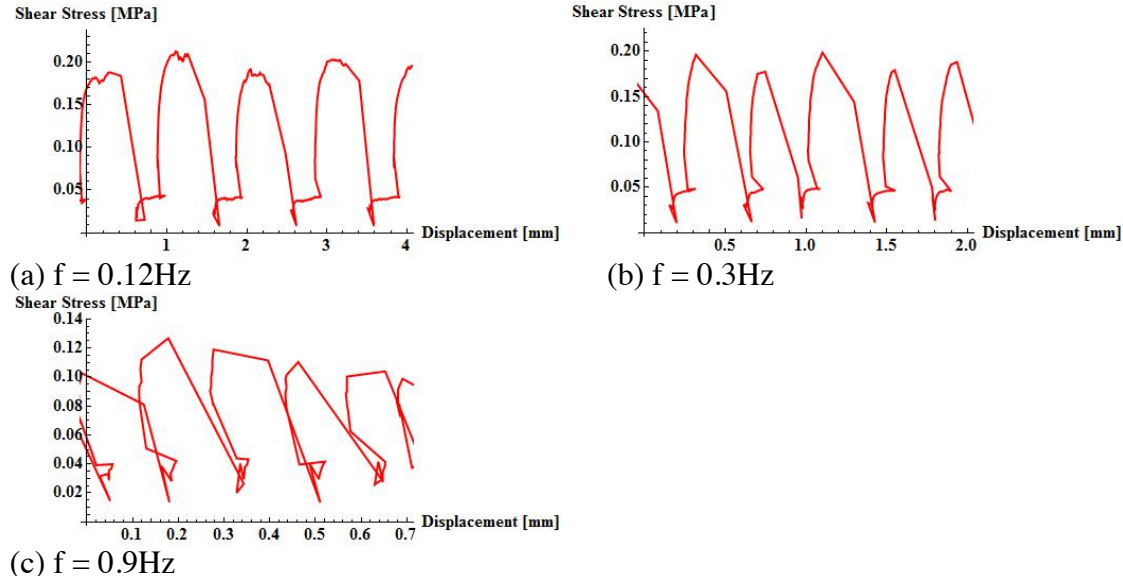


Figure 5.20. Shear stress versus displacement for 2mm diameter chrome steel bearing balls under normal load oscillating between 0.12MPa and 0.55MPa at: (a)  $f = 0.12\text{Hz}$ , (b)  $f = 0.3\text{Hz}$ , (c)  $f=0.9\text{Hz}$ .

A normal force applied to granular media could cause a negative shear cell displacement with respect to the shearing direction through the schematic presented in Figure 5.21. The change in shear cell displacement direction caused by the oscillating normal load makes it difficult to perform an exponential decay fit analysis on shear stress with respect to displacement. However, the shear stress versus displacement data could potentially serve as a tool in granular media force chain structure analysis. Depending on the force chain structure developed in the granular media, the magnitude of shear cell displacement due to the applied normal load can vary. Hence, the changes in shear stress slope (representing the shear modulus), mostly evident during the experiment under high normal load oscillation frequency (Figure 5.20c), could be attributed to the change in force chain structure over time.

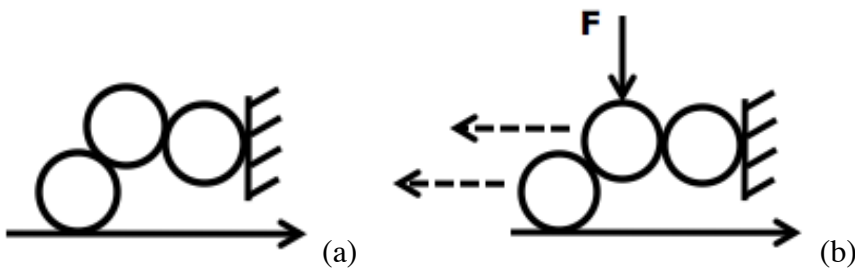


Figure 5.21. A schematic presenting a change in shear cell displacement due to the normal force applied.

A change in shear cell displacement due to the oscillating normal load is also expected to affect the shear speed measurements. Figure 5.22 presents sample shear stress versus time plots for both static and oscillating normal load experiments, as well as the corresponding measured shear cell speed plots. During both of these experiments, the same steady-state average shear rate ( $0.003\text{ s}^{-1}$ ) and maximum normal load (0.55 MPa) were applied. Normal load variation results in a considerable variation in shearing speed, as presented in Figure 5.22d, when compared to the speed for a static load experiment (Figure 5.22c). The speed spikes observed in Figure 5.22d show considerable magnitude variations, which could be caused by changes in the force chain structure within the granular medium. The speed spikes could also cause the increase in the decay exponents measured for oscillating normal load, presented in Figure 5.18, compared to the static load decay exponent results (Figure 5.8).

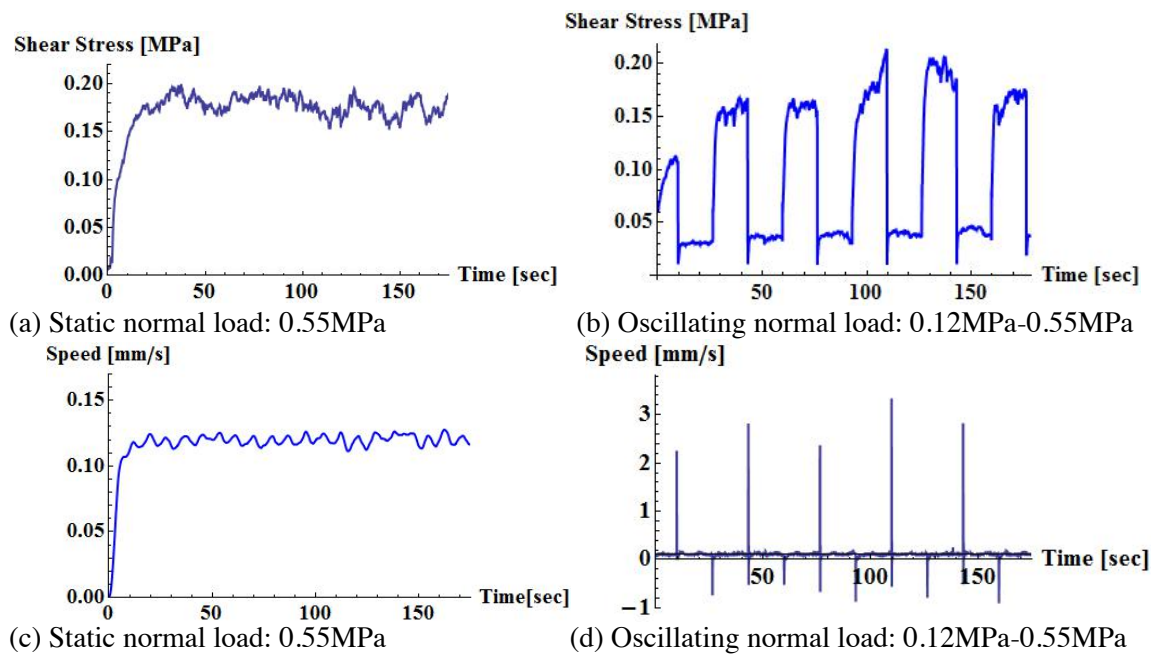


Figure 5.22. 2 mm diameter steel balls, sheared at  $0.003 \text{ s}^{-1}$  (a) Shear stress versus time during a static load test with normal load of 0.55 MPa, (b) Shear stress versus time during experiment with normal load oscillating between 0.12 MPa to 0.55 MPa, (c) Shear cell speed measured during the experiment presented in Figure 5.22a, data were smoothed using a Monte Carlo analysis, (d) Shear cell speed measured during the experiment presented in Figure 5.22b (data are not smoothed).

## **VI. CONCLUSIONS AND FUTURE WORK RECOMMENDATIONS**

The research study presented in this project introduced the author to the field of granular media testing, and provided a general knowledge of hot- and warm-forming of metal alloy sheet materials. This project also produced a direct shear cell instrument that was used to measure the basic mechanical properties of granular media. The direct shear cell allowed testing of different types of granular media under relatively high normal loads, which could be oscillated with controlled frequency and amplitude. This instrument was designed to allow relatively easy reconfiguration for new options, a valuable quality if new testing requirements arise. Any redesign for new options will be assisted by the 3D CAD model provided for the existing instrument. Data acquisition and control systems, as well as data analysis software, were generated during this study.

Throughout the course of this project, granular media were tested under a variety of conditions to simulate the granular flow behavior expected in a working medium for warm-forming of sheet material. Data were acquired for different types of granular media tested in shear under both static and oscillating normal loads. The static normal load experiments revealed shear stress oscillations during granular media flow. This effect is attributed to jamming behavior occurring within the granular media structure, since the oscillation frequency measured was equivalent to the media diameter. These stress fluctuations could produce an inhomogeneous force distribution if granular media are utilized as a force transfer medium in the process of warm-forming sheet materials. The shear stress fluctuations in this study were observed for spherical granular media under dense-packed conditions; no shear stress oscillations were observed for sand. These shear stress fluctuations, which occurred during direct shear tests, should be taken into account when evaluating granular media performance as a working fluid for material forming.

The experiments conducted under an oscillating normal load revealed an opportunity to reduce the maximum shear stress during granular media flow. Although sand shows a higher steady-state shear stress than bearing balls, the maximum shear stress in sand may be decreased to the level of steady-state shear stress for steel bearing

balls by oscillating the normal load. The load oscillation frequency required for sand is relatively low because of the long transient period observed for sand, i.e., its small decay constant,  $\eta$ . Granular media shear stress control by normal force oscillation could be practically applied during warm-forming of sheet metals. It is expected that under lower shear stress the granular media will flow more easily while the metal sheet undergoes deformation.

A comparison between shear stress simulation for static normal load and oscillating normal load experiments is presented in Figure 6.1. The simulated oscillating normal load square wave is presented in Figure 6.1a. The average normal load during the oscillating load simulation is equal to the normal load applied during the static load simulation. If the granular media hysteresis effects are neglected, then the average shear forces for static and oscillating normal load may be considered directly proportional to the energy required to transport the granular medium. Figure 6.1b shows that no major shear force advantage is expected for normal load oscillating at low frequency and low normal load amplitude. However, the average shear force is expected to decrease with an increase in load oscillation frequency (Figure 6.1c) or normal load amplitude (Figure 6.1d). The greatest shear force advantage may be observed by oscillating normal load with high frequency and high amplitude, as presented in Figure 6.1e. Hence, it is expected that increasing both normal load amplitude and oscillation frequency should enhance the flow behavior of granular media.

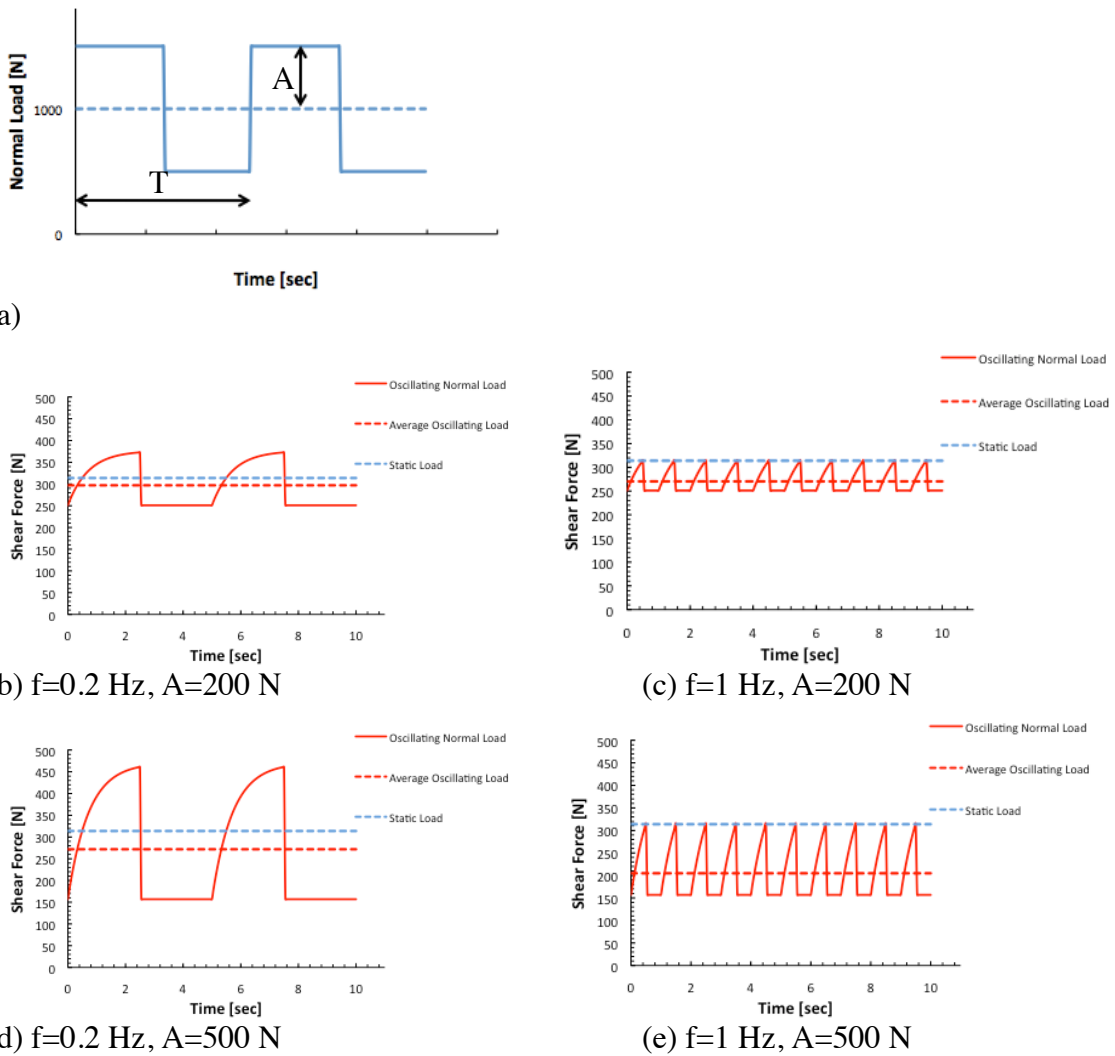


Figure 6.1. Granular media shear stress model comparison between steady state static load and oscillating normal load experiments for 2 mm steel bearing balls. The simulations are conducted at shear rate of  $0.003 \text{ s}^{-1}$ , or shearing speed of  $0.12 \text{ mm/s}$ . The average oscillating normal load equals  $1\text{kN}$ , which is equal to the static load applied, for each simulation. Oscillating normal load applied during the simulation is presented in (a). The oscillating load is simulated with the following frequency  $f$ , and normal load amplitude  $A$ : b)  $f=0.2\text{Hz}$ ,  $A=200\text{N}$ , c)  $f=1\text{Hz}$ ,  $A=200\text{N}$ , d)  $f=0.2\text{Hz}$ ,  $A=500\text{N}$ , e)  $f=1\text{Hz}$ ,  $A=500\text{N}$ .

The shear stress simulations presented in Figure 6.1 contain several simplifications. Shear stress oscillations were neglected for the static load experiment. The oscillating load simulations do not contain the harmonic normal load oscillations, due to the instrument vibrations; hence, a square wave normal load input is used. The decay exponent  $\eta$  was assumed constant for all the simulations, at an average value of  $1.4 \text{ s}^{-1}$ . Although it should be noted that decay exponent variation was observed for different normal load amplitudes and oscillation frequencies during the experimental study. It is also assumed that when the low normal load is applied relaxation occurs instantaneously and the shear stress reaches the steady state value, which is in close agreement with the experimental results obtained for chrome steel bearing balls. This assumption would not be appropriate for sand simulations, because sand exhibits dense medium characteristic when low normal load is applied during oscillating normal load experiments.

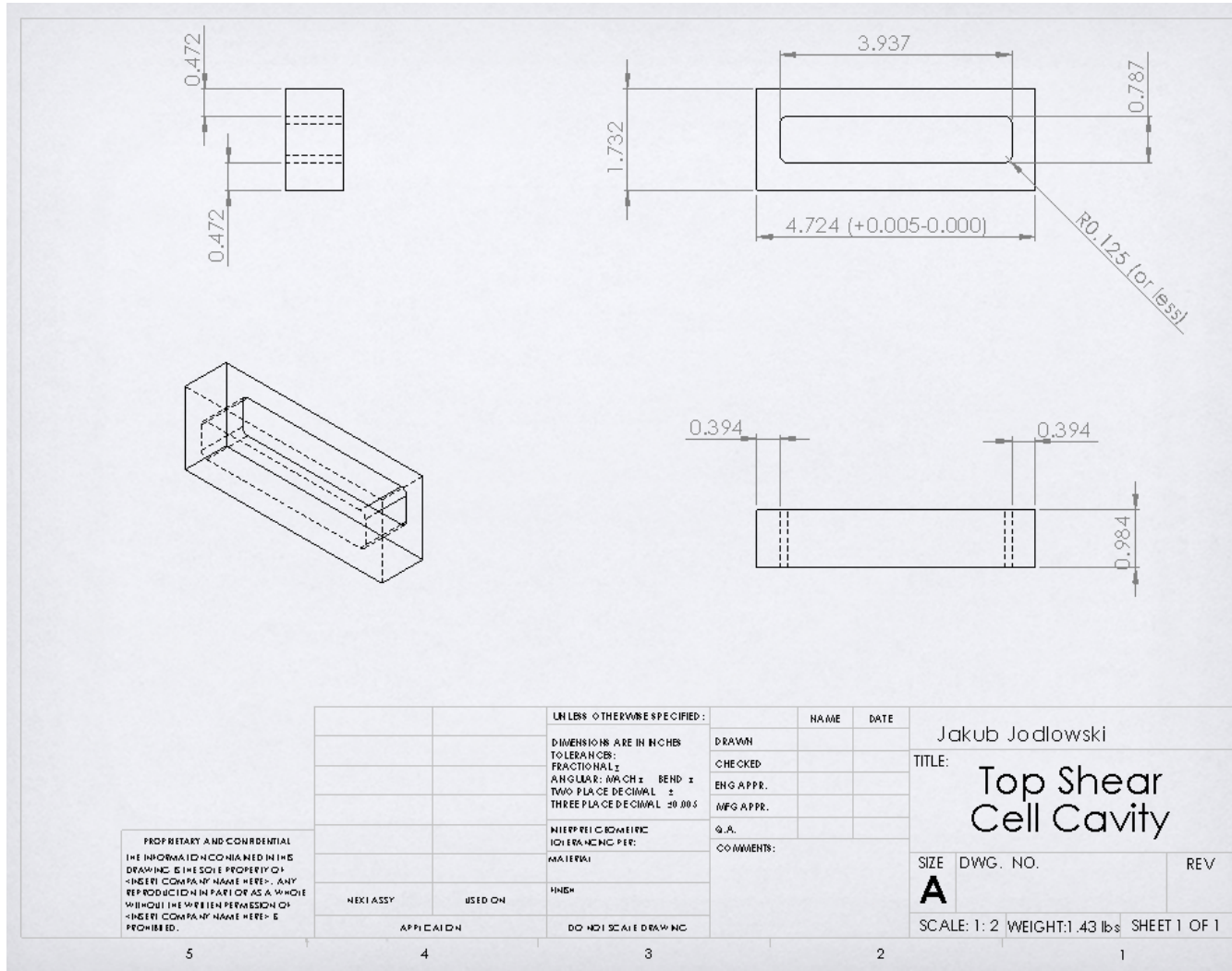
It is recommended that future research study sheet metal deformation with granular media as a force transfer medium. Currently, a gas-pressure bulge forming instrument is available in the research facility, and it could potentially serve as an initial design concept for a granular media-forming machine. The instrument should allow comparing the sheet metal forming properties for different types of granular media, such as steel bearing balls and sand, under both constant and oscillating normal loads. An MTS servo-hydraulic testing machine available in the laboratory could be used in the load application process. Sand requires lower normal load frequency oscillations, and it is expected to be more compatible with the MTS instrument, which has limited load oscillation frequency capabilities. A study should also measure granular media force distribution on the sheet material being forced. The force distribution could either be studied by using force marking materials, such as carbon paper, or by studying the resultant sheet shapes. Discrete element simulations could be developed concurrently to obtain a model for granular media behavior during forming applications.

The literature review and the direct shear test experimental data obtained in this study provide predictions with regards to utilizing granular media as a force transfer

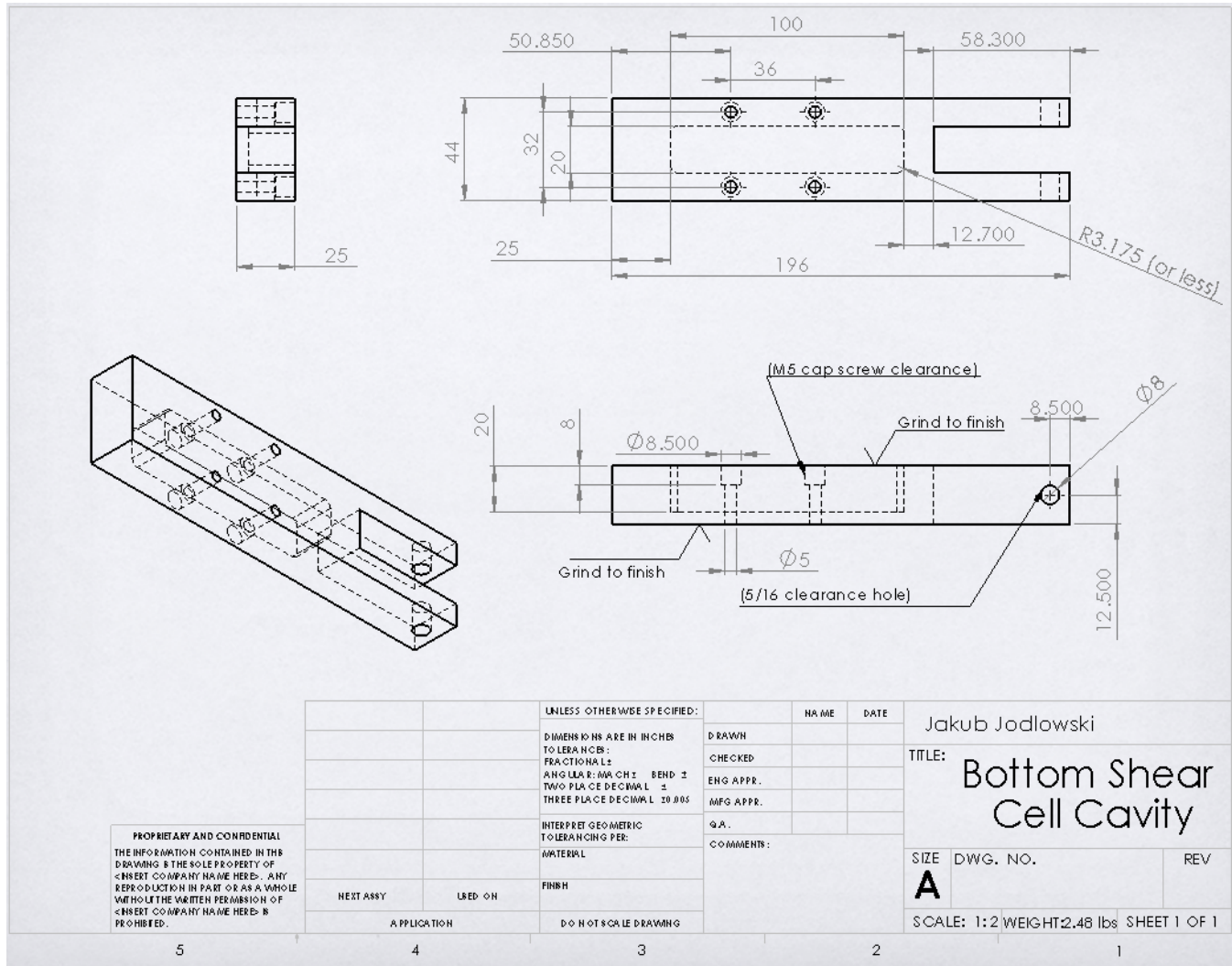
medium for sheet forming. However, actual forming experiments and simulations, such as discrete element simulations, need to be conducted to better understand the force transfer capabilities of granular media.

## **Appendix A: Technical Drawings**

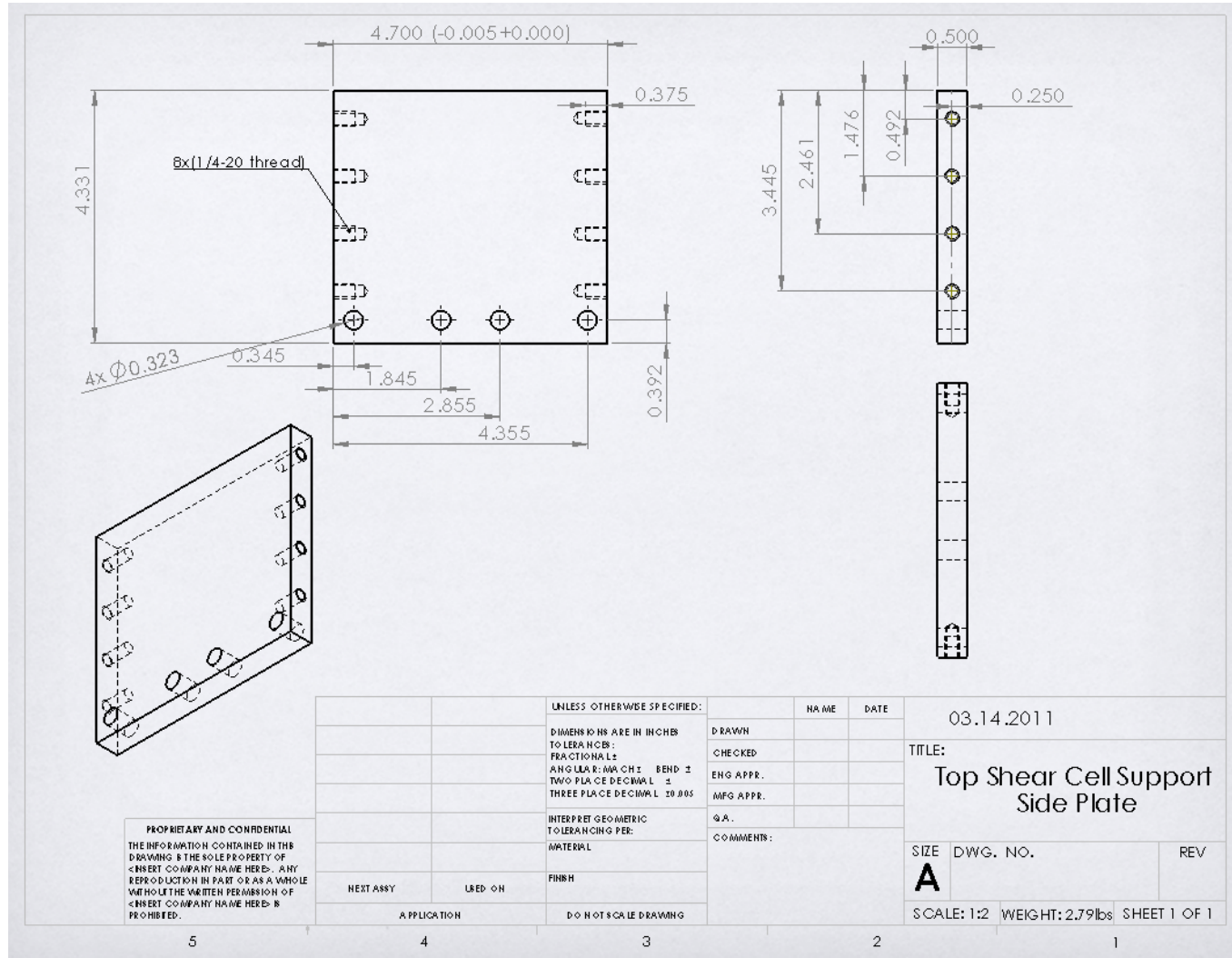
## TOP SHEAR CELL CAVITY



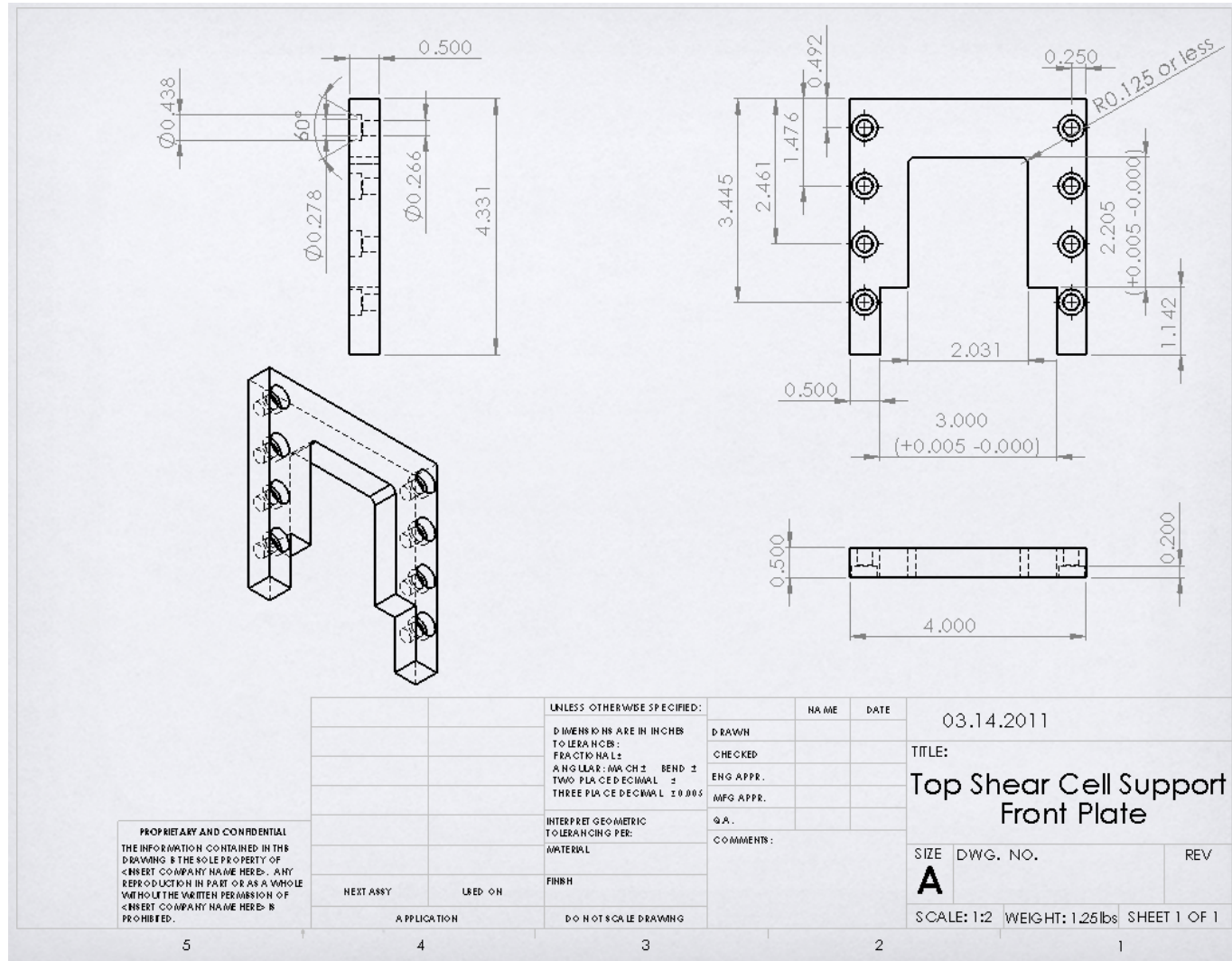
## BOTTOM SHEAR CELL CAVITY



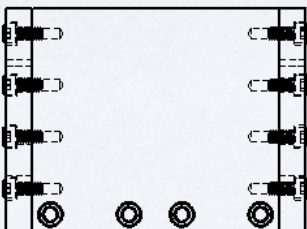
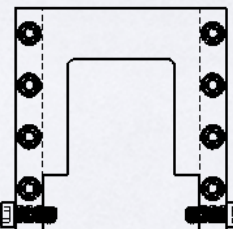
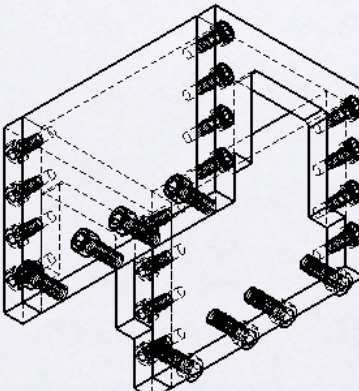
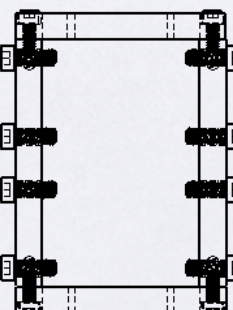
## TOP SHEAR CELL SUPPORT SIDE PLATE



## TOP SHEAR CELL SUPPORT FRONT PLATE



## TOP SHEAR CELL SUPPORT ASSEMBLY

  																													
<p><b>PROPRIETARY AND CONFIDENTIAL</b></p> <p>THE INFORMATION CONTAINED IN THIS DRAWING IS THE SOLE PROPERTY OF &lt;INSERT COMPANY NAME HERE&gt;. ANY REPRODUCTION IN PART OR AS A WHOLE WITHOUT THE WRITTEN PERMISSION OF &lt;INSERT COMPANY NAME HERE&gt; IS PROHIBITED.</p>																													
<table border="1" style="width: 100%; border-collapse: collapse;"> <tr> <td style="width: 10%;">NEXT ASSY</td> <td style="width: 10%;">USED ON</td> <td style="width: 10%;">FINISH</td> <td style="width: 10%;">APPLIED</td> <td style="width: 10%;">DO NOT SCALE DRAWING</td> </tr> </table>		NEXT ASSY	USED ON	FINISH	APPLIED	DO NOT SCALE DRAWING																							
NEXT ASSY	USED ON	FINISH	APPLIED	DO NOT SCALE DRAWING																									
<table border="1" style="width: 100%; border-collapse: collapse;"> <tr> <td colspan="2">UNLESS OTHERWISE SPECIFIED:</td> <td>NAME</td> <td>DATE</td> </tr> <tr> <td colspan="2">DIMENSIONS ARE IN INCHES</td> <td>DRAWN</td> <td></td> </tr> <tr> <td colspan="2">TO LENGTHS:</td> <td>CHECKED</td> <td></td> </tr> <tr> <td colspan="2">FRACTIONAL ± ANGULAR MACHINING ± TWO PLACE DECIMAL ± THREE PLACE DECIMAL ±</td> <td>ENG APPR.</td> <td></td> </tr> <tr> <td colspan="2"></td> <td>MFG APPR.</td> <td></td> </tr> <tr> <td colspan="2">INTERPRET GEOMETRIC TOLERANCING PER:</td> <td>QA.</td> <td></td> </tr> <tr> <td colspan="2">MATERIAL</td> <td colspan="2">COMMENTS:</td> </tr> </table>		UNLESS OTHERWISE SPECIFIED:		NAME	DATE	DIMENSIONS ARE IN INCHES		DRAWN		TO LENGTHS:		CHECKED		FRACTIONAL ± ANGULAR MACHINING ± TWO PLACE DECIMAL ± THREE PLACE DECIMAL ±		ENG APPR.				MFG APPR.		INTERPRET GEOMETRIC TOLERANCING PER:		QA.		MATERIAL		COMMENTS:	
UNLESS OTHERWISE SPECIFIED:		NAME	DATE																										
DIMENSIONS ARE IN INCHES		DRAWN																											
TO LENGTHS:		CHECKED																											
FRACTIONAL ± ANGULAR MACHINING ± TWO PLACE DECIMAL ± THREE PLACE DECIMAL ±		ENG APPR.																											
		MFG APPR.																											
INTERPRET GEOMETRIC TOLERANCING PER:		QA.																											
MATERIAL		COMMENTS:																											
<table border="1" style="width: 100%; border-collapse: collapse;"> <tr> <td>SIZE</td> <td>DWG. NO.</td> <td>REV</td> </tr> <tr> <td>A</td> <td></td> <td></td> </tr> <tr> <td colspan="2">SCALE: 1:2</td> <td>WEIGHT: SHEET 1 OF 1</td> </tr> </table>		SIZE	DWG. NO.	REV	A			SCALE: 1:2		WEIGHT: SHEET 1 OF 1																			
SIZE	DWG. NO.	REV																											
A																													
SCALE: 1:2		WEIGHT: SHEET 1 OF 1																											

## **Appendix B: Load Cell Measuring Shear Force**

The following pages were taken from Honeywell® catalog  
([www.honeywell.com/sensotec](http://www.honeywell.com/sensotec))

**Honeywell**

## Model 41

---

### Precision Low Profile Load Cell



#### DESCRIPTION

Model 41 is a low profile "pancake" type load cells. These bonded foil, strain gage load cells are engineered to measure loads from 5 lb to 500,000 lb. The tension/ compression Model 41 is designed with the threaded hole running completely through the center of the cell. Model 41 utilizes two stabilizing diaphragms, which are welded to the sensing member to

reduce off-center and side-loading effects. It provides high performance in non-linearity, hysteresis, and repeatability specifications for such applications as tube mills, extruding processes and weighing. Each unit has a welded construction and can be hermetically sealed for added durability. Model 41 load cells are available with optional 0 Vdc to 5 Vdc or 4 mA to 20 mA output.



#### FEATURES

- 0.1 % accuracy
- 5 lb to 500000 lb
- mV/V output (standard); 4 mA to 20 mA and 0 Vdc to 5 Vdc (optional) outputs
- Double diaphragm design
- Intrinsically safe available (2N option only)<sup>16</sup>
- CE approved<sup>17</sup>

## Model 41

### PERFORMANCE SPECIFICATIONS

Characteristic	Measure
Load ranges <sup>1)</sup>	5 lb to 500000 lb
Non-linearity, 5 lb to 25 lb	$\pm 0.2\%$ full scale
Hysteresis, 50 lb to 500000 lb	$\pm 0.1\%$ full scale
Hysteresis, 5 lb to 25 lb	$\pm 0.1\%$ full scale
Hysteresis, 50 lb to 500000 lb	$\pm 0.08\%$ full scale
Non-repeatability, 5 to 25 lb	$\pm 0.1\%$ full scale
Non-repeatability, 50 lb to 500000 lb	$\pm 0.03\%$ full scale
Output (tolerance), 5 lb to 25 lb	2 mV/V $\pm 0.5\%$ full scale
Output (tolerance), 50 lb to 500000 lb	3 mV/V $\pm 0.5\%$ full scale
Operation	Compression/tension <sup>1)</sup>
Resolution	Infinite
Standard calibration	5-point calibration: 0 %, 50 % and 100 % of full scale in tension only

### ENVIRONMENTAL SPECIFICATIONS

Characteristic	Measure
Temperature, operating	-54 °C to 121 °C [-65 °F to 250 °F]
Temperature, compensated	15 °C to 71 °C [60 °F to 160 °F]
Temperature effect, zero	0.002 % full scale/°F
Temperature effect, span	0.002 % full scale/°F

### ELECTRICAL SPECIFICATIONS

Characteristic	Measure
Strain gage type	Bonded foil
Excitation (calibration)	10 Vdc
Insulation resistance	5000 mOhm @ 50 Vdc
Bridge resistance (tolerance)	350 ohm (nominal)
Zero balance (tolerance)	$\pm 1\%$ full scale
Shunt calibration data	Included
Electrical termination (std) 5 lb to 5000 lb	PTIH-10-6P
Electrical termination (std) 7500 lb to 500000 lb	MS3102E-14S-6P
Mating connector 5 lb to 5000 lb (not incl.)	PT06A-10-6S or equiv. (AA111)
Mating connector 7500 to 500000 lb (not incl.)	MS3106A-14S-6S (AA121)

### MECHANICAL SPECIFICATIONS

Characteristic	Measure
Maximum allowable load	150 % FS <sup>1)</sup>
Weight	See table
Material	17-4PH stainless steel
Less than 200,000 lb	
Material greater than or equal to 300000 lb	Carbon steel
Deflection	See table
Natural frequency	See table

### RANGE CODES

Range Code	Available ranges	Range Code	Available ranges
AT	5 lb	DV	10000 lb
AV	10 lb	EJ	15000 lb
BL	25 lb	EL	20000 lb
BN	50 lb	EN	30000 lb
BR	100 lb	EP	50000 lb
CN	250 lb	ER	75000 lb
CR	500 lb	ET	100000 lb
CV	1000 lb	FJ	150000 lb
DL	2000 lb	FL	200000 lb
DN	3000 lb	FN	300000 lb
DP	4000 lb	FP	400000 lb
DR	5000 lb	FR	500000 lb
DT	7500 lb		

### WIRING CODES

Connector	Unamplified (Std.)
A	(+) excitation
B	(+) excitation
C	(-) excitation
D	(-) excitation
E	(-) output
F	(+) output

### DEFLECTIONS AND RINGING FREQUENCIES

Capacity (lb)	Deflection @ full scale (in)	Natural ringing frequency (Hz)	Weight (lb)
5 to 25	0.001	2000	0.8
50 to 1000	0.002	4800	1.5
2000 to 5000	0.002	10000	2.0
7500 to 15000	0.003	6000	8.8
20000 to 50000	0.004	8000	11.0
75000 to 100000	0.006	5500	30.9
150000 to 200000	0.010	4500	46.3
300000 to 500000	0.010	4100	130.1

**Honeywell**

## Precision Low Profile Load Cell

### INTERNAL AMPLIFIERS

Amplifier specifications	Voltage output: Option 2b	Voltage output: Option 2c	Voltage output: Option 2t	Current three-wire: Option 2j	Current two-wire: Option 2k	Intrinsically safe amp: Option 2n (2N)***
<b>Output signal</b>	±5 V	0-5 V or ±5 V @ 45 mA	0-10 V or ±10 V @ 45 mA	4 mA to 20 mA	4 mA to 20 mA	4 mA to 20 mA
<b>Input power (voltage)</b>	±15 Vdc or 26-32 Vdc	11 Vdc to 28 Vdc	15 Vdc to 28 Vdc	22 Vdc to 32 Vdc	9 Vdc to 32 Vdc	9 Vdc to 28 Vdc
<b>Input power (current)</b>	45 mA	40 mA	40 mA	65 mA	4 mA to 28 mA	4 mA to 24 mA
<b>Freq. response</b>	3000 Hz	3000 Hz	3000 Hz	2500 Hz	300 Hz	2000 Hz
<b>Power supply rejection</b>	60 db	60 db	60 db	60 db	60 db	60 db
<b>Operating temperature</b>	-20 °F to 185 °F	-20 °F to 185 °F	-20 °F to 185 °F	0 °F to 185 °F	0 °F to 185 °F	-20 °F to 185 °F
<b>Reverse volt. protection</b>	Yes	Yes	Yes	Yes	Yes	Yes
<b>Short circuit protection</b>	Momentary	Momentary	Momentary	Yes	Yes	Yes
<b>Wiring code: connector</b>	A (+) Supply B Output common C Supply return D (+) Output E Shunt Cal 1 F Shunt Cal 2	A (+) Supply B Output common** C Supply return** D (+) Output E Shunt Cal 1 F Shunt Cal 2	A (+) Supply B Output common** C Supply return** D (+) Output E Shunt Cal 1 F Shunt Cal 2	A (+) Supply B Output common** C Supply return** D (+) Output E Shunt Cal 1 F Shunt Cal 2	A (+) Supply B No connection C No connection D (+) Output E Case ground F No connection	A (+) Supply B No connection C No connection D (+) Output E Case ground F No connection
<b>Wiring code: cable</b>	R (+) Supply Bl Output common G Supply return W (+) Output B Shunt Cal 1 Br Shunt Cal 2	R (+) Supply Bl Output com* G Supply return* W (+) Output B Shunt Cal 1 Br Shunt Cal 2	R (+) Supply Bl Output com* G Supply return* W (+) Output B Shunt Cal 1 Br Shunt Cal 2	R (+) Supply Bl Output com* G Supply return* W (+) Output B Shunt Cal 1 Br Shunt Cal 2	R (+) Supply Bl (+) Output W Case ground	R (+) Supply Bl (+) Output W Case ground

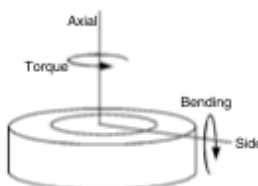
\* Black and green wires are internally connected.

\*\* Pins B and C are internally connected.

\*\*\* See our Web site (<http://measurementsensors.honeywell.com>) for the most up-to-date information regarding intrinsically safe approvals, ref. #008-0547-00.

### ALLOWABLE MAXIMUM LOADS

Capacity (lb)	Side load (lb)	Bending (lb-in)	Torque (lb-ft)
5 to 25	50 %	40 %	25 %
50 to 1000	45 %	35 %	25 %
2000 to 5000	30 %	25 %	25 %
7500 to 30000	20 %	20 %	15 %
50000 to 100000	20 %	20 %	15 %
150000 to 200000	20 %	20 %	15 %
300000	20 %	20 %	10 %
400000	20 %	20 %	10 %
500000	20 %	20 %	10 %



Honeywell • Sensing and Control 3

## Model 41

### OPTION CODES

	Many range/option combinations are available in our quick-ship and fast-track manufacture programs. Please see <a href="http://measurementsensors.honeywell.com">http://measurementsensors.honeywell.com</a> for updated listings.			
<b>Load ranges</b>	5, 10, 25, 50, 100, 250, 500, 1000, 2000, 5000, 3000, 4000, 7500, 10000, 15000, 20000, 30000, 50000, 75000, 100000, 150000, 200000, 300000, 400000, 500000 lb	1d. -20 °F to 130 °F 1e. -20 °F to 200 °F 1f. 70 °F to 250 °F	1g. 70 °F to 325 °F <sup>14</sup> 1h. 70 °F to 400 °F <sup>14</sup> 1i. -65 °F to 250 °F <sup>14</sup>	1j. 0 °C to 50 °C 1k. -20 °C to 85 °C 1m. -25 °C to 110 °C
<b>Temperature compensation</b>	1a. 60 °F to 160 °F 1b. 30 °F to 130 °F 1c. 0 °F to 185 °F	2b. 4 wire, ±5 Vdc 2c. 0-5 Vdc output 2k. 4 mA to 20 mA (two-wire) <sup>15</sup>	2j. 4-20 mA (three-wire) output 2n (2N) 4 mA to 20 mA (wire) intrinsically safe <sup>16</sup> 2t. 0 Vdc to 10 Vdc	2u. Unamplified, mV/V output
<b>Internal amplifiers<sup>18</sup></b>	3a. Input/output isolation <sup>19</sup> 3d. Remote buffered shunt calibration <sup>20</sup>			
<b>Overload stops</b>	4a. Overload stops			
<b>Electrical termination</b>	6a. Bendix PTIH-10-6P 6-pin (ranges to 5000 lb) 6b. MS3102E-14S-6P (ranges 7500 lb and up) <sup>21</sup> 6e. Integral cable: Teflon	6f. Integral cable: PVC 6g. Integral cable: Neoprene <sup>22</sup> 6h. Integral cable: Silicone	6i. Integral underwater cable <sup>23</sup> 6j. 1/2-14 conduit fitting with 5 ft of 4 conductor PVC cable	6q. Molded integral cable polyurethane <sup>24</sup> 6v. Phoenix connector on end of cable
<b>Shunt calibration</b>	8a. Precision internal resistor <sup>25</sup>			
<b>Special calibration</b>	9a. 10 point (5 up/5 down) 20 % increments @ 68 °F 9b. 20 point (10 up/10 down) 10 % increments @ 68 °F 9c. ASTM E-74 calibration			
<b>Bridge resistance</b>	12b. 5000 ohm (foil)			
<b>Zero and span adjustment</b>	14a. No access to pots 14b. Top access to pots			
<b>Electrical connector orientation</b>	15a. Horizontal electrical exit port orientation 15b. Vertical electrical exit port orientation		15c. Radial electrical exit port orientation 15d. Connector on end of cable	
<b>Special calibration</b>	30a. Compression only calibration, positive in compression 30b. Tension and compression calibration, positive in tension 30c. Compression only calibration, negative in compression 30d. Tension and compression calibration, positive in compression			
<b>Bridge type</b>	31a. Dual bridge			
<b>Shock and vibration</b>	44a. Shock and vibration resistance			
<b>Interfaces</b>	53e. Signature calibration <sup>14</sup> 53t. TEDS IEEE 1451.4 module <sup>15</sup>			

**Honeywell**

## Precision Low Profile Load Cell

### MOUNTING DIMENSIONS

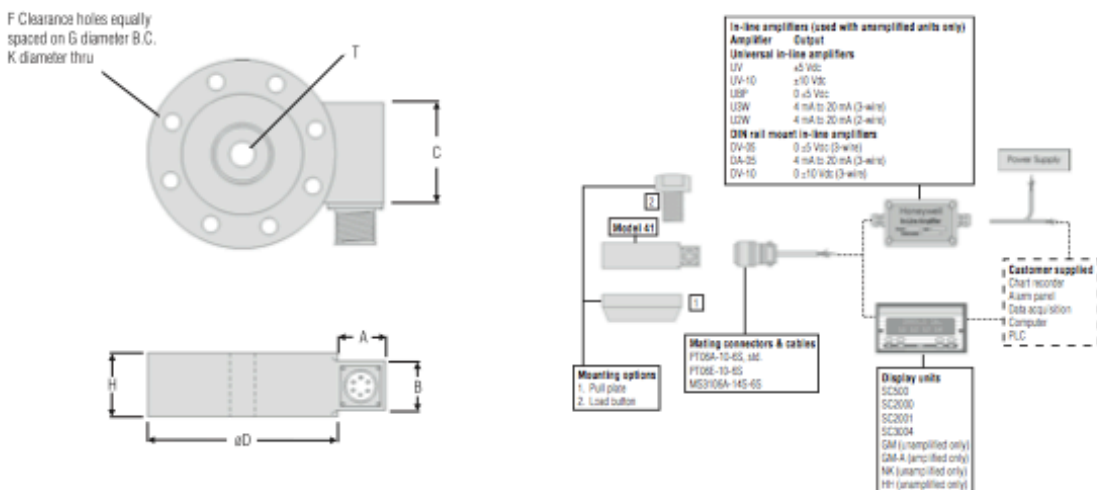
Ranges lb	D mm [in]	H mm [in]	H*** mm [in]	F#	ØG mm [in] B.C.	ØK mm [in] thru	T	A mm [in]	A* mm [in]	B mm [in]	B* mm [in]	C mm [in]
5, 10, 25	63,5 [2.50]	20,32 [0.80]	44,45 [1.75]	6	50,8 [2.000]	4,83 [0.19]	1/4-28 UNF	20,83 [0.82]	63,5 [2.5]	19,05 [0.75]	22,86 [0.9]	31,75 [1.25]
50, 100, 250, 500, 1000	76,2 [3.00]	25,4 [1.00]	44,45 [1.75]	6	57,15 [2.250]	7,11 [0.28]	3/8-24 UNF	20,83 [0.82]	63,5 [2.5]	19,05 [0.75]	22,86 [0.9]	31,75 [1.25]
2000, 3000, 4000, 5000	88,9 [3.50]	25,4 [1.00]	44,45 [1.75]	6	66,68 [2.625]	8,64 [0.34]	1/2-20 UNF	20,83 [0.82]	63,5 [2.5]	19,05 [0.75]	22,86 [0.9]	31,75 [1.25]
7500, 10000, 15000	139,7 [5.50]	45,7 [1.80]	45,7 [1.80]	8	114,3 [4.500]	10,16 [0.40]	1-14 UNS	31,75 [1.25]	58,42 [2.3]	38,1 [1.50]	38,1 [1.5]	50,8 [2.00]
20000, 30000, 50000	152,4 [6.00]	45,7 [1.80]	45,7 [1.80]	8	123,83 [4.875]	13,46 [0.53]	1 1/2-12 UNF	31,75 [1.25]	58,42 [2.3]	38,1 [1.50]	38,1 [1.5]	50,8 [2.00]
75000, 100000	228,6 [9.00]	63,5 [2.50]	63,5 [2.50]	12	196,85 [7.750]	16,76 [0.66]	2-12 UN	31,75 [1.25]	58,42 [2.3]	38,1 [1.50]	38,1 [1.5]	50,8 [2.00]
150000, 200000	279,4 [11.00]	63,5 [2.50]	63,5 [2.50]	12	241,3 [9.500]	19,81 [0.78]	2 1/2-12 UN	31,75 [1.25]	58,42 [2.3]	38,1 [1.50]	38,1 [1.5]	50,8 [2.00]
300000, 400000, 500000	355,6 [14.00]	107,95 [4.25]	107,95 [4.25]	12	298,45 [11.750]	26,16 [1.03]	3 1/2-8 UN	31,75 [1.25]	58,42 [2.3]	38,1 [1.50]	38,1 [1.5]	**

\* Length of load cell with amplified option (see option codes)

\*\* C dimension varies on high ranges. Consult factory

\*\*\* H dimension with 2n(2N) amplifier

### TYPICAL SYSTEM DIAGRAM



## **Appendix C: LVDT**

The following pages were taken from Honeywell® catalog  
([www.honeywell.com/sensotec](http://www.honeywell.com/sensotec))

## Model VL7A AC-AC Long Stroke LVDT

Order Code BY122

- +/- 0.5 to 3.0 in. Ranges
- Stainless Steel Construction
- 0.25% Non-Linearity
- Spring Return



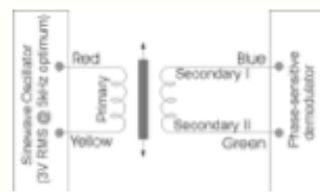
### Dimensions



Order Code with Ranges	Available Ranges	L (in.)	X (in.)	Approx. Unit Weight (oz.)	Typical F.S. Output @ 3V RMS
BY122HP	+/- 0.5 in.	5.35	1.5	6.5	2.4V RMS
BY122HQ	+/- 1.0 in.	6.35	2.5	8.0	3.0V RMS
BY122HR	+/- 2.0 in.	11.0	3.0	14.0	4.8V RMS
BY122HS	+/- 3.0 in.	15.35	4.5	17.0	4.5V RMS

### Wiring Codes

Wire	Supply
Red	(+) Supply (Calibrated @ 3V RMS 5 kHz)
Yellow	Supply Return
Blue	Output
Green	Output Return
Black	Secondary Center Tap (normally not connected)



### Performance

Stroke Range.....	+/- 0.5 to 3.0 in.
Non-Linearity (max.).....	+/- 0.25% Full Scale
Non-Repeatability (max.).....	<20 microinches
Output Sensitivity.....	See table above
Resolution.....	Infinite

### Environmental

Temperature, Operating.....	-58° to 257°F
Temperature, Effect.....	
Zero (max.).....	0.006% Full Scale/°F
Span (max.).....	0.006% Full Scale/°F

### Electrical

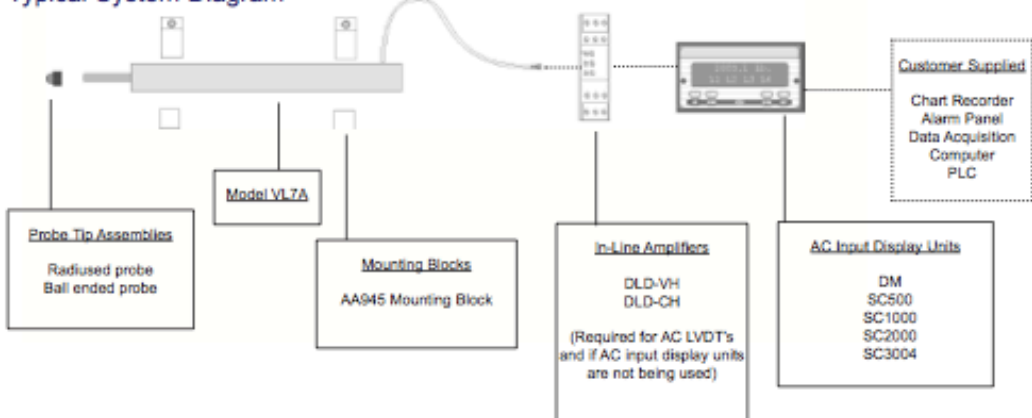
Element Type.....	AC-AC LVDT
Input Supply (calibrated).....	3 V RMS @ 5 kHz
Input Supply (acceptable).....	1-7 V RMS @ 2-10 kHz
Electrical Termination.....	Multiconductor shielded cable

### Mechanical

Material.....	Stainless Steel
Probe Material.....	Stainless Steel
Armature Type.....	Captive Guided Spring Return
Probe Thread.....	Not Applicable
Weight.....	See table above
Spring Force (max.).....	4 oz./in.

Model VL7A

## Typical System Diagram



## Options

	Same Day Ship	Fast Track Delivery	Built to Order
Stroke Ranges	+/- 0.5 to +/- 2.0 in.	+/-3.0 in.	
Electrical Termination	Multiconductor Shielded Cable (6 ft.)		TM405, Axial Bendix connector on body Radial (side) TM406, Bendix connector on body
Electrical Cable Orientation			TM49. Axial cable exit
Mounting Threads			TM511, 13/16 - 32 UNF
Improved Linearity		L10, +/- 0.1% max. linearity (less than or equal to +/- 4 in.)	
Higher Temperature			TM315, 400° F

 Supplied as standard

**Special Customer Requirements  
(Consult Factory)**

Moisture resistant  
Radiation resistance 100M rads  
Longer cable length, limited on certain models  
Threaded body  
Spring retract  
Optional tips  
T.E.D.S. IEEE 1451.4 module  
Signature Calibration

-Not RoHS Compliant

## How to Order

The order code consists of the product model, the desired range code and the available options.

Sample Code: BY122 HQ L10  
Model Code Range Code Options Code

## **Appendix D: Load Cell Measuring Normal Load**

The following pages were taken from Omega® catalog ([www.omega.com](http://www.omega.com))

## LOW-PROFILE PANCAKE STYLE LOAD CELLS STANDARD AND METRIC MODELS

### LCHD/LCMHD Series

Tension/Compression  
Calibrated in Tension  
2.5 kgf to 10,000 kgf

Starts at  
**\$765**



F-59

## SPECIFICATIONS

**Excitation:** 10 Vdc (15 V max)

**Output (FSO):**

≤25 lb/10 kgf: 2 mV/V ±0.25%

≤50 lb/20 kgf: 3 mV/V ±0.25%

**5-Point Calibration (in Tension):**  
0%, 50%, 100%, 50%, 0%

**Linearity:**

≤25 lb/10 kgf: ±0.20% FSO

≤50 lb/20 kgf: ±0.10% FSO

**Hysteresis:**

≤25 lb/10 kgf: ±0.10% FSO

≤50 lb/20 kgf: ±0.10% FSO

**Repeatability:**

≤25 lb/10 kgf: ±0.1% FSO

≤50 lb/20 kgf: ±0.03% FSO

**Zero Balance:** ±1% of FSO

**Operating Temp Range:**

-54 to 121°C (-65 to 250°F)

**Compensated Temp Range:**  
16 to 71°C (60 to 160°F)

**Thermal Effects:**

Zero: 0.0036% FSO/°C

Span: 0.0036% FSO/°C

**Safe Overload:** 150% of capacity

**Ultimate Overload:** 300% of capacity

**Input Resistance:** 350 ±10 Ω

**Output Resistance:** 350 ±10 Ω

**FS Deflection:**

0.025 to 0.076 mm

(0.001 to 0.003") typical

**Construction:** 17-4 PH stainless steel

**Electrical:**

≤5000 lb/2000 kgf: DT02H-10-6P

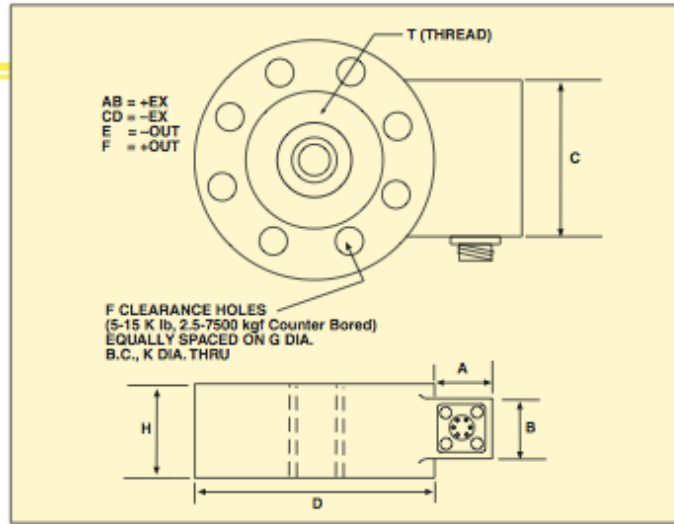
>5000 lb/2500 kgf: MS3102E-14S-6P  
(or equiv.)

**Mating Connector (Included):**

≤5000 lb/2000 kgf: PT06F-10-6S

>5000 lb/2500 kgf: MS3102E-14S-6S  
(or equiv.)

LCHD-TP263, S85, optional tension plate for 2k to 5k LCHD load cells, shown smaller than actual size.



Dimensions: mm (in)

CAPACITY	D	H	F	G	K	T	A	B	C
	STANDARD MODELS								
5 to 25 lb	64 (2.5)	20 (0.80)	6	51 (2.0)	4.6 (0.18)	1/28 UNF	24 (0.94)	19 (0.75)	32 (1.25)
50 to 1K lb	76 (3.0)	25 (1.0)	6	57 (2.25)	7.1 (0.28)	1/24 UNF	24 (0.94)	19 (0.75)	32 (1.25)
2K to 5K lb	89 (3.5)	25 (1.0)	6	67 (2.63)	8.6 (0.34)	1/20 UNF	24 (0.94)	19 (0.75)	32 (1.25)
7.5K to 15K lb	140 (5.5)	46 (1.8)	8	114 (4.5)	10 (0.40)	1-14 UNS	32 (1.25)	38 (1.5)	51 (2.0)
20K to 50K lb	152 (6.0)	46 (1.8)	8	124 (4.88)	13 (0.53)	1/4-12 UNF	32 (1.25)	38 (1.5)	51 (2.0)
75K to 100K lb	229 (9.0)	64 (2.5)	12	197 (7.75)	17 (0.66)	2-12 UN	32 (1.25)	38 (1.5)	51 (2.0)
150K to 200K lb	279 (11)	76 (3.0)	12	241 (9.5)	20 (0.78)	2 1/2-12 UN	32 (1.25)	38 (1.5)	51 (2.0)
300K to 500K lb	356 (14)	108 (4.25)	12	298 (11.75)	25 (1.0)	3 1/2-8 UN	32 (1.25)	38 (1.5)	51 (2.0)
METRIC MODELS									
2.5 to 10 kgf	64 (2.5)	20 (0.80)	6	51 (2.0)	4.6 (0.18)	M6 x 1.00	24 (0.94)	19 (0.75)	32 (1.25)
25 to 500 kgf	76 (3.0)	25 (1.0)	6	57 (2.25)	7.1 (0.28)	M10 x 1.5	24 (0.94)	19 (0.75)	32 (1.25)
1000 to 2500 kgf	89 (3.5)	25 (1.0)	6	67 (2.63)	8.6 (0.34)	M12 x 1.75	24 (0.94)	19 (0.75)	32 (1.25)
5000 to 7500 kgf	140 (5.5)	46 (1.8)	8	114 (4.5)	10 (0.40)	M24 x 2.0	32 (1.25)	38 (1.5)	51 (2.0)
10000 kgf	152 (6.0)	46 (1.8)	8	124 (4.88)	13 (0.53)	M36 x 2.0	32 (1.25)	38 (1.5)	51 (2.0)

## TENSION PLATES

MODEL NO.	PRICE	DESCRIPTION
LCHD-TP225	\$65	Tension plate, 50 to 1000 lb ranges
LCHD-TP263	85	Tension plate, 2000 to 5000 lb ranges
LCHD-TP450	155	Tension plate, 7500 to 15,000 lb ranges
LCHD-TP488	180	Tension plate, 20,000 to 50,000 lb ranges
LCHD-TPXXX	Consult Sales	Tension plate, ranges over 50,000 lb

## LOW-PROFILE PANCAKE STYLE LOAD CELLS



MOST POPULAR MODELS HIGHLIGHTED!

### To Order (Specify Model Number)

CAPACITY	MODEL NO.	PRICE	COMPATIBLE METERS**
<b>STANDARD MODELS</b>			
5 lb	2.3 kgf	LCHD-5	\$765 DPIS, DP41-S, DP25B-S
10 lb	4.5 kgf	LCHD-10	765 DPIS, DP41-S, DP25B-S
25 lb	11 kgf	LCHD-25	765 DPIS, DP41-S, DP25B-S
50 lb	23 kgf	LCHD-50	765 DPIS, DP41-S, DP25B-S
100 lb	45 kgf	LCHD-100	765 DPIS, DP41-S, DP25B-S
250 lb	114 kgf	LCHD-250	765 DPIS, DP41-S, DP25B-S
500 lb	227 kgf	LCHD-500	765 DPIS, DP41-S, DP25B-S
1K lb	455 kgf	LCHD-1K	765 DPIS, DP41-S, DP25B-S
2K lb	909 kgf	LCHD-2K	765 DPIS, DP41-S, DP25B-S
3K lb	1361 kgf	LCHD-3K	765 DPIS, DP41-S, DP25B-S
4K lb	1815 kgf	LCHD-4K	765 DPIS, DP41-S, DP25B-S
5K lb	2269 kgf	LCHD-5K	765 DPIS, DP41-S, DP25B-S
7.5K lb	3403 kgf	LCHD-7.5K	765 DPIS, DP41-S, DP25B-S
10K lb	4537 kgf	LCHD-10K	935 DPIS, DP41-S, DP25B-S
15K lb	6806 kgf	LCHD-15K	935 DPIS, DP41-S, DP25B-S*
20K lb	9074 kgf	LCHD-20K	1075 DPIS, DP41-S, DP25B-S*
30K lb	13,612 kgf	LCHD-30K	1075 DPIS, DP41-S, DP25B-S*
50K lb	22,686 kgf	LCHD-50K	1075 DPIS, DP41-S, DP25B-S*
75K lb	34,029 kgf	LCHD-75K	† DPIS, DP41-S, DP25B-S*
100K lb	45,372 kgf	LCHD-100K	† DPIS, DP41-S, DP25B-S*
150K lb	68,058 kgf	LCHD-150K	† DPIS, DP41-S, DP25B-S*
200K lb	90,744 kgf	LCHD-200K	† DPIS, DP41-S, DP25B-S*
300K lb	136,116 kgf	LCHD-300K	† DPIS, DP41-S, DP25B-S*
400K lb	181,488 kgf	LCHD-400K	† DPIS, DP41-S, DP25B-S*
500K lb	226,860 kgf	LCHD-500K	† DPIS, DP41-S, DP25B-S*
<b>METRIC MODELS</b>			
5.5 lb	2.5 kgf	LCMHD-2.5	\$765 DPIS, DP41-S, DP25B-S
11 lb	5 kgf	LCMHD-5	765 DPIS, DP41-S, DP25B-S
22 lb	10 kgf	LCMHD-10	765 DPIS, DP41-S, DP25B-S
55 lb	25 kgf	LCMHD-25	765 DPIS, DP41-S, DP25B-S
110 lb	50 kgf	LCMHD-50	765 DPIS, DP41-S, DP25B-S
220 lb	100 kgf	LCMHD-100	765 DPIS, DP41-S, DP25B-S
551 lb	250 kgf	LCMHD-250	765 DPIS, DP41-S, DP25B-S
1102 lb	500 kgf	LCMHD-500	765 DPIS, DP41-S, DP25B-S
2205 lb	1000 kgf	LCMHD-1K	765 DPIS, DP41-S, DP25B-S
3307 lb	1500 kgf	LCMHD-1.5K	765 DPIS, DP41-S, DP25B-S
4409 lb	2000 kgf	LCMHD-2K	765 DPIS, DP41-S, DP25B-S
5512 lb	2500 kgf	LCMHD-2.5K	765 DPIS, DP41-S, DP25B-S
11,023 lb	5000 kgf	LCMHD-5K	935 DPIS, DP41-S, DP25B-S
16,535 lb	7500 kgf	LCMHD-7.5K	935 DPIS, DP41-S, DP25B-S
22,046 lb	10,000 kgf	LCMHD-10K	1075 DPIS, DP41-S, DP25B-S

Comes complete with 5-point NIST-traceable calibration and 59 kΩ shunt data.

\* Consult factory. \* 4-digit meter.

\*\* See section D for compatible meters. DPIS meter suitable for one direction measurement only.

Note: Models >300,000 lb are calibrated at 300,000 lb—see Specifications.

Ordering Examples: LCHD-500, 500 lb capacity load cell, \$765.

LCMHD-500, 500 kgf capacity load cell, \$765.

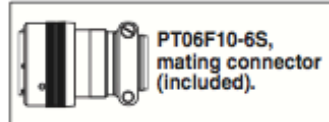
PT06F10-6S, mating connector (included). LCMHD-10K, 10,000 kgf capacity load cell, \$1075.

MS3102E-14S-6S, mating connector (included).



### POPULAR OPTIONS

DESCRIPTION	SUFFIX	PRICE
0-5 Vdc Output (≥5000 kgf)	-5V"	\$135
Overload Stops	-OL"	Consult Factory
Dual Bridge ≤5000 lb/2500 kgf ≥5000 lb/2500 kgf	--DUAL" "--DUAL"	250 350
Extended Temperature Range between: -50 to 93°C (-50 to 200°F) and to 163°C (350°F)	--TC1" "--TC2"	50 125



### ACCESSORIES

MODEL NO.	PRICE	DESCRIPTION
MS3106E-14S-6S	\$64.00	Spare mating connector for units above 5000 lb capacity
PT06F10-6S	26.50	Spare mating connector for units below 7500 lb capacity

## **Appendix E: Solenoid Valve**

The following pages were taken from Norgren® catalog ([www.norgren.com](http://www.norgren.com))



## V60-63 Series

3/2, 5/2, 5/3 and 2 x 3/2 Directional control valves  
Solenoid and pilot actuated  
Rest position and impulse versions

- High flow rate
- Small volumetric size
- Proven sealing system
- Manual override option
- Maintenance-free
- Low power consumption
- Application oriented pilot controls
- Manifold system for easy assembly
- Multiple pressure options



### Technical data

Medium:  
Compressed air, filtered to 50 µm, lubricated\* or non lubricated.

Operation:  
Electromagnetically or pneumatically controlled

Mounting position:  
Optional

Connection:  
G 1/8 up to G 1/2

Operating pressure:  
1,5/2 up to 8/10 bar

Flow direction:  
Internal pilot supply: fixed

External pilot supply: optional

Flow:	Size	3/2, 5/2	2 x 3/2, 5/3
	G1/8	750	500
	G1/4	1300	950
	G3/8	2600	1900
	G1/2	4200	

Ambient temperature:  
-10°C to +50°C

Fluid temperature:  
-10°C to +50°C  
Consult our Technical Service for use below +2°C.

### Materials

Housing and base plate: aluminium  
Spindle: stainless steel,  
Piston, spacers and cover: synthetic material  
Static and dynamic seals: NBR,  
Screws: zinc plated  
Springs: stainless steel.

\* Oil recommendation: Shell Hydrol OO 32, ESSO Febis K 32 (as of 07/92) or comparable oils with DIN values < 8 (DIN 53521) and ISO viscosity class 32 to 46 (DIN 51519)

### Ordering Information

To place an order, choose the valve design and add coil and voltage codes from solenoid variant tables, e.g. **V61B513A-A213L** for a 5/2 valve, solenoid actuated, air spring return, manual override push & lock, 24 V d.c. solenoid according to DIN EN 175 301-803 (DIN 43650 B).

### Connector types

Standard see data sheet	7.7.002
AS-i see data sheet	7.7.003

### Alternative models

NPT ports.



## 3/2 directional control valves, solenoid actuated

Symbol	Model	Part size	Pilot supply	Pilot exhaust	Solenoid variant	Flow (l/min)	Operating pressure (bar)	Pilot pressure (bar)	kg	Dimensional drawing no.
NC	V60413A-Ax***	G1/8	Internal	Not collected	1	750	2...8	—	0.22	1
	V604423A-Ax***	G1/8	External	Not collected	1	750	-0.9...8	3...8	0.22	1
	V604413D-Cx13A	G1/8	Internal	Collected	2	750	2...10	—	0.21	4
	V604423D-Cx13A	G1/8	External	Collected	2	750	-0.9...10	3...10	0.21	4
	V618413A-Ax***	G1/4	Internal	Not collected	1	1300	2...8	—	0.29	1
	V618423A-Ax***	G1/4	External	Not collected	1	1300	-0.9...8	3...8	0.29	1
	V618413D-Cx13A	G1/4	Internal	Collected	2	1300	2...10	—	0.27	4
	V618423D-Cx13A	G1/4	External	Collected	2	1300	-0.9...10	3...10	0.27	4
	V620413A-Ax***	G3/8	Internal	Not collected	1	2600	2...8	—	0.52	1
	V620423A-Ax***	G3/8	External	Not collected	1	2600	-0.9...8	3...8	0.52	1
NO	V620413D-Cx13A	G3/8	Internal	Collected	2	2600	2...10	—	0.50	4
	V620423D-Cx13A	G3/8	External	Collected	2	2600	-0.9...10	3...10	0.50	4
	V630413A-Ax***	G1/2	Internal	Not collected	1	4200	2...8	—	0.78	5
	V630423A-Ax***	G1/2	External	Not collected	1	4200	-0.9...8	3...8	0.78	5
	V604313A-Ax***	G1/8	Internal	Not collected	1	750	2...8	—	0.22	2
	V604323A-Ax***	G1/8	External	Not collected	1	750	-0.9...8	3...8	0.22	2
	V604313D-Cx13A	G1/8	Internal	Collected	2	750	2...10	—	0.21	4
	V604323D-Cx13A	G1/8	External	Collected	2	750	-0.9...10	3...10	0.21	4
	V618313A-Ax***	G3/8	Internal	Not collected	1	2600	2...8	—	0.52	2
	V620323A-Ax***	G3/8	External	Not collected	1	2600	-0.9...8	3...8	0.52	2
NO	V620313D-Cx13A	G3/8	Internal	Collected	2	2600	2...10	—	0.50	4
	V620323D-Cx13A	G3/8	External	Collected	2	2600	-0.9...10	3...10	0.50	4
	V630313A-Ax***	G1/2	Internal	Not collected	1	4200	2...8	—	0.78	5
	V630323A-Ax***	G1/2	External	Not collected	1	4200	-0.9...8	3...8	0.78	5
	V604411A-Ax***	G1/8	Internal	Not collected	1	750	1.5...8	—	0.30	3
	V604422A-Ax***	G1/8	External	Not collected	1	750	-0.9...8	3...8	0.30	3
	V604411D-Cx13A	G1/8	Internal	Collected	2	750	1.5...10	—	0.20	4
	V604422D-Cx13A	G1/8	External	Collected	2	750	-0.9...10	3...10	0.20	4
	V618411A-Ax***	G1/4	Internal	Not collected	1	1300	1.5...8	—	0.38	3
	V618422A-Ax***	G1/4	External	Not collected	1	1300	-0.9...8	3...8	0.38	3
NO	V618411D-Cx13A	G1/4	Internal	Collected	2	1300	1.5...10	—	0.27	4
	V618422D-Cx13A	G1/4	External	Collected	2	1300	-0.9...10	3...10	0.27	4
	V620411A-Ax***	G3/8	Internal	Not collected	1	2600	1.5...8	—	0.61	3
	V620422A-Ax***	G3/8	External	Not collected	1	2600	-0.9...8	3...8	0.61	3
	V620411D-Cx13A	G3/8	Internal	Collected	2	2600	1.5...10	—	0.50	4
	V620422D-Cx13A	G3/8	External	Collected	2	2600	-0.9...10	3...10	0.50	4
	V630411A-Ax***	G1/2	Internal	Not collected	1	4200	1.5...8	—	0.87	6
	V630422A-Ax***	G1/2	External	Not collected	1	4200	-0.9...8	3...8	0.87	6

\*\*\* Insert coil code from table below or 000 for version without solenoid. For manual override options, substitute 'X' as follows: 1 = without manual override, 2 = push and lock, 3 = push only

NC = Normally closed, NO = Normally open

## Coil &amp; voltage codes

Solenoid variant 1 (solenoid rotates 4 x 90°)

22 mm coil DIN EN 175 301-803 (DIN 43650 B)

Voltage	Coil code	Power inrush/hold	Model
12 V d.c.	12L	2 W	V10626-A12L
24 V d.c.	13L	2 W	V10626-A13L
24 V 50/60 Hz	14L	4/2.5 VA	V10626-A14L
48 V 50/60 Hz	16L	4/2.5 VA	V10626-A16L
110/120 V 50/60 Hz	18L	4/2.5 VA	V10626-A18L
220/240 V 50/60 Hz	19L	6/5 VA	V10626-A19L

## 22 mm coil industrial standard

Voltage	Coil code	Power inrush/hold	Model
12 V d.c.	12J	2 W	QM48/12J/21
24 V d.c.	13J	2 W	QM48/13J/21
24 V 50/60 Hz	14J	4/2.5 VA	QM48/14J/21
48 V 50/60 Hz	16J	4/2.5 VA	QM48/16J/21
110/120 V 50/60 Hz	18J	4/2.5 VA	QM48/18J/21
220/240 V 50/60 Hz	19J	6/5 VA	QM48/19J/21

## Solenoid variant 2

Double solenoid DIN EN 175 301-803 (DIN 43650 type C) 4 pin

Voltage	Coil code	Power inrush/hold	Manual override	Model
24 V d.c.	13 A	2 W	Push only	9031703900002400
24 V d.c.	13 A	2 W	Turn & lock	9031704900002400
24 V d.c.	13 A	2 W	Without	9031705900002400

Connection plugs must be ordered separately – see page 16

## Electrical details

Voltage tolerance: ±10%
Rating: 100% E.D.
Protection class: IP 65 with sealed plugs (ISO 6952)

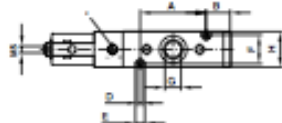
## Plug configuration, valve side/twin pilot

Symbol	Plug no.	Function	Actuation
	1	(+)	12 (Solenoid 2)
	2	(-)	12 + 14
	3	(+)	14 (Solenoid 1)

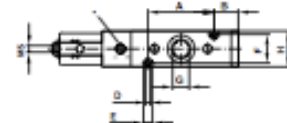


## Drawing dimensions

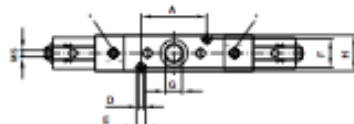
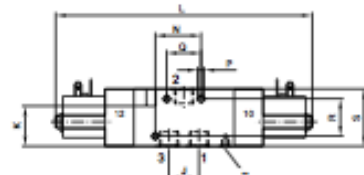
1



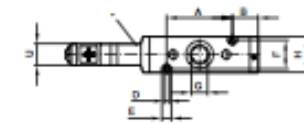
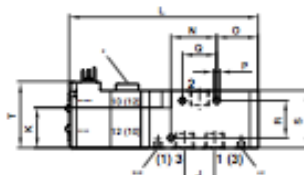
2



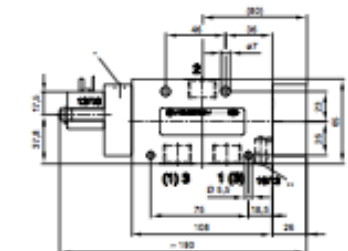
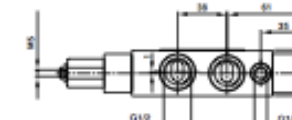
3



4

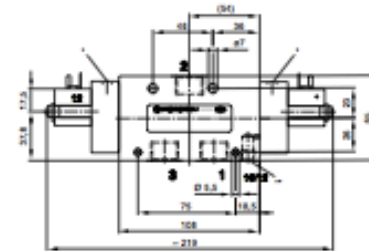
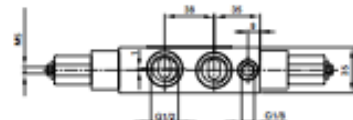


5



\* Manual override  
 \*\* External pilot supply (MS)  
 \*\*\* Collected pilot exhaust (ME)  
 \*\*\*\* Solenoid 1  
 \*\*\*\*\* Solenoid 2

6



Dimensional drawing no.	Type	A	B	C	D	E	F	G	H	J	K	L	M	N	O	P	Q	R	S	T	U
1	V60	35	17	—	3.2	6.5	17	G1/8; 6 deep	22	16.2	28	—	114	25	25	4.5	18	26	35	—	—
1	V61	46	18	—	3.2	6.5	20	G1/4; 10 deep	25	21	28	—	130	32	29	4.5	24	26	40	—	—
1	V62	54	21	—	4.5	8	28	G3/8; 11.5 deep	34	24.4	44	—	145	12	36	4.5	26	36	55	—	—
2	V60	35	17	—	3.2	6.5	17	G1/8; 6 deep	22	16.2	28	—	114	25	25	4.5	18	26	35	—	—
2	V61	46	18	—	3.2	6.5	20	G1/4; 10 deep	25	21	28	—	130	32	29	4.5	24	26	40	—	—
2	V62	54	21	—	4.5	8	28	G3/8; 11.5 deep	34	24.4	44	—	145	12	34	4.5	26	36	55	—	—
3	V60	35	—	—	3.2	6.5	17	G1/8; 6 deep	22	16.2	28	160	—	25	—	4.5	18	26	35	—	—
3	V61	46	—	—	3.2	6.5	20	G1/4; 10 deep	25	21	28	179	—	32	—	4.5	24	26	40	—	—
3	V62	54	—	—	4.5	8	28	G3/8; 11.5 deep	34	24.4	44	194	—	12	—	4.5	26	36	55	—	—
4	V60	35	17	—	3.2	6.5	17	G1/8; 6 deep	22	16.2	28	119	—	25	25	4.5	18	26	35	46	15
4	V61	46	18	—	3.2	6.5	20	G1/4; 10 deep	25	21	28	133	—	32	29	4.5	24	26	40	46	15
4	V62	54	21	—	4.5	8	28	G3/8; 11.5 deep	34	24.4	44	147	—	12	36	4.5	26	36	55	54	15

## **Appendix F: Solid State Relay**

The following pages were taken from data sheet provided by Allied Electronics®  
 (www.alliedelec.com)



## Series 1-DC

7-40Amp • 0-500 Vdc - DC OUTPUT

- MOSFET Output
- Low On-State Resistance
- Parallelizing Capability for Higher Currents
- Panel Mount

DC output relays feature MOSFET technology for low on-state resistance, assuring easy paralleling and switching capabilities to 40 amps at up to 200 Vdc. Lower current models are also available to 500 Vdc. All models come in Crydom's standard panel-mount package.

Manufactured in Crydom's ISO 9001 Certified facility for optimum product performance and reliability.

### OUTPUT SPECIFICATIONS ①

MODEL NUMBERS	D1D07	D1D12	D1D20	D1D40	D2D07	D2D12	D2D40	D4D07	D4D12	D5D07	D5D10
Operating Voltage Range [Vdc]	0-100	0-100	0-100	0-100	0-200	0-200	0-200	0-400	0-400	0-500	0-500
Load Current Range ② [Adc]	0-7	0-12	0-20	0-40	0-7	0-12	0-40	0-7	0-12	0-7	0-10
Max. Surge Current, [Adc] (10Msec)	15	28	42	106	22	27	106	17	36	19	29
Max. On-State Voltage Drop @ Rated Current [Vdc]	2.0	1.6	2.1	2.1	2.0	2.8	2.1	4.2	4.2	5.7	5.5
Thermal Resistance Junction to Case $R_{JJC}$ [°C/W]	2.2	1.34	1.06	0.83	1.5	1.06	0.83	1.06	0.8	1.0	0.8
Max On-state Resistance @ Rated Current ( $R_{DS(on)}$ ) [Ωrms]	.29	.13	.10	.05	.29	.23	.05	.6	.35	.8	.55
Max. Off-State Leakage Current @ Rated Voltage [mA]	0.1	0.2	0.3	0.3	0.1	0.3	0.3	0.3	0.3	0.2	0.3
Max. Turn-On Time [μsec]	100	100	100	100	100	100	100	100	100	100	100
Max. Turn-Off Time [msec]	1.0	1.0	1.0	1.0	1.0	1.0	1.0	1.0	1.0	1.0	1.0

### INPUT SPECIFICATIONS ①

### DC CONTROL

Control Voltage Range	3.5-32 Vdc
Maximum Turn-On Voltage	3.5 Vdc
Minimum Turn-Off Voltage	1.0 Vdc
Nominal Input Impedance	See Note 4
Maximum Input Current	1.6 mA (5 Vdc), 28 mA (32 Vdc) ③

### GENERAL NOTES

- ① All parameters at 25°C unless otherwise specified.
- ② Dielectric strength and insulation resistance are measured between input and output.
- ③ Heat sinking required, for derating curves see page 3.
- ④ Input circuitry incorporates active current limiter.

© 2008 CRYDOM Inc., Specifications subject to change without notice.

# crydom™

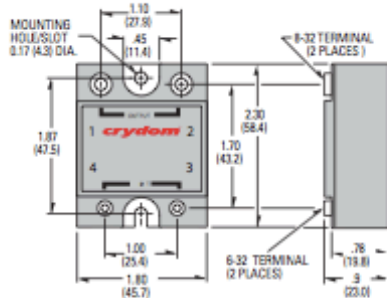
**Series 1-DC**  
7-40Amp • 0-500 Vdc - DC OUTPUT

#### GENERAL SPECIFICATIONS

Dielectric Strength 60Hz	2500 Vrms
Insulation Resistance (Min.) @ 500 Vdc	10 <sup>9</sup> Ohm
Max. Capacitance Input/Output	50 pF
Ambient Operating Temperature Range	-20 to 80°C
Ambient Storage Temperature Range	-20 to 125°C

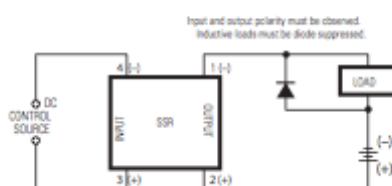
#### MECHANICAL SPECIFICATIONS

Weight: (typical)	3.0 oz. (86.5g)
Encapsulation:	Thermally Conductive Epoxy
Terminals:	Screws and Saddle Clamps Furnished, Unmounted



All dimensions are in inches (millimeters)

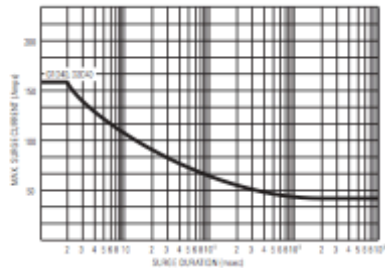
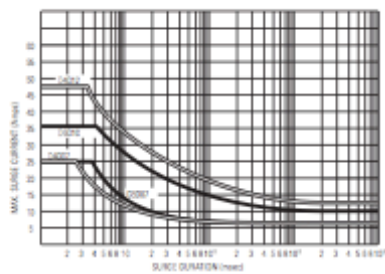
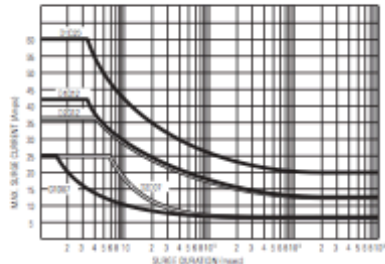
**Screw Torque Requirements:** 6-32 Screws - 10 in. lbs. (1.1Nm), 8-32 and 10-32 Screws - 20 in. lbs. (2.2Nm) (Screws dry without grease.)



#### Transient Protection

All loads are inductive, even ones that are not so labeled. An inductive load will produce harmful transient voltages when it is turned off. The more perfect the switch, the larger the transient voltage; the MOSFET output is so nearly an ideal switch that the transient voltages produced by seemingly "non-inductive" loads can cause damage if not suppressed. Diodes should be fast recovery type with PV rated greater than supply voltage.

#### MAXIMUM SURGE vs. DURATION



## Bibliography

- [1] Aaranson I., Tsimring L. (2006). *Patterns and Collective Behavior in Granular Media: Theoretical Concepts*, Reviews of Modern Physics, 78, pp.641-692.
- [2] Albert I., Tegzes P., Kahng B., Albert R., Sample J.G., Pfeifer M., Barbasi A.-L., Vicsek T., Schiffer P. (2000). *Jamming and Fluctuations in Granular Drag*, Physical Review Letters, 84(22), pp.5122-5125.
- [3] ASTM Standard D3080/D3080M – 11, *Standard Method for Direct Shear Test of Soils Under Consolidated Drained Conditions*.
- [4] Bocquet L., Losert W., Schalk D., Lubensky T.C., Gollub J.P. (2008) *Granular Shear Flow Dynamics and Forces: Experiment and Continuum Theory*, Physical Review E.
- [5] Cerato A.B., Letenegger A.J. (2006) *Specimen Size and Scale Effects of Direct Shear Box Tests of Sands*. Geotechnical Testing Journal, ASTM, 29(6), pp.1-10.
- [6] Chang J. -K., Takata K., Ichitani K., Taleff E. M. (2010). *Ductility of an aluminum-4.4 wt. pct. Magnesium Alloy at Warm- and Hot- Working Temperatures*. Materials Science and Engineering pp. 3822-3828.
- [5] Craig R.C. (2011) *Mechanics of Materials, 3<sup>rd</sup> Edition*, Wiley
- [6] Cundall P.A., Strack O.D.L. (1979). A discrete numerical model for granular assemblies. Geotechnique Volume 29, Issue I, pp. 47-65.
- [7] D'Anna G., Gremaud G. (2008). *Vibration Induced Jamming Transition in Granular Media*, Physical Review E, 64.
- [8] Das N., (2007) Modeling Three-Dimensional Shape of Sand Grains using Discrete Element Method. Graduate School Theses and Dissertations. Paper 689. Retrieved on May, 15 2012 from <http://scholarcommons.usf.edu/etd/689/>.
- [9] Dieter G. (1961) *Mechanical Metallurgy*, McGraw-Hill
- [10] Dijksman J. A., Wortel G. H., van Dauchot O., van Hecke M. (2011) *Jamming, Yielding, and Rheology of Weakly Vibrated Granular Media*, Physical Review Letters.
- [11] Dullien F.A.L. (1992), *Porous Media. Fluid Transport and Pore Structure*, Academic Press Inc.
- [12] Feda J. (1982) Mechanics of Particulate Materials, New York: Elsevier Science Ltd.

- [13] Ford K. J., Gilchrist J. F., Caram H. S. (2009). *Transitions to vibro-fluidization in a deep granular bed*, Powder Technology, 192, pp.33-39.
- [14] *Free-Cutting Brass (UNS C36000) for Automatic Screw Machine Products*, Copper Development Association Inc. Retrieved March 27, 2012 from [http://www.copper.org/applications/rodbar/alloy360/free\\_cutting.html](http://www.copper.org/applications/rodbar/alloy360/free_cutting.html).
- [15] Gere J.M. (2003), *Mechanics of Materials 6<sup>th</sup> Edition*, Belmont, CA: Thomson Learning Inc.
- [16] Graham L. (2006). Strain Gages and Force Measurement. Retrieved March 21, 2012 from Connexions <http://cnx.org/content/m13779/latest/>.
- [17] Hanes D. (1984). *Observation of rapidly flowing granular-fluid materials*, Journal of Fluid Mechanics, 150, pp. 357-380.
- [18] *Heat Treating of Specific Classes of Tool Steels*, ASM Handbooks Online, 4, ASM Handbook, ASM International, 1991.
- [19] Howell D., Behringer R.P. (1998). *Stress Fluctuations in 2D Granular Couette Experiment: A Continuous Transition*, Physical Review Letters, 82(26), pp.5241-5244.
- [20] Hsiau S., Sieh Y. (1999). *Effect of Solid Fraction on Fluctuations and Self-Diffusion of Sheared Granular Flows*, Chemical Engineering Science, 55 (11), pp.1969-1979.
- [21] Janda A. (2009). *Unjamming a Granular Hopper by Vibration*, A Letters Journal Exploring Frontiers of Physics, 87(2).
- [22] Ji S., Hanes D., Shen H. (2009). *Comparison of Physical Experiment and Discrete Element Simulations of Sheared Granular Materials in an Annular Shear Cell*, Mechanics of Materials 41, p. 764-776.
- [23] Klausner J. (2000). *Experimental Investigation of Cohesive Powder Rheology*, Powder Technology, 112, pp.94-101.
- [24] Lu K., Brodsky E.E. (2007), Kavehpour H.P., *Shear-weakening of the Transitional Regime for Granular Flow*, Journal of Fluid Mechanics, 587, pp.3477-372.
- [25] Metcalfe G., Tennakoon S. G. K., Kondic L., Schaeffer L., Behringer R. P. (2002). *Granular Friction, Coulomb Failure, and the Fluid-Solid Transition for Horizontally Shaken Granular Materials*, Physical Review E, 65.

- [26] Miller B., (1997) *Stress Fluctuations in Continuously Sheared Granular Media* (PhD Dissertation). Department of Physics Duke University.
- [27] Mueth D. M., Jaeger H. M., Nagel S. R. (1997). *Force Distribution in Granular Medium*, Physical Review E, 57(3), pp. 3164-3169.
- [28] Orlando A. D., Hanes D. M., Shen H., (2009) *Scaling Effects in Direct Shear Tests*. AIP Conf Proc. 1145, pp.413-416.
- [29] O'Sullivan C., Cui L., (2009) *Micromechanics of Granular Materials Response during Load Reversals: Combined DEM and Experimental Study*, Powder Technology, 193(3), pp.289-302
- [30] O'Sullivan C., Cui L., (2005). *Three-Dimensional Discrete Element Simulations of Direct Shear Tests*, Proc. 11<sup>th</sup> Int'l Conf. of IACMAG, Turin, Italy, Vol.1, pp. 119-126.
- [31] Puppala A. *Direct Shear Test*, UT Arlington Geotechnical Laboratory, Retrieved March 27, 2012 from  
<http://www.uta.edu/ce/geotech/lab/Main/Soil%20Lab/Direct%20Shear%20test/DS.pdf>.
- [32] Press W.H., Teukolsky S.A., Vetterling W.T., Flannery B.P. (2007), *Numerical Recipes*. 3<sup>rd</sup> Edition, New York: Cambridge University Press.
- [33] Rao K. K., Nott P. (2008). *An Introduction to Granular Flow*, New York: Cambridge University Press.
- [34] Roesler J., Harders H., Baeker M. (2007), *Mechanical Behavior of Materials*, Verlag Berlin Heidelberg: Springer
- [35] Smith J.O. III (2007), *Mathematics of the Discrete Fourier Transform (DFT) with Audio Applications*. 2<sup>nd</sup> Edition, W3K Publishing
- [36] Tardos G., McNamara S., Talu I. (2003). *Slow and Intermediate Flow of a frictional bulk powder in the Coutte geometry*, Powder Technology, 131, pp.23-39.
- [37] Taub A. I. (2006) *Automotive Materials: Technology Trends and Challenges in the 21<sup>st</sup> Century*. MRS Bulletin, vol. 31 pp. 336-343.
- [38] Wang D., Campbell C. (1992). *Reynolds Analogy for a Shearing Granular Material*, Journal of Fluids Mechanics, 244, pp.527-546.

## Vita

Jakub Jodlowski was born in Szczecinek, Poland where he grew up and attended the primary education institutions. In 2005, he graduated from III High School in Gdynia, where he was enrolled in an advanced math and computer science program.

In 2005 Jakub enrolled in Saint Louis University, campus in Madrid, Spain, where he began his academic engineering career, as well as developed knowledge of Spanish. In 2007 Jakub transferred to the University of Texas at Austin, where he continued working on the mechanical engineering degree. In 2008 he began the undergraduate research study on hot temperature deformation of aluminum alloys under a supervision of Prof. Eric Taleff. During the undergraduate career Jakub was involved in three projects studying static abnormal grain growth in aluminum alloys. As an undergraduate research assistant Jakub conducted and assisted experimental studies, and data analysis, as well as prepared reports and presentations on research development. From September 2009 to May 2010 Jakub was also a grader for Mechanical Behavior of Materials course taught at UT Austin. In 2010 Jakub provided solutions to the problems that were new or revised in the third edition of Mechanics of Materials by Prof. Roy Craig. He graduated with a Bachelor's degree in May 2010.

Prior to enrolling to graduate program in Mechanical Engineering at the University of Texas at Austin in August 2010, Jakub interned at Krafft Walzen© in Düren, Germany, a manufacturing company working with heavy turning components, where he further developed computer aided design skills. Jakub accepted a full time mechanical engineering position at Schlumberger©, starting June 2012.

Permanent email: jodlowski.jakub@utexas.edu

This thesis was typed by Jakub Jodlowski.